

LeMMINGs. II. The *e*-MERLIN legacy survey of nearby galaxies. The deepest radio view of the Palomar sample on parsec scale.

R. D. Baldi^{1,2,3,4*}, D. R. A. Williams^{5,6}, I. M. McHardy², R. J. Beswick⁵, E. Brinks⁷, B. T. Dullo⁸, J. H. Knapen^{9,10}, M. K. Argo^{5,11}, S. Aalto¹², A. Alberdi¹³, W. A. Baan¹⁴, G. J. Bendo^{5,15}, S. Corbel^{16,17}, D. M. Fenech¹⁸, J. S. Gallagher¹⁹, D. A. Green²⁰, R. C. Kennicutt^{21,22}, H.-R. Klöckner²³, E. Körding²⁴, T. J. Maccarone²⁵, T. W. B. Muxlow⁵, C. G. Mundell²⁶, F. Panessa⁴, A. B. Peck²⁷, M. A. Pérez-Torres¹³, C. Romero-Cañizales²⁸, P. Saikia²⁹, F. Shankar², R. E. Spencer⁵, I. R. Stevens³⁰, E. Varenus^{12,5}, M. J. Ward³¹, J. Yates¹⁸

27 October 2021

ABSTRACT

We present the second data release of high-resolution (≤ 0.2 arcsec) 1.5-GHz radio images of 177 nearby galaxies from the Palomar sample, observed with the *e*-MERLIN array, as part of the LeMMINGs (Legacy *e*-MERLIN Multi-band Imaging of Nearby Galaxy Sample) survey. Together with the 103 targets of the first LeMMINGs data release, this represents a complete sample of 280 local active (LINER and Seyfert) and inactive galaxies (HII galaxies and Absorption Line Galaxies, ALG). This large program is the deepest radio survey of the local Universe, $\gtrsim 10^{17.6}$ W Hz⁻¹, regardless of the host and nuclear type: we detect radio emission $\gtrsim 0.25$ mJy beam⁻¹ for 125/280 galaxies (44.6 per cent) with sizes of typically $\lesssim 100$ pc. Of those 125, 106 targets show a core which coincides within 1.2 arcsec with the optical nucleus. Although we observed mostly cores, around one third of the detected galaxies features jetted morphologies. The detected radio core luminosities of the sample range between $\sim 10^{34}$ and 10^{40} erg s⁻¹. LINERs and Seyferts are the most luminous sources, whereas HII galaxies are the least. LINERs show FR I-like core-brightened radio structures while Seyferts reveal the highest fraction of symmetric morphologies. The majority of HII galaxies have single radio core or complex extended structures, which probably conceal a nuclear starburst and/or a weak active nucleus (seven of them show clear jets). ALGs, which are typically found in evolved ellipticals, although the least numerous, exhibit on average the most luminous radio structures, similar to LINERs.

Key words: galaxies: active – galaxies: jet – galaxies: nuclei – galaxies: star formation – radio continuum: galaxies

1 INTRODUCTION

Observational studies support the idea of co-evolution of supermassive black holes (SMBHs) and their host galaxies (e.g. Heckman & Best 2014). For example, the empirical scaling relationships between black hole mass (M_{BH}) and both stellar velocity dispersion and host bulge luminosity (e.g. Ferrarese & Merritt 2000; Gebhardt et al. 2000; Tremaine et al. 2002) are indications of a coupled growth of the SMBH and its host galaxy. These relationships provide some of the most

basic constraints on models of SMBH and galaxy formation and evolution (e.g. Menci et al. 2004). However, these observational constraints are poorly known (e.g. Graham & Scott 2013; Shankar et al. 2013, 2016, 2019 and references therein), particularly at low M_{BH} , for which dynamical mass measurements become increasingly more challenging (Peterson 2014). This uncertainty at low masses prevents us from properly calibrating the scaling relations and the prescriptions for SMBH-galaxy growth used in semi-analytical and numerical models (Shankar et al. 2012; Barausse et al. 2017).

The agreement between the accreted mass function as extracted from continuity equation arguments for M_{BH} and

* E-mail: ranieri.baldi@inaf.it

nuclear luminosity distribution, and the local BH mass function derived from local scaling relations, strongly suggest that all local massive galaxies have undergone at least one major episode of Active Galactic Nuclei (AGN) in their past (e.g., Soltan 1982). It also supports the view that the vast majority of local galaxies host a central SMBH (e.g. Aller & Richstone 2002; Marconi et al. 2004; Shankar et al. 2004). The detection of AGN activity at the centre of galaxies is considered sufficient evidence to confirm the existence of a SMBH. The Eddington ratio¹ distribution of local galaxies has been measured to be extremely broad, mostly sub-Eddington, extending down to very low Eddington rates ($\sim 10^{-6}$, e.g., Kauffmann & Heckman 2009; Schulze & Wisotzki 2010). A large portion of low mass BHs hosted in low mass galaxies are thus expected, and indeed observed, to be among the faintest luminosity AGN, with the lowest accretion rates and Eddington ratios, and extremely weak nuclear outputs (e.g. Ho 1999, 2008; Panessa et al. 2007). These low-luminosity AGN (LLAGN) are traditionally defined as having $H\alpha$ luminosities $\leq 10^{40}$ erg s⁻¹ (Ho et al. 1997). They numerically dominate the local Universe (Nagar et al. 2002; Filho et al. 2006; Saikia et al. 2018) and include the two main classes of active galaxies, LINERs and Seyferts, distinguished by their optical emission lines (Heckman 1980). While Seyfert galaxies show clear multi-band signatures of BH activity (i.e. broad emission lines, hard X-ray spectra, Maoz 2007; Ho 2008), the physical origin of the central engine in LINERs has been debated: stellar or non-stellar nature (SMBH, shocks, or hot stars; see Ho et al. 1993 for a review)? The common interpretation is that a radiatively-efficient accretion disc appears to reconcile with the high-energy properties of Seyferts, while LINERs, which are typically fainter, are possibly powered by a radiatively-inefficient accretion disc (Kewley et al. 2006; Maoz 2007; Ho 2008; Heckman & Best 2014).

However, our view of the nuclear activity in the local Universe is partial and biased towards massive, bright and unobscured galaxies. In turn, detailed and complete studies of the low-brightness and low-mass active galaxy populations in the local Universe are still sparse. Optically weak or inactive galaxies can hide quiescent/low-accreting SMBHs, which are missed in the current local BH census. In fact, even star forming galaxies, although energetically dominated by dusty HII regions, and extremely enshrouded objects with high column densities can hide a compact object at their centers, which could reveal weak signatures of activity in optical, infrared and X-ray bands (e.g. Reines et al. 2013, 2016; Chen et al. 2017; Marleau et al. 2017; Girichidis et al. 2020). In addition, the BH activity is an episodic event: galaxies can go through periods of nuclear inactivity within their duty cycle, where their optical output is basically turned off and the SMBH becomes quiescent (e.g. Woltjer 1959; Marconi et al. 2004; Morganti 2017).

The best method to overcome this bias towards bright and massive galaxies is through radio observations which by virtue of not being obscured by intervening material allow the very centres of galaxies to be viewed in a less biased

way (despite opacity problems in the radio band, such as synchrotron self-absorption and free-free absorption). Radio observations consent to investigate a wide range of astrophysical phenomena, from those related to the formation, evolution, and death of stars (e.g. supernovae, SN), to accretion onto SMBHs. In case of stellar processes, thermal and non-thermal radiation is produced by stellar ejecta (e.g. SN remnants, SNR) and photoionisation; in active SMBHs a plethora of radio-emitting mechanisms can compete (see Panessa et al. 2019 for a review): jets (Padovani 2016; Blandford et al. 2019), disc winds (Zakamska & Greene 2014) or outflowing magnetically-active coronae (Laor & Behar 2008). Radio observations provide the best single diagnostic to separate star formation (SF) and AGN components (e.g. morphology, luminosity, brightness temperature).

Long-baseline radio arrays are suitable for detecting the low-level nuclear output of the LLAGN. These observatories, applied to nearby galaxies, provide the pc-scale resolution which is required to isolate the low-brightness nuclear emission, comparable to that of Sgr A*, from more diffuse emission of the host galaxy. Because of its long, UK-wide baselines, and large bandwidth *e*-MERLIN, is among the best radio arrays to detect compact structures, e.g., AGN cores, nuclear starburst and jets, in galaxies in the nearby Universe. A deep radio study of a complete sample of LLAGN at milli-arcsecond resolution and μ Jy sensitivity with *e*-MERLIN array has the potential to create a census of the constituent components of galaxies at unprecedented depth and at pc-scale linear resolution. This is the objective of the LeMMINGs (Legacy *e*-MERLIN Multi-band Imaging of Nearby Galaxy Sample²) survey (Beswick et al. 2014). To reduce bias against optically active AGN as present in previous studies, we chose as our target the magnitude-limited sample of nearby galaxy selected by Ho et al. (1997), which is commonly known as the 'Palomar sample'. This sample has a median distance of ~ 20 Mpc and is statistically complete with no radio imposed constraint or bias. This sample is by far the most widely observed, across a range of wavelength regimes (*Spitzer*, *Herschel*, *HST*, and with complete *Chandra* and VLA coverage). It includes all optical spectral classes (LINER, Seyfert, star forming and optically inactive galaxies) and morphological host types (early- and late-type galaxies), encompassing a wide range of BH masses (from intermediate BH up to the most massive BHs of the local Universe, 10^4 – 10^9 M_\odot) and accretion rates ($\sim 10^{-6}$ – 10^{-1} in Eddington units, Connolly et al. 2016).

Observations at L-band (1.5 GHz) of the first 103 galaxies of the LeMMINGs project were presented in the first data release by Baldi et al. (2018) (Paper I hereafter). One of the results reported there was the detection of pc-scale jetted structure in inactive galaxies down, to $M_{\text{BH}} \sim 10^6 M_\odot$, suggesting that a (weakly) active SMBH is present at the centre of local galaxies regardless of their optical class. Here we complete the full LeMMINGs sample presenting the images of the remaining 177 galaxies at 1.5 GHz and proceed to study the survey from both data releases combined. Basic results on the radio properties of this population of nearby galaxies are discussed in this work.

This paper is organized as follows. In Sect. 2 we present

¹ The Eddington ratio is defined as the ratio between the bolometric luminosity of the AGN (precisely, the disc luminosity, or a proxy) and the Eddington luminosity.

² <http://www.e-merlin.ac.uk/legacy/projects/lemmings.html>

the LeMMINGs project and sample, and the updated optical classification of the sub-sample of 177 galaxies. The observations and calibration of the radio data are explained in Sect. 3. The identification of the radio cores and the general radio properties of the sub-sample are presented in Sect. 4. We discuss the results and implications of the radio emission for the entire LeMMINGs survey (280 galaxies) in Sect. 5 and draw our conclusions in Sect. 6.

2 THE PALOMAR SAMPLE AND THE LEMMINGs SURVEY

2.1 Sample selection

The sample of this survey is a subset of the Revised Shapley-Ames Catalog of Bright Galaxies and the Second Reference Catalogue of Bright Galaxies ($\delta > 0^\circ$ and $B_T \leq 12.5$, Sandage & Tammann 1981; de Vaucouleurs et al. 1976), which was originally observed by Ho et al. (1995) with the Hale 5m telescope at the Palomar Observatory (Filippenko & Sargent 1985) to carry out a deep spectroscopic campaign. Ho et al. extracted the optical emission lines (H β , [O III], [O I], [N II], H α , [S II] doublet) from their spectra and used the emission line ratios to classify them as HII, Seyfert, LINER or Transition galaxy (see Sect. 2.2 for the updated classification).

The galaxies for which the active SMBH is the main photoionising source are Seyferts and LINERs, which represent the ~ 11 and ~ 19 per cent of the Palomar sample, respectively. The inactive galaxies are the HII galaxies (~ 42 per cent of the Palomar sample) where star forming regions populated by massive young stars mainly photoionise the surrounding gas, and the Absorption Line Galaxies (ALG, ~ 14 per cent) which are optically inactive galaxies. The latter shows no obvious emission lines and are typically in early-type galaxies. Ho et al. (1993) introduced a further class which they named Transition galaxies (~ 14 per cent). These are sources with composite characteristics of both LINER and HII galaxies and are based on a single diagnostic diagram (of [O III]/H β vs. [N II]/H α ; diagram 'a' in Figure 1).

The LeMMINGs survey focuses on a sub-sample of the original Palomar catalogue, namely on those galaxies with declination $> 20^\circ$ (280 targets), to ensure good visibility (or uv -plane) coverage, and accessibility to the e -MERLIN array over a wide hour-angle range. The survey was designed to carry out shallow observations at 1.5 and 5 GHz without the largest e -MERLIN antenna, the Lovell telescope. In addition, several galaxies were observed to greater depth as part of LeMMINGs (i.e., with the Lovell telescope included): M 82 (Muxlow et al. 2010), IC 10 (Westcott et al. 2017), NGC 4151 (Williams et al. 2017), NGC 5322 (Dullo et al. 2018), M 51b (NGC 5195, Rampadarath et al. 2018), and NGC 6217 (Williams et al. 2019).

In Paper I a resolution of 150 mas resulted in the detection of 1.5-GHz radio emission at pc scales, reaching a sensitivity of $\sim 75 \mu\text{Jy beam}^{-1}$. We detected 46 per cent (47/103) of the targets observed³, measuring radio dimensions typically $\lesssim 100$ pc and radio luminosities in the range

$\sim 10^{34}\text{--}10^{40} \text{ erg s}^{-1}$. Here, in analogy to Paper I, we report our observations of the remaining 177 Palomar galaxies at 1.5 GHz, listed in Table A1.

2.2 Revised optical classification

Whereas Seyferts display high ionisation lines which are indicative of photoionisation by an active nucleus, the typical emission line ratios of LINERs can be reproduced either by AGN photoionisation, collisional excitation by shocks, photoionisation by post-AGB stars, or by combined starburst and merger-driven shock (Allen et al. 2008; Sarzi et al. 2010; Capetti & Baldi 2011; Singh et al. 2013; Rich et al. 2014). In addition, the Transition Galaxies are not a well defined class, being a mixture of photo-ionisation by SF and a weak AGN. Therefore a secure and net separation between the different classes is necessary for a better and well-refined physical interpretation of each class. For this purpose, in analogy to what we performed in the first data release (Paper I), we revise the optical classifications carried out by Ho et al. (1997) by using the state-of-the-art spectroscopic diagnostic diagrams based on criteria introduced by Kewley et al. (2006) and Buttiglione et al. (2010). The former used SDSS emission-line galaxies and BPT diagrams (Baldwin et al. 1981) to classify mostly radio-quiet AGN galaxies, whereas the latter used optical spectra of radio galaxies from the Revised Third Cambridge Catalogue (3CR, Bennett 1962, i.e., only radio-loud AGN) obtained with the Telescopio Nazionale Galileo. Ho et al. scheme marginally differ in the separation of Seyferts and LINERs from those used by Kewley et al. (2006) and Buttiglione et al. (2010): Seyferts by Ho et al. (1997) with $\log([O III]/H\beta) > 0.5$ are now reclassified as LINERs. We also used the 'line ratios index' introduced by Buttiglione et al. (2010) as the average of three low ionisation line ratios for a more robust separation between LINERs and Seyferts. Furthermore, we opt for removing the Transition galaxy class, by classifying the given galaxy either as LINER or HII galaxy based on the other diagnostic diagrams ('b' and 'c' diagrams in Fig. 1). Finally, each target is classified as HII, LINER, or Seyfert based on at least two diagnostic diagrams in case the third criterion disagrees with the other two (see Paper I for more details).

Of the 177 galaxies, 122 exhibit at least four detected emission lines (i.e. having line uncertainties smaller than 50 per cent in Ho et al. 1997), which is enough to ensure a reliable classification in the BPT diagrams (Fig. 1). The remaining 55 sources are classified based on recent spectra taken from the literature (see notes in Table A1). The revision of their classification based on optical spectra resulted in a final sample of 89 HII galaxies, 60 LINERs, 14 Seyferts and 14 ALGs.

When considering galaxy morphological type, most of the sources are late-type galaxies (LTGs, spiral and irregular galaxies ~ 71 per cent), with a smaller fraction of early-type galaxies (ETGs, ellipticals and lenticulars). LINERs and ALGs are typically in ETGs, Seyferts have both early- and late-type morphologies and HII galaxies are mostly late-type systems (see Sect. 5 for more details).

have decided to remove this target from the group of detected galaxies (see Sect. 5 for details).

³ Based on a more detailed analysis of NGC 147, which was the least luminous detected radio source of the sample in Paper I, we

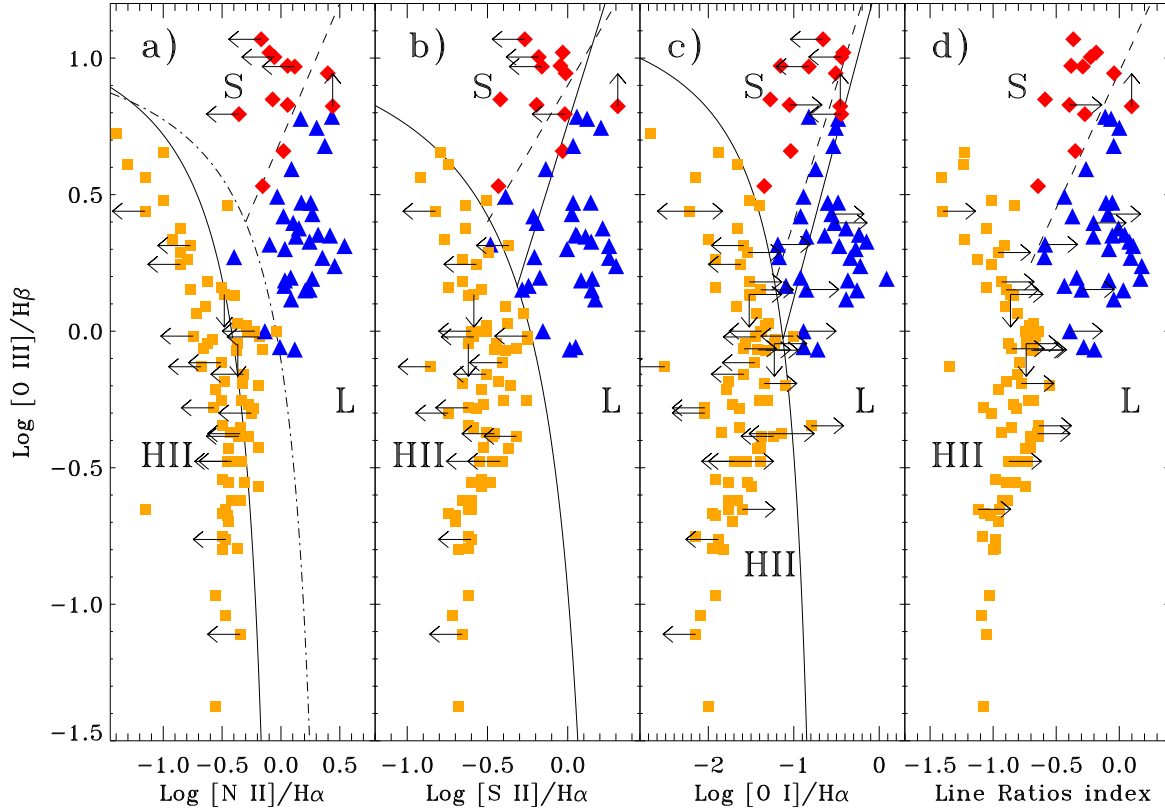


Figure 1. Diagnostic diagrams based on optical spectra (named BPT, Baldwin et al. 1981): $\log([O\ III]/H\beta)$ vs. a) $\log([N\ II]/H\alpha)$, b) $\log([S\ II]/H\alpha)$, c) vs. $\log([O\ I]/H\alpha)$, and d) line ratios index (the averaged line ratios, see the definition in Paper I). The data-points represent the 122 galaxies with emission line data taken from Ho et al. (1997) (the remaining 55 sources were classified based on data from the recent literature; see Table A1). In the first three panels, the solid lines separating HII galaxies, LINER, and Seyferts are taken from Kewley et al. (2006). The dashed lines between Seyferts and LINERs in the four panels separate the two classes according to the scheme introduced by Buttiglione et al. (2010). In panel a, the sources between the solid and the dot-dashed lines were classified as Transition galaxies by Ho et al. (1997), which we re-classify as LINER or HII galaxies based on the other diagrams ('b' and 'c'). We mark LINERs as blue triangles, Seyferts as red diamonds, and HII galaxies as orange squares. Several galaxies have different classifications with respect to those from Ho et al. (1997) because of the updated diagnostic diagrams (see Table A1).

3 OBSERVATIONS AND DATA REDUCTION

Detailed information on the *e*-MERLIN 1.5-GHz observations can be found in Paper I. The sub-sample presented in this work was observed from March 2017 to March 2019, divided into observing blocks of typically 10 targets, grouped based on their right ascensions to minimise the slewing of the 7 telescopes.

The observing strategy was identical to that used for the galaxies in Paper I: it consisted in following the target and the phase calibrator in at least six visits (cycles) to maximise *uv*-coverage given allocated time. A target-phase calibrator cycle usually lasted ~ 10 min, with ~ 3 min on the phase calibrator and ~ 7 min on the target. The phase calibrators were selected from the VLBA calibrator lists (Beasley et al. 2002) and/or from the latest RFC catalog⁴, chosen for being unresolved on *e*-MERLIN baseline scales. The bandpass calibrator (OQ 208) and the flux calibrator (3C 286) were typically observed for several minutes each. In this work, we present the data from seventeen scheduling blocks which include the 177 Palomar galaxies presented here (Table A1).

3.1 Data Calibration and Imaging with CASA

In a change from Paper I, where the data reduction was carried out using the AIPS⁵ software package, here the data has been calibrated with CASA (McMullin et al. 2007), the Common Astronomy Software Applications package. This change was prompted by the release of the *e*-MERLIN CASA pipeline⁶ at around the time the observations presented in this paper were conducted. In Section 3.2 we will present the differences between the two software packages.

The CASA pipeline converts 'fitsidi' format observation files into CASA measurement sets ('MS'); next it performs *a priori* flagging such as removing the first minutes of data when antennas are not yet all tracking a source, flagging the edges of the observing band and spectral windows, and applying any observatory flags.

The 512 MHz wide L-band suffers substantial radio frequency interference (RFI) due to a variety of sources, such as modems, satellites, mobile phones, and radars. Hence,

⁴ available from <http://astrogeo.org>

⁵ AIPS, the Astronomical Image Processing Software (Greisen 2003), is free software available from the NRAO.

⁶ https://github.com/e-merlin/eMERLIN_CASA_pipeline/

to achieve the highest sensitivity possible, RFI must be removed from the outset. The CASA pipeline uses the AOFLAGGER software (Offringa et al. 2012) which calculates a limiting threshold based on the raw data, above which any instances of RFI are automatically flagged and subsequently removed from the dataset. To remove any low-level RFI (the target observations are expected to be intrinsically faint) we further inspect the data with CASA task ‘plotms’, plotting the amplitude and phase of the visibilities as a function of time and channel/frequency to detect any amplitude spikes, dropouts, or intervals with null phase. We have estimated that the flagged data represents typically ~ 15 – 20 per cent of the raw data.

The data are subsequently averaged down in frequency by a factor of four to reduce the data volume and improve calibration speed without losing any significant information that might affect our scientific objectives. The pipeline then allows any additional manual flags to be added by the user, before proceeding with calibrating the data as follows. First, the flux for the primary calibrator 3C 286 is set using a model by ‘setjy’. This is followed by delay and phase-only calibration with the task ‘gaincal’ using a solution interval of ~ 10 s. Next is amplitude and phase calibration with a solution interval of 2–3 min in amplitude and phase. An initial bandpass response table was created to account for the changes of sensitivity across the band with the task ‘bandpass’. At this point further automatic identification and removal of data outliers in the time-frequency plane indicating RFIs is done with the task ‘flagdata’ (with ‘tfcrop’ mode). The flux density scale of 3C 286 is then bootstrapped to the secondary calibrator and target sources using ‘fluxscale’, taking into account that 3C 286 is slightly resolved by the longest *e*-MERLIN baselines. A final bandpass table is then recalculated using the spectral information obtained from the previous step. Final phase and amplitude solutions were recalculated after the bandpass correction. The phase solutions are usually delimited within $\pm 20^\circ$ independent of baseline, while the amplitude solutions show typical variations within a range of 10–20 per cent. The phase and amplitude solution tables are then applied to the data. A final step of flagging the data using ‘flagdata’ (‘tfcrop’ mode) is run as part of the pipeline to remove any RFI from the target fields. The solutions from the amplitude and phase calibration and the bandpass table were applied to the data to assess the data quality with ‘possm’. Diagnostic plots are produced and uploaded to a ‘weblog’ which allows for checking the quality of the calibration by showing such plots as the per-antenna flagging percentage at each step, calibration tables at each step and images of the calibrators and targets. These plots were inspected for any signs of remaining RFI or poor solutions in the calibration tables, with the option of running the pipeline again with manually input flags post averaging, with the aim of removing any subsections of the data that are of poor quality. After inspection of the diagnostic plots and manual excision of RFI in the target fields, the latter were ‘split’ from the now calibrated measurement set to create a single-source data file which is more manageable for the data imaging stage. In conclusion, the entire procedure achieved a maximum of 20 per cent calibration error in L-band.

Imaging of the *e*-MERLIN data (Stokes I) was also performed within the CASA environment, using the task

‘tclean’ on the ‘split’, calibrated datasets as described above. This task includes the possibility of using the ‘mtmfs’ deconvolver mode, which allows to reconstruct images from visibilities using a multi-term (multi-scale) multi-frequency approach (Rau & Cornwell 2011). After Fourier transforming the visibilities into an image, the latter is then ‘cleaned’, essentially deconvolved quasi simultaneously at a small number of characteristic scales, taking into account the no-null frequency dependence of the emission in the different sub-bands⁷. We used three different scales: the smallest scale size is recommended to be 0 (point source), the second the size of the synthesized beam and the third 3–5 times the synthesized beam. Since the nominal beam size of the *e*-MERLIN L-band observations is 150 mas, we used a cell size of 50 mas and we set the corresponding scales array to [0, 3, 10] pixels. The images were produced with natural baseline weighting, mapping a field of 1024×1024 pixels (~ 0.85 arcmin \times ~ 0.85 arcmin, i.e. 0.73 arcmin² which corresponds to an area of ~ 11.6 kpc² at the median distance of the sample).

For the targets with flux densities higher than 5 mJy, we carried out a few rounds of self-calibration in phase and a final one in phase and amplitude, using 1–2 min integration times and using a $3\text{-}\sigma$ minimum threshold for valid solutions. This procedure had the effect of increasing the signal-to-noise of the final maps and reducing the scatter in phase and gain solutions. Bright sources in the fields were mapped in parallel with the targets by using separate, small fields centred on their location, thus reducing the level of their side-lobes and their contribution to the effective noise floor for the fields on the targets.

Several images were created with different resolutions to explore the presence of diffuse low-brightness radio emission and to possibly detect a target in case of no detection in full resolution. Lower-resolution maps were obtained using different values of the ‘uvtaper’ parameter in ‘tclean’. This parameter specifies the width of the Gaussian function in the *uv*-plane to down-weight the contribution by the longer baselines. We chose values ranging between 300 and 750 k λ . The narrower the Gaussian, the less weight is given to the longer baselines and hence the lower the resolution of the resulting maps. A value of 300 k λ corresponds to a beam size typically 3 – 4 times larger (i.e. 0.45 – 0.6 arcsec) than that reached at full resolution. Furthermore, the angular resolution of the images strongly depends on the *uv*-plane coverage, hence the inclusion of the data from all seven antennas. Extreme data flagging can consequently result in degradation of the resolution. The range of restoring beam sizes is between 0.12 and 0.50 arcsec at full resolution.

Figures A1 and A2 (the full sets of figures for identified and unidentified sources will be as online supplementary data) present the full and low-resolution (*uv*-tapered) maps of the detected sources. For each detected galaxy we present one or two *uv*-tapered images chosen among those obtained with the highest ‘uvtaper’ parameters (typically 750–500 k λ) judged to be the best for illustrating the radio structure. The radio images have a large dynamic range which

⁷ We used 2 Taylor coefficients in the spectral model, which then corresponds to a spectrum defined by a straight line with a slope at the reference frequency of 1.5 GHz. The spectral image has not been considered in this work.

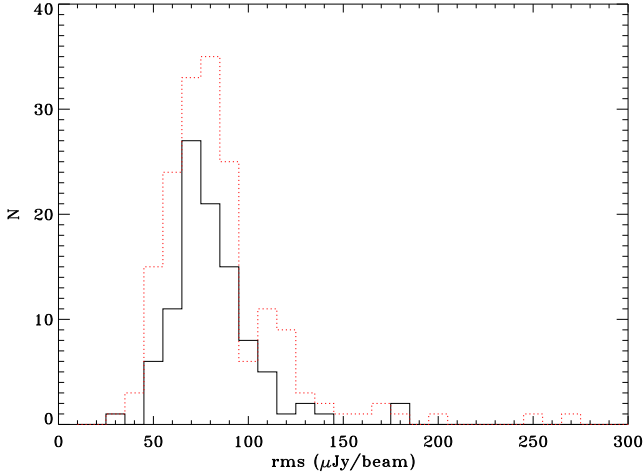


Figure 2. The effective rms noise distribution of the data (103 targets) presented in Paper I calibrated and imaged with AIPS (solid black line) and the data presented here (177 targets) calibrated and imaged with CASA (dashed red line). The result of a KS test is that the two distributions are not drawn from different parent populations at a confidence level greater than 95. Four targets with effective rms higher than $300 \mu\text{Jy beam}^{-1}$ are from images that are dynamic range limited and not plotted.

highlights their quality. For a small fraction of sources (in blocks 08 and 12), the image quality is modest, usually due to an antenna ‘drop-out’, but still adequate for the purposes of our survey (see Table A1).

To analyse the source parameters in the radio maps, we used ‘imfit’, part of the CASA ‘viewer’, which fits two-dimensional Gaussians to an intensity distribution on a region selected interactively on the map, providing the position, the deconvolved size, peak flux density, integrated flux density, and position angle (PA) of the source (all listed in Table A2 and Table A3). Whilst this procedure is valid for compact or slightly-resolved components, a simple technique to estimate the total brightness of an extended component is by interactively marking the region around the irregular shape of the source. Similarly, we estimate the rms noise of the maps by selecting a region around the target free from any significant emitting source. The maps show a range in effective rms noise of between ~ 30 and $250 \mu\text{Jy beam}^{-1}$. The higher values indicate we are for the brighter sources limited by the dynamic range of the data. An extreme example is the brightest source NGC 1275 in our sample with an integrated flux density of 47.1 Jy and an effective rms noise of $156 \text{ mJy beam}^{-1}$, or a dynamic range of about 300:1 (Tab. A4).

3.2 AIPS vs CASA

Since this Legacy Survey has been processed with two techniques based on AIPS and CASA softwares, a comparison of the data calibration and results between the two procedures is needed. Here we report the main differences and crucial similarities between Paper I and this work:

- Data calibrated and imaged via both CASA and AIPS (Paper I) were averaged in frequency and/or time by the same amount (averaged to 0.5 MHz channels and 2-seconds integrations) prior calibration procedures.

- Both ‘SERPENT’, the auto-flagging code (Peck & Fenech 2013) written in ParselTongue (Kettenis et al. 2006) used in Paper I, and AOFLAGGER are based on similar algorithms to assess the data quality and flag any instances of RFI. However, the updated version AOFLAGGER is more efficient than the SERPENT routine, because scripts searching for low-level RFIs have been optimised.

- In Paper I the calibration procedures began with a fit to the delay offsets among the distant antennas using the AIPS task ‘FRING’. Only recently a fringe fitting procedure became available in CASA, a Python-based global fringe fitter (task ‘fringefit’, van Bemmelen et al. 2019) developed specifically for long-baseline interferometers. The *e*-MERLIN CASA pipeline implements a simplified antenna-based delay correction. Moreover, since *e*-MERLIN utilises a single central clock, unlike VLBI arrays, no additional rate correction is essentially required.

- Each spectral window was used for amplitude and phase calibration, apart from their edge channels which are noisier. In Paper I we used the central 80 per cent of channels as recommended by the *e*-MERLIN cookbook, but the CASA pipeline uses the inner 90 per cent.

- The data published in Paper I underwent several rounds of phase-only self-calibration on the phase calibrators plus a final round of self-calibration in phase and amplitude. The *e*-MERLIN CASA pipeline performs a self-calibration on the calibrators, but it defaults to a point source model assumption rather than iteratively creating maps as in AIPS. In the classical assumption of a phase calibrator structure being dominated by a compact point source, the two routines are essentially the same.

- In the imaging technique, the AIPS task ‘imagr’ uses the Högbom clean method (Högbom 1974), which amounts to a brute force deconvolution by subtracting the brightest points in the map until it reaches a simply noisy map. Instead the deconvolution used by ‘tclean’ with ‘mtmfs’ mode offers multi-frequency synthesis of the wide-band data. AIPS task ‘imagr’ also offers a simplified multi-scale option in the cleaning phase, but CASA ‘tclean’ permits a better control of the parameters of the image deconvolution.

- In order to extract the source parameters from the detected components, AIPS task ‘jmfitt’ and CASA task ‘imfit’ work in a similar way by fitting a 2-D Gaussian across the source.

In the following we carry out a comparison between the two methods. First, we compare the rms noise obtained for the radio images of the 103 sources from Paper I and those calibrated in this work. Figure 2 shows the two rms noise distributions. The median values of two distributions are similar, 81 and $84 \mu\text{Jy beam}^{-1}$, for Paper I and this work, respectively. We also evaluate a two-sample Kolmogorov-Smirnov (KS) test, to compare the cumulative distributions of the two datasets. This test confirms there is no significant difference between the rms noise distribution of the two samples.

In addition, as a further test, we calibrated with CASA a randomly selected observing block of good quality, LEM 10, already published in Paper I. We run the CASA pipeline on the dataset by tuning the calibration steps and further flagging the RFIs and noisy visibilities. The calibrated dataset returns a lower rms noise level of $\sim 68 \mu\text{Jy beam}^{-1}$ than the $\sim 78 \mu\text{Jy beam}^{-1}$ achieved with

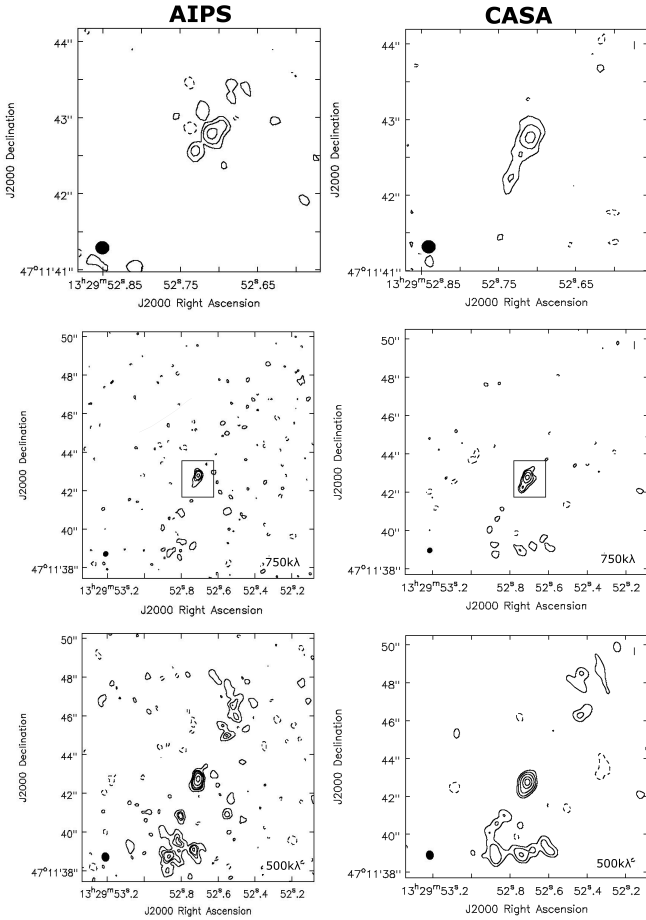


Figure 3. Radio maps (with natural weighting) of NGC 5194 for a comparison between the calibration and imaging performed with AIPS (left panels, taken from Paper I) and with CASA (right panels). The upper panels are at full resolution, the medium panels at 750k λ (the boxes represent the regions depicted in the upper panels at full resolution) and the lower ones at 500k λ with matched restoring beams. The rms noise of the CASA maps are 68 μ Jy beam $^{-1}$, while those of the AIPS maps are 78 μ Jy beam $^{-1}$. The contour levels are $3 \times \text{rms} \times N$, where $N = [-1, 1, 2, 4]$, $[-1, 1, 2, 3, 6]$, and $[-1, 1, 2, 2.5, 3.3, 5, 8]$ respectively for the three sets of panels from the top to the bottom.

the AIPS routine. The targets which were not detected with AIPS remain as such with CASA (NGC 4914, NGC 5055, NGC 5112, and NGC 5297). The restoring beams obtained with the two procedures are consistent with each other. The detected targets (NGC 5005, NGC 5194, NGC 5195, NGC 5377, and NGC 5448) display similar but not identical radio structures identified in the AIPS maps (see next paragraph and Figure 3 for a detailed comparison). At full resolution the peak flux densities of the unresolved components (with matched synthesised beams) are typically ~ 87 per cent of the estimates obtained with AIPS task ‘*imagr*’. The difference is insignificant in the lower resolution maps. The integrated fluxes of the extended structures are consistent with the measurements obtained with AIPS. In terms of resolved structures, the wide-band imaging with CASA resulted in emission features that were better defined, reducing the confusion between noisy artifacts and genuine

regions of emission. The differences revealed between the two procedures are probably the result of two aspects: i) the AOFLAGGER software provides a better flagging of data affected by RFI, returning a lower rms noise level; ii) the multi-scale multi-Frequency synthesis of the CASA task ‘*tclean*’ probes the spatial and spectral characteristics present in the data in a more accurate mode than the CASA task ‘*imagr*’. Furthermore, the different self-calibration routes of the two procedures could also lead to a little influence on the dynamic range of the target itself, if the object is highly detected (high signal-to-noise ratio) and can be self-calibrated. Conversely, the inability of self-calibrating because of a weak or non-detected target could largely affect the noise levels of the map and probably contribute to the different noise levels observed between the maps produced with CASA and AIPS.

Figure 3 shows an example of two sets of radio images for the galaxy NGC 5194 obtained from the same raw data calibrated and imaged with the two software packages. As discussed before, the neater structures (i.e. see the edge of the southern radio lobe) and the lower rms noise observed in the CASA images of this target probably result from the combination of different steps of the two procedures. This example provides the level of reliability of the low-brightness structures observed in the maps of our sample and suggests caution in interpreting weak source structures, obtained either with or without self-calibration.

We can conclude that the two data calibration and imaging techniques based on AIPS and CASA produce consistent results in terms of flux densities and detected emission regions, with minor differences which are still within the absolute flux calibration error of < 20 per cent.

4 RESULTS

4.1 Radio maps and source parameters

As one of the key goals of the LeMMINGs Survey is to study of the 1.5-GHz emission ascribed to the central SMBH, we examine the innermost region of the galaxy in the full-resolution and *uv*-tapered images near the optical/infrared identification of the supposed nucleus. Practically, we search for significant radio emission, i.e. we detect a source component if its flux density is above 3σ of the local noise in analogy to Paper I⁸. In the cases of diffuse low-level emission and no detection, we extract a 3σ upper-limit to the core flux density at full resolution. Moreover note that the larger beams of the *uv*-tapered maps could cause the appearance of additional components not present at full resolution due to increased signal-to-noise ratio.

The median rms noise of the final naturally-weighted full-resolution images is 84 μ Jy beam $^{-1}$, with a median ratio between the peak flux density and the rms noise of five. We detected radio emission for 78 out of the 177 targets with flux densities ≥ 0.25 mJy. For such sources, we also derive the flux densities of their counterparts in the *uv*-tapered maps. The source parameters (e.g. peak/integrated flux, deconvolved major/minor axes, position) for the detected sources

⁸ We are aware that 3σ limit might include spurious detections for particularly weak sources.

are listed in Table A2 and A3. The contour levels and the restoring beam parameters are listed in Table A4. For the remaining 99 objects, no significant radio emission ($> 3 \times \text{rms}$ level) was detected in the imaged fields, neither at full- nor at low-resolution.

The morphology of the detected radio structures is varied, ranging from pc-scale unresolved cores to jetted to extended and complex shapes. The lower resolution images generally reveal a more extended morphology than the full-resolution images. The radio structures vary in size from 150 mas at the smallest scale for unresolved sources to up to 17 arcsec for sources like NGC 5548 (~ 6 kpc). With a mean size for the radio structures in the survey being 0.5 arcsec, i.e., a physical size $\sim 3 - 550$ pc (median ~ 100 pc), most of the sources are slightly resolved or unresolved. All of the radio sizes for the resolved sources are listed in Table A2 and A3.

In agreement with Paper I, we identify the radio core in each source as the unresolved central component, which might be associated with the active SMBH or nuclear star-forming region. We used the specific radio morphologies of each source combined with the optical centre of the galaxy obtained from the NASA Extragalactic Database (NED⁹) to gauge the distance of the radio core from the optical centre. For sources with a symmetric structure, the central unresolved component is assigned to be the radio core, but for asymmetric sources the brightest component is used. The distance between the optical galaxy centre and the closest possible radio component is the main criterion for a core identification (see more details in Paper I).

There have been several previous VLA observations of subsets of the Palomar sample which, with the final goal of studying the nuclear activity, were successful in detecting radio cores at the centre of the galaxies, at resolution of $\sim 1-2$ arcsec (e.g. Nagar et al. 2002; Filho et al. 2000; Nagar et al. 2005). The VLA core position generally matches with the optical centre of the galaxy within the VLA beam width. This spatial coincidence sets the upper limits of the radius from the optical centre where an active SMBH could be located.

The previous VLA observations did not resolve the *e*-MERLIN cores, but on the contrary *e*-MERLIN resolves out part of the extended radio emission visible in VLA maps. This is also because of the longer baselines of the *e*-MERLIN array which results in the *e*-MERLIN angular resolution being five times better than that of most previous VLA surveys. This higher resolution in turn complicates for identifying the correct position of the radio-emitting SMBH within the VLA beam width around the optical galaxy centre without a more precise localisation, like from VLBI. Therefore, optical and *e*-MERLIN astrometries play a crucial role in pinpointing the active SMBH. The *e*-MERLIN astrometry is set by the International Celestial Reference Frame to an accuracy a few 10 mas. We note that the positional uncertainties are therefore now dominated by the positional uncertainty in the optical observations. In fact, absolute optical positions provided by NED are limited by seeing and the light profile across the nuclear region observed by the optical telescopes catalogued in NED. The NED target positions

typically refer to the position accuracy of the Two Micron All Sky Survey, i.e. $\sim 0.3 - 0.5$ arcsec¹⁰. Considering the relative optical-radio astrometry, systematic errors and plausible degradation of the *e*-MERLIN resolution/astrometry due to low phase reference quality and/or a low signal-to-noise ratio of some sources, we set 1.5 arcsec as a conservative, maximum offset from the optical nucleus to search for a radio core in the *e*-MERLIN maps in analogy to Paper I.

For 66 out of the 78 detected sources in the sample presented in this work, evident radio cores are identified within 1.2 arcsec from the optical centre of the galaxy: we refer to them as ‘identified’ sources (see Sect. 4.2). For 12 of the 78 detected sources we cannot clearly identify the radio source with the nucleus of the galaxy either because the optical-radio separation is > 2 arcsec or because there are multiple radio components within 1 arcsec of the optical centre. In addition to those, three galaxies which have a detected identified core (NGC 2832, NGC 3077, NGC 4111) reveal additional significantly bright structures in the field, associated with galaxy companions or other sources of ambiguous nature (named ‘identified+unidentified’). These 15 (12 galaxies + 3 sources in the field of three identified galaxies) sources have been called ‘unidentified’ hereafter (see Sect. 4.3). The core-identification tags for the sample are listed in Table A1 and are described in details in the next sub-sections.

4.2 Identified sources

The full and low-resolution maps of the 66 detected and identified galaxies are presented in Figure A1, along with the tables including source characteristics (Table A2), radio contours and restoring beams (Table A4).

To ensure that the ‘identified’ sources are genuine, we calculated the probability of detecting a radio source above the 0.25-mJy detection limit of the LeMMINGs survey within a given area of sky. We use the source count distribution obtained from the 1.4 GHz *e*-MERLIN legacy programme SuperCLASS (Battye et al. 2020) over an area of ~ 1 square degree centred on the Abell 981 super-cluster to provide an upper limit on the number of background confusing sources. We find that when observing 177 galaxies, statistically at most one unrelated radio source falls within a circular radius of ~ 2.6 arcsec of the optical centre. Hence, given this result, a radio sources detected within a 1.2 arcsec circular aperture can with a high degree of confidence likely be identified with the central optical nucleus, e.g., with an SMBH.

Radio cores were detected at full resolution for all 66 identified sources with the exception of one, NGC 4369, which is undetected at full resolution but reveals a radio core coincident with the optical galaxy centre in the lower resolution radio images. Most of the sample have peak core flux densities ~ 1 mJy beam⁻¹. The brightest source is NGC 1275 which reaches a 10.5 Jy beam⁻¹ peak flux density. Most of the central components can be considered unresolved or compact as the deconvolved source sizes are much smaller than the beam size. For those sources the peak flux densities of the radio core components are usually consistent with the integrated flux densities to within a factor of ~ 2 .

⁹ <https://ned.ipac.caltech.edu/>

¹⁰ https://old.ipac.caltech.edu/2mass/releases/second/doc/sec6_7f.html

Those which have significantly larger integrated flux densities than their peak flux densities include sources that are extended or contain multiple components.

For 17 identified sources, clear extended radio structures are observed, which have been preferentially interpreted as originated from a compact jet. There are several reasons why compact jets might be preferentially detected: the high spatial resolution (150 mas) and the lack of short-spacings of the *e*-MERLIN array, and the use of snapshot imaging of the LeMMINGs program which produces sparse *uv*-coverage, cause loss of sensitivity to diffuse low-brightness emission, such as expected by a galaxy disc (Brown & Hazard 1961; Kennicutt 1983) (see Section 6.3 for discussion). We estimate that, based on the properties of our observations (array configuration and snapshot imaging), *e*-MERLIN appears to resolve out up to 75 per cent of the radio structure detected with VLA with 1-arcsec resolution: based on previous VLBI and VLA studies (e.g. Hummel et al. 1982; Falcke et al. 2000; Nagar et al. 2005; Panessa & Giroletti 2013), LINERs are less affected by this issue than Seyferts and HII galaxies, which are generally associated with more extended low-brightness radio emission than LINERs. However, this interpretation does not preclude the possibility that the radio emission arises from compact radio emission from circumnuclear SF (e.g. Linden et al. 2020) or circumnuclear disc (e.g. Carilli et al. 1998).

The 66 identified sources were divided into five distinct classes, based on their radio morphology in both the full- and low-resolution maps (Table A1), in analogy to Paper I. The five morphologies are discussed below:

- *core/core-jet*, marked as A (49 galaxies): these sources show bright unresolved or slightly resolved cores and often show a protrusion (Conway et al. 1994). A few radio components could be aligned in the same direction of the possible jet. Some examples include NGC 1161 and NGC 1275.
- *one-sided jet*, marked as B (3 galaxies): the one-sided jets show a clear asymmetric extended jet structure with multiple one-directional components emerging at different resolutions, possibly due to relativistic beaming of the jet. Some examples include NGC 5322.
- *triple-source*, marked as C (8 galaxies): Triple-sources have three aligned components. These components are interpreted as the radio core and adjacent jets/lobes. These sources may appear as twin-symmetric jets in the lower resolution images. Some examples include NGC 4036 and NGC 4589.
- *double-lobed*, marked as D (0 galaxies): these sources have two large radio lobes over extended scales in either the full or low resolution images (see NGC 5005 from Paper I). A possible overlap with C-type morphologies in case of triple source with two weak unresolved radio lobes (see NGC 3348).
- *jet+complex*, marked as E (6 galaxies): these sources show a complicated radio morphology with several components dispersed around a core. They could hide a possible jet interacting with the interstellar medium (ISM) or be an extended star-forming region. Some examples include NGC 1186 and NGC 2964.

To further discriminate the radio sample, the radio sources which show ‘jet-like’ morphologies (e.g. one-sided, two-sided, triple, double-lobed sources) are hereafter named

‘jetted’ and those without a clear jet, ‘non-jetted’. Note that the radio classification can be equivocal because of the low-brightness of the radio structures.

4.3 Unidentified sources: background sources, M 82 and Arp 299

Fifteen sources (12 galaxies and 3 radio sources appeared in three core-identified galaxies) are considered as ‘unidentified’. The online supplementary data include the full and low-resolution maps for these ‘unidentified’ sources (for radio contours and restoring beam see Table A4) and their radio source parameters are listed in Table A3.

Seven objects show off-nuclear radio sources further than 4 arcsec from the optical centre and as far away as ~ 38 arcsec, but still falling within the extent of the optical galaxy. The morphology varies from multiple compact components, double/triple sources, to a single unresolved component on a typical scale of a few arcseconds with low flux densities (< 1 mJy beam $^{-1}$). The nature of this off-nuclear emission is ambiguous, whether related to star-forming regions or background AGN. Using the same approach as in Section 4.2, it is possible to estimate the likelihood of radio sources falling within 4 arcsec and 38 arcsec radii (the offsets measured above) and hence consider whether they are likely related to the nuclear core. The expected number of unrelated sources detected within those radii are 3.8 and 65.2 respectively, suggesting that the off-nuclear sources are potentially background objects. However, we cannot rule out the possibility that those off-nuclear sources nonetheless belong to the galaxy concerned.

Five galaxies show several components in the nuclear region (< 4 arcsec) and it is therefore difficult to pinpoint unequivocally the core (NGC 2750, NGC 3034, NGC 3690, NGC 4631 and NGC 5012). The low resolution maps of NGC 2750, NGC 4631 and NGC 5012 reveal a few components near the optical centre. The cases of NGC 3034 and NGC 3690 deserve more attention and are presented below.

NGC 3034 (M 82) is a dusty star forming galaxy which lacks clear evidence of an active nucleus so far. We detect a mix of SNe, SNRs, and HII regions, which have been previously identified by (*e*-)MERLIN (e.g. Muxlow et al. 1994; Beswick et al. 2006; Fenech et al. 2008, 2010; Muxlow et al. 2010; Gendre et al. 2013; Varenus et al. 2015 and references therein). Amongst the stellar remnants we find SN 2008iz which is the brightest source in the LeMMINGs images of M 82 and has a peak luminosity of ~ 60 mJy at 1.5 GHz (epoch 19 April 2017). This bright radio source has been interpreted as synchrotron emission due to an expanding SN shock which encounters clumpy dense medium (Bruntz et al. 2010; Kimani et al. 2016). One of the interesting sources detected in the *e*-MERLIN map of M 82 is also 41.95+575, which has a double-lobed structure at VLBI resolution and has been decreasing by ~ 8 per cent per year for the last 5 decades. Hence, 41.95+575 may be a remnant of a Gamma Ray Burst instead of a conventional SNR (Muxlow et al. 2005). Several faint sources ($< a$ few sub-mJy) detected in previous radio observations are missing from our map due to low sensitivity and resolution, such as X-ray Binaries (XRB) and, in particular, a transient discovered by Muxlow et al. (2010) at RA 09h55m52.5083s, Dec. +69°40′45″.410 (J2000).

NGC 3690, an interacting system also known as Arp 299 (or Mrk 171), is an interesting case, composed of two galaxies: the eastern, brightest member NGC 3690A, and the western member NGC 3690B. We use the names Arp 299-A and Arp 299-B to refer to NGC 3690A and NGC 3690B, respectively, in agreement with the nomenclature used in Fig. 1 from [Romero-Cañizales et al. 2011](#). In our *e*-MERLIN maps we detected three sources, which correspond to i) Arp 299-A, ii) Arp 299-B, and iii) Arp 299-C which could be a satellite galaxy taking part in the merger event or a vigorous off-nuclear star-forming region related to the merging system ([Tarchi et al. 2011](#)). These sources have been confirmed and largely studied by previous continuum and spectroscopic radio, infrared and X-ray observations (see [Alonso-Herrero et al. 2000](#); [Pérez-Torres et al. 2009](#); [Tarchi et al. 2011](#); [Romero-Cañizales et al. 2011](#); [Bondi et al. 2012](#); [Romero-Cañizales et al. 2014](#); [Kankare et al. 2014](#); [Anastasopoulou et al. 2016](#) and references therein). Specifically, Arp299-A was resolved into several components with VLBI: an extremely prolific SN factory ([Neff et al. 2004](#); [Pérez-Torres et al. 2009](#); [Ulvestad 2009](#)), and a LLAGN ([Pérez-Torres et al. 2010](#)). In addition, Arp 299-B has been resolved into two main components: B1, which includes another SN factory, although less extreme than the one in Arp-299A ([Ulvestad 2009](#); [Romero-Cañizales et al. 2011](#); [Sliwa et al. 2012](#)), an AGN (detected in hard X-rays, [Ptak et al. 2015](#)) and a bright transient source (Arp299-B AT1; [Mattila et al. 2018](#)); and B2 ([Neff et al. 2004](#); [Alonso-Herrero et al. 2000](#)), a weaker component with no reported compact radio sources in it. Subsequent VLBI and infrared observations of the transient AT1 in the nucleus of Arp 299-B, showed an increase in luminosity over several years, which was later identified with a jetted tidal disruption event (TDE; [Mattila et al. 2018](#) and references therein). We have not resolved the nucleus of Arp 299-B into its compact components, but we clearly detect it with a flux density of 14.1 mJy (on 18 April 2017), so it is likely that we have detected the late time radio emission of AT1 at 1.5 GHz, together with the quiescent emission of its host Arp 299-B. Two of the several well-known SNe present in this system, SN 2010O and SN 2010P ([Romero-Cañizales et al. 2011, 2014](#); [Kankare et al. 2014](#)) are not detected in our map with a flux density upper limit of <0.6 mJy beam $^{-1}$. The current and past observations of NGC 3690 appear to confirm that both starburst and AGN can co-exist in this merging system, as pointed out by, e.g., [Pérez-Torres et al. \(2010\)](#) and [Romero-Cañizales et al. \(2011\)](#).

In conclusion, it is worth mentioning that the source confusion level is high in NGC 3690 as well as in M 82 (and probably in other sources of our sample) even at the *e*-MERLIN resolution, where both stellar and SMBH processes are probably embedded in dusty regions and difficult to disentangle within a few tens of parsec at the centre of a (obscured) galaxy.

Three galaxies (NGC 2832, NGC 3077 and NGC 4111) which have been core-identified, show additional radio sources in the field. For example the radio map of NGC 2832 reveals the radio core component of its companion NGC 2831. The off-nuclear radio source in NGC 3077 is a potential SNR ([Rosa-González 2005](#); [Leonidaki et al. 2010](#)).

4.4 Undetected galaxies

Most of the LeMMINGs sample (99/177) have not been detected. The vast majority of our undetected sources were also not detected by previous VLA campaigns ([Nagar et al. 2002, 2005](#)). However, there are some galaxies for which *e*-MERLIN have not detected any core, which instead was detected by the VLA (i.e. NGC 3780) and viceversa (i.e. NGC 6340) in different radio observation frequencies (1 – 15 GHz) and epochs.

It is important to note that undetected as well as ‘unidentified’ galaxies, may still conceal an AGN. Indeed, radio-emitting active SMBHs may be below the detection limit of the LeMMINGs survey or not identified in the more complex structures listed above (see for example the cases of M 82 and Arp 299). Radio core variability on a time scale of a few years, episodic accretion onto the BH and nuclear inactivity expected within a typical duty cycle of $\lesssim 10^8$ years could also account for their current none detection (e.g. [Mundell et al. 2009](#); [Morganti 2017](#); [Alexander et al. 2020](#)). Future *e*-MERLIN 5 GHz observations of the LeMMINGs targets with higher resolution and sensitivity will be able to possibly pinpoint the core with higher accuracy than L-band data.

5 THE COMPLETE LEMMINGS LEGACY SURVEY

In the following we present the radio flux and luminosity distributions, radio morphology and brightness temperatures for the full sample of LeMMINGs galaxies combining the first data release (Paper I) with the observations presented in this work. The detailed scientific results for the full LeMMINGs sample and for each optical class will be reported in forthcoming papers.

In the entire Legacy survey *e*-MERLIN detected radio emission in 125 targets (typically $< a$ few mJy) at scales of a few tens of parsecs in a statistically-complete sample of 280 nearby galaxies (~ 44.6 per cent)¹¹. The 3σ flux density limit of this survey is ~ 0.25 mJy beam $^{-1}$ and the range of detected peak flux densities F_{core} covers three order of magnitudes from a fraction of a mJy to a few Jy beam $^{-1}$. The galaxies are detected out to ~ 100 Mpc (Fig. 4, upper panel), but the fraction of radio detections increases with the distance to the targets, with only ~ 20 per cent of galaxies nearer than ~ 20 Mpc (the median distance of the sample) being detected but ~ 40 per cent within 50 Mpc. The core luminosity (F_{core} integrated over the *e*-MERLIN L-band, 1.244 – 1.756 GHz) L_{core} vs. distance plot of the LeMMINGs program is presented in Fig. 4 (lower panel). The identified sources lie above the black dotted curve which corresponds to the detection threshold as shown in the top panel of Fig. 4, while the undetected and unidentified sources straddle the curve.

The core luminosities¹² range between $\sim 10^{33.8}$ to 10^{40}

¹¹ NGC 147 was classified as ‘identified’ in Paper I, but a more careful analysis of its HST position indicates that the radio detection lies at (> 2 arcsec) from the optical nucleus. Therefore its updated classification is ‘unidentified’.

¹² The radio luminosities have been presented in units of erg s $^{-1}$. To convert the radio luminosities from erg s $^{-1}$ to monochromatic

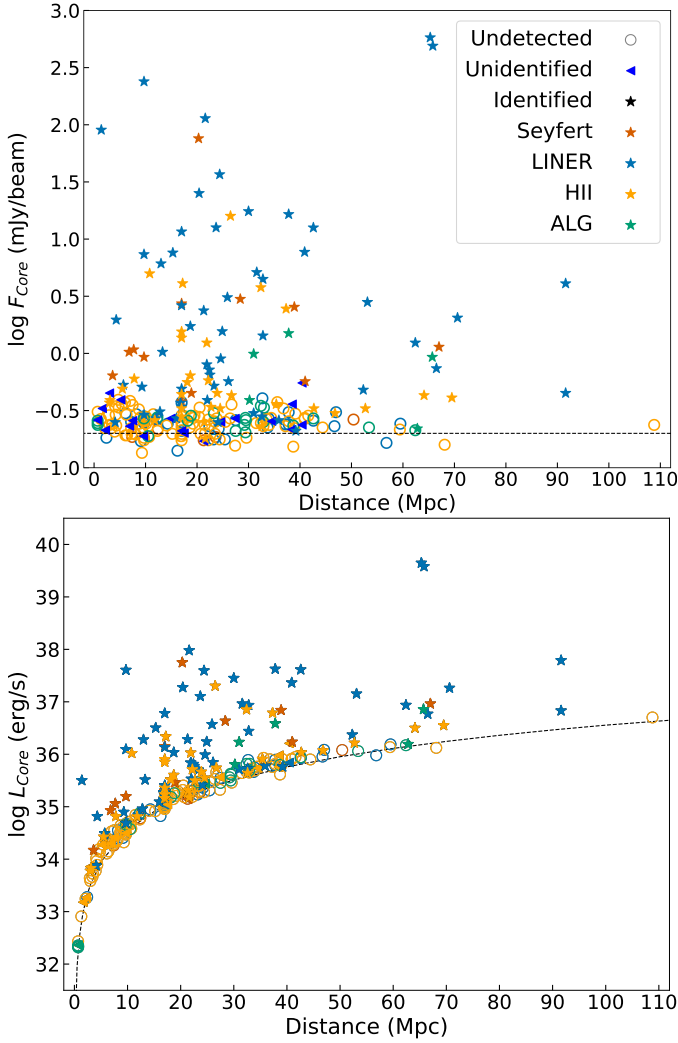


Figure 4. Radio core flux density (F_{core} in mJy beam^{-1} , upper panel) and its luminosity (L_{core} , integrated over the *e*-MERLIN L-band, 1.244 – 1.756 GHz, in erg s^{-1} , lower panel) as a function of distance (Mpc) for the full sample. The dashed lines represent the 3σ flux density limit of this survey ($0.25 \text{ mJy beam}^{-1}$) and the corresponding luminosity, respectively in the upper and lower panels. The symbols in the legend indicate the status of their detection (open circles for undetected and filled stars for detected) and their optical class (red Seyferts, light blue LINERs, yellow HII galaxies and green ALGs). For the unidentified (blue left-pointing triangles) and undetected radio sources, the values on the y-axis should be understood as upper limits. The typical error bar on flux densities and luminosities is 20 per cent of the values. To convert the radio luminosities from erg s^{-1} to W Hz^{-1} at 1.5 GHz, an amount +16.18 should be subtracted from the logarithm of the luminosities presented in the graph.

erg s^{-1} ($\sim 10^{17.6} - 10^{23.8} \text{ W Hz}^{-1}$), or down to $10^{32} \text{ erg s}^{-1}$ when including our upper limits for the non-detected cores. A Kaplan-Meier (censored) mean value (Kaplan & Meier 1958) of $1.5 \times 10^{34} \text{ erg s}^{-1}$ is found. The radio luminosities of the 177 galaxies presented in this work (Table A1) are

luminosities (W Hz^{-1}) at 1.5 GHz, an amount +16.18 should be subtracted from the logarithm of the luminosities.

similar to those of the 103 galaxies from Paper I. Compared to previous surveys of the Palomar surveys, the LeMMINGs legacy presents the deepest survey, by extending to lower luminosities by a factor of at least 10 with respect to previous ones (Nagar et al. 2002; Filho et al. 2006; Panessa & Giroletti 2013). It reaches a depth similar to the 15-GHz Palomar survey by Saikia et al. (2018) but our work is on a larger sample of active and inactive galaxies and at lower frequencies. Our legacy program is sensitive to sources about a factor of 100 times more luminous than Sgr A* ($\sim 1 \text{ Jy}$, $\sim 10^{15.5} \text{ W Hz}^{-1}$, Krichbaum et al. 1998), and represents the deepest radio survey of the local Universe at 1.5 GHz.

Table 5 summarises the number of core-identified galaxies, core-unidentified sources, and undetected sources, listed by optical classes. Seyferts have the highest detection rate (13/18, ~ 72.2 per cent) in the sample, a more robust number than that measured in the first data release because of the poor coverage of this class (only 4 Seyferts in Paper I). This fraction is similar to the radio detection rate measured in type-1 Seyferts (72 per cent) from previous VLA studies (Ho 2008). LINERs have the largest number of detections, 58/94, ~ 61.7 per cent, a rate that is comparable to what was achieved in Paper I and similar to what was obtained in previous VLA studies for type-1 LINERs, 63 per cent, (Ho 2008). However we note that our radio detection rates relative to type-II AGN are higher than what measured in previous VLA studies (Ho 2008). HII galaxies have a smaller detection rate, 47/140 (~ 33.6 per cent) and for ALG the detection rate is even lower, at 7/28 (25 per cent). Overall 106/280, or ~ 37.9 per cent of the detected sources are core-identified; 19 detected sources (two ALG, one Seyfert, two LINERs and fourteen HII galaxies) are unidentified. The final identified radio core fractions are therefore: LINERs 56/94 (~ 59.6 per cent), Seyferts 12/18 (~ 66.7 per cent), ALGs 5/28 (~ 17.9 per cent) and HII galaxies 33/140 (~ 23.6 per cent).

The LeMMINGs sample covers all radio morphological types across all of the optical classes (see Table 5). Furthermore, the radio classes which suggest the presence of a radio jet (B, C and D), enclose all the optical classes. LINERs exhibit a variety of morphologies, but are most commonly observed as core/core-jet and triple structures, similar to the ALGs. Seyferts cover the whole variety of morphologies, but with the highest fraction of extended jetted structures among the classes. In contrast, the HII galaxies show primarily compact cores or extended complex structures.

Although HII galaxies are classified as star forming based on their location on the BPT diagrams, the presence of a jet is not precluded in these sources. In fact, there are seven LeMMINGs HII galaxies that show clear ‘jet-like’ morphologies, we refer to them as *jetted* HII galaxies¹³. One of these sources is NGC 3665 which exhibits a Fanaroff-Riley type-I (FR I) radio morphology extended over $\sim 3 \text{ kpc}$ at the VLA scale (Parma et al. 1986). NGC 3504 appears extended in VLBI maps with a core of 3 mJy beam^{-1} (Deller & Middeberg 2014). NGC 7798 shows only a bright core ($\sim 6 \text{ mJy}$) at 8.5 GHz with the VLA (Schmitt et al. 2006). NGC 2782 shows an extended radio source which matches a previous

¹³ The *jetted* HII galaxies are NGC 972, NGC 3665, UGC 3828, NGC 7798, UGC 4028, NGC 2782, and NGC 3504.

Table 5. Spectral–radio morphological classification breakdown of the LeMMINGs sample.

		optical class				
radio class		LINER	ALG	Seyfert	HII	Tot
core identified	core/core-jet (A)	37 (29)	3 (0)	6 (6)	18 (14)	64 (49)
	one-sided jet (B)	2 (2)	0 (0)	1 (1)	2 (0)	5 (3)
	triple (C)	13 (4)	2 (1)	3 (2)	4 (1)	22 (8)
	doubled-lobed (D)	3 (0)	0 (0)	1 (0)	0 (0)	4 (0)
	jet+complex (E)	1 (0)	0 (0)	1 (0)	9 (6)	11 (6)
Tot core-identified		56 (35)	5 (1)	12 (9)	33 (21)	106 (66)
unidentified		2 (1)	2 (1)	1 (0)	14 (10)	19 (12)
Tot detected		58(36)	7(2)	13(9)	47(31)	125(78)
undetected		36 (24)	21 (12)	5 (5)	93 (58)	155 (99)
Tot		94 (60)	28 (14)	18 (14)	140 (89)	280 (177)

Notes. The sample is divided into morphological radio (core/core-jet, one-sided jet, triple, double-lobed source, and complex source) and spectroscopic optical classes (LINER, ALG, Seyfert, HII galaxies) based on their radio detection, core-identification or non-detection. The numbers are related to the total LeMMINGs sample (280 objects), whilst the numbers in parenthesis are related to the sub-sample of 177 galaxies reported here.

e-MERLIN observation with an elongated core (a peak flux density of $1.4 \text{ mJy beam}^{-1}$, lower than our detected value $2.5 \text{ mJy beam}^{-1}$), resolved in a twin-jet morphology by EVN observations (peak flux density of $0.4 \text{ mJy beam}^{-1}$, Krips et al. 2007). The radio emission for the remaining *non-jetted* HII galaxies is more probably related to SF instead of a jet (single cores or complex morphologies).

The brightness temperature (T_B) is the temperature needed for a black-body (thermal) radiator to produce the same specific intensity as the observed point source. In astrophysical phenomena, below 10^5 K , the radio emission can be explained by a large contribution from free-free emission (Condon et al. 1991) but above 10^6 K synchrotron emission from relativistic particles (e.g. from jets or AGN) is required to explain such high brightness temperatures (Condon 1992). Using half the beam width at the *e*-MERLIN resolution at 1.5 GHz as the deconvolved size of the cores (see Table A1), a flux density of $\gtrsim 5 \text{ mJy beam}^{-1}$ corresponds to a $T_B \gtrsim 10^6 \text{ K}$ (Paper I). Twenty-one LeMMINGs galaxies meet this requirement and are associated with all types of radio morphologies observed and are for the majority LINERs. The brightness temperatures broadly reflect the flux density distribution. However, T_B lower than 10^6 K do not preclude an SMBH origin of the radio emission, as weak LLAGN emit low brightness. VLBI observations are required to give a robust measurement of cores’ brightness temperatures.

The luminosity distributions for the LeMMINGs sample are presented in Figure 5: both the peak radio core luminosities and the total luminosities (L_{Tot}) integrated over the radio-emitting region, split by optical class (upper panel) and host type (lower panel). The detected cores have a mean (uncensored) luminosity of $10^{36.10 \pm 0.11} \text{ erg s}^{-1}$. In general, LINERs are among the most luminous sources of the sample, with a censored mean value of $1.8 \times 10^{35 \pm 0.24} \text{ erg s}^{-1}$. Seyferts show the largest mean core luminosity ($2.6 \times 10^{35 \pm 0.26} \text{ erg s}^{-1}$). In contrast, the ALG and HII galaxies have the lowest censored mean core powers, at $5.0 \times 10^{34 \pm 0.30}$ and $3.1 \times 10^{34 \pm 0.17} \text{ erg s}^{-1}$, respectively. Yet, when detected ALGs show the highest core luminosities, $> 10^{36} \text{ erg s}^{-1}$. The undetected/unidentified galaxies have upper-limit radio luminosities between 10^{32} to $10^{37} \text{ erg s}^{-1}$,

Table 6. Spectral–host-radio classification breakdown of the LeMMINGs sample.

		optical class				
host type		LINER	ALG	Seyfert	HII	Tot
elliptical		14 (11)	13 (3)	0 (0)	0 (0)	27 (14)
lenticular		29 (21)	14 (2)	6 (3)	6 (2)	55 (28)
Tot ETG		43 (32)	27 (5)	6 (3)	6 (2)	82 (42)
spirals		50 (23)	1 (0)	12 (9)	122 (29)	185 (61)
irregular		1 (1)	0 (0)	0 (0)	12 (2)	13 (3)
Tot LTG		51 (24)	1 (0)	12 (9)	134 (31)	198 (64)
Tot		94 (56)	28 (5)	18 (12)	140 (33)	280 (106)

Notes. The sample is divided into galaxy types (elliptical and lenticular [ETG], spiral and irregular [LTG]) and spectroscopic optical classes (LINER, ALG, Seyfert, HII galaxies) based on their radio detection. The numbers in parenthesis are related to the sub-sample of 106 core-identified galaxies.

with a median radio luminosity of $9.06 \times 10^{34 \pm 0.07} \text{ erg s}^{-1}$. The different median luminosities of the optical classes are not due to different sensitivities or distances because the sources are randomly distributed in the space volume of the survey and observed in similar conditions.

In analogy to the core luminosities, the total luminosities estimated from the low-resolution radio images for the 177 galaxies described in this work (Table A1) are comparable with the values obtained from the first sub-sample from Paper I (Fig. 5): the median value is $4 \times 10^{36} \text{ erg s}^{-1}$. The total luminosities equal the core luminosities in case of an unresolved core or can be larger up to a factor 100 in case of bright extended emission (see Table A1). LINERs and Seyferts are once again the most powerful radio sources and the HII galaxies are the weakest. The core dominance, defined as the ratio of the radio core power to the total flux density changes with each class, but has a large variance: LINERs and ALGs are the most core dominated (~ 75 per cent), followed by Seyferts with moderate core dominance (~ 40 per cent), whereas the HII galaxies have the smallest core dominance (~ 35 per cent) (Figure 5, upper panel). On average the radio core contributes half of the total radio emission.

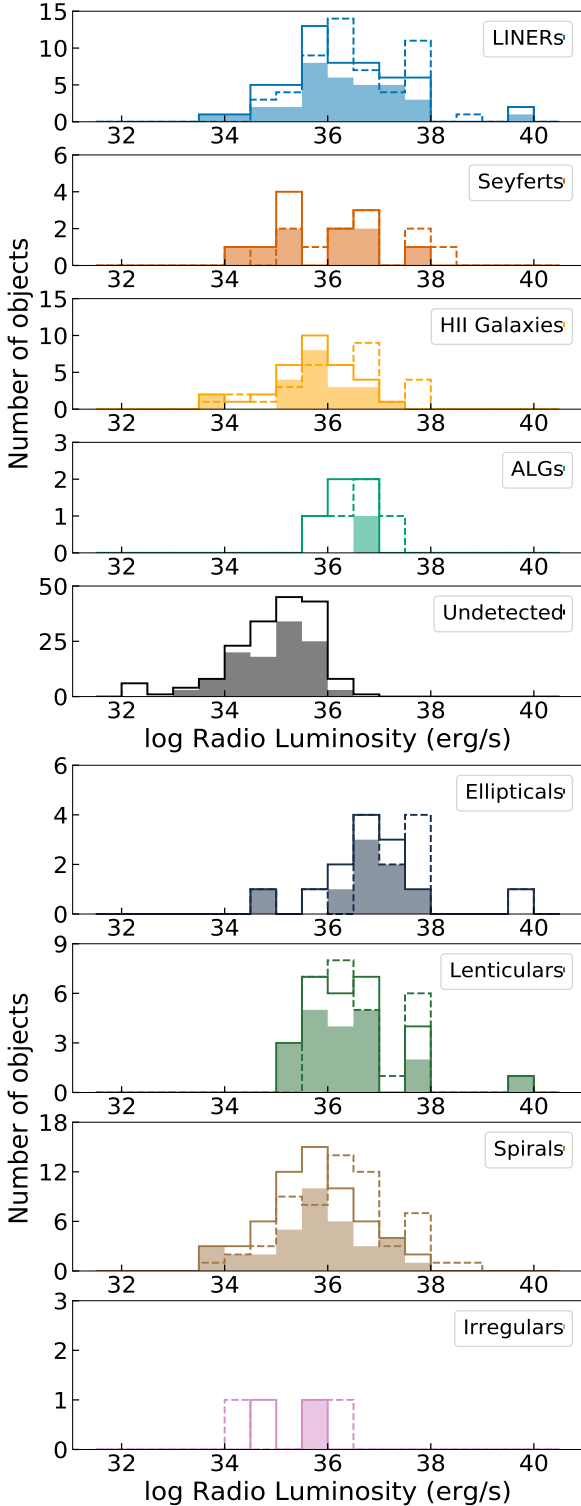


Figure 5. Radio luminosity distribution (erg s^{-1}) divided per optical class (upper figure) and host morphological type (lower figure). The radio core luminosity and the total radio luminosity distributions are outlined by the solid-line and the dashed-line histograms, respectively. The bottom panel of the upper figure depicts the 3σ upper-limit radio luminosity distribution for the undetected and unidentified sources. The filled histogram represents the 177 sources presented in this work. To convert the radio luminosities from erg s^{-1} to W Hz^{-1} at 1.5 GHz, an amount +16.18 should be subtracted from the logarithm of the luminosities presented in the graph.

In terms of the host morphological classes (see Table 6), although spiral galaxies are the most abundant host type in the LeMMINGs sample (185/280, ~ 66 per cent), approximately 33 per cent of spiral galaxies are core-detected and are associated with all types of radio morphology. Detected spirals host Seyfert, LINERs and HII galaxies in decreasing order of radio fraction. Of the 13 irregular galaxies in our sample, three are core-detected in our radio survey and host LINER or HII galaxies. Conversely, ellipticals and lenticulars are the most detected radio sources (~ 51 per cent) and are usually associated with the jetted radio morphologies. LINERs in ETGs have the highest core detection fraction. In summary, approximately one third of LTGs (spiral and irregular) and half of the ETGs (elliptical and lenticular) are detected in our survey. In terms of radio luminosities, Figure 5, lower panel, depicts the radio luminosity distribution per host type. Ellipticals and lenticulars show the highest radio luminosities ($\sim 10^{35-40} \text{ erg s}^{-1}$). Spiral galaxies have intermediate radio luminosities of $\sim 10^{36} \text{ erg s}^{-1}$. The irregular galaxies have the lowest core and total luminosities.

6 DISCUSSION

6.1 CASA versus AIPS

In this work we present the *e*-MERLIN observations of 177 Palomar galaxies from the LeMMINGs survey. The data were calibrated with CASA which is different from the 103 sources presented in Paper I which were analysed with AIPS. The rms noise distribution of the resulting maps presented here is not statistically different from the values obtained with AIPS. However, for a single observation block calibrated with both software packages, the rms noise from CASA is lower than that from AIPS whereas the integrated flux densities obtained from the maps are consistent with each other to within a 20 per cent calibration error. Moreover, we note marginal differences in terms of low-brightness structures between the maps created with AIPS and CASA procedures, with the latter exhibiting neater radio structures than the former. This implies that caution is required when interpreting faint radio sources.

A potential difference in rms noise between the two calibration techniques could skew the 3σ detection limit so as to have more galaxies detected in the CASA sample. However, this can not be reconciled with the slightly higher detection fraction of galaxies mapped with AIPS (45.6 per cent) than in this work where we used CASA (44.6 per cent). However, if one considers these detection statistics as a binomial distribution, the detection fractions of the two sub-samples presented in Paper I and here are consistent with one another within $\lesssim 1$ per cent. In conclusion, the two calibration methods produce generally consistent flux densities and radio structures, which minimise a possible bias in the results.

6.2 General characteristics of the survey

The LeMMINGs survey stands for the deepest radio study of the local Universe represented by the Palomar galaxy sample, reaching an average rms noise of $\sim 0.8 \text{ mJy beam}^{-1}$. More importantly, the LeMMINGs sample probes pc-scale activity in all types of galaxies, irrespective of the nuclear

properties set by their optical emission line ratios. This characteristic makes the LeMMINGs survey unbiased towards the presence of an active SMBH and different from previous programs which partially focused only on Seyferts and LINERs.

Of the complete sample of 280 Palomar galaxies, 125 sources (~ 44.6 per cent) were detected. This corresponds to a detection rate similar to previous VLA/VLBA campaigns of the Palomar active galaxies (see [Ho 2008](#) for a review). For 106/280 (~ 37.9 per cent) of the sample, radio emission has been detected within the central 1.2 arcsec from the galaxies' optical centre, possibly due to a radio-emitting active nucleus.

Direct comparison with previous radio studies is non-trivial since it was decided to reclassify all galaxies based on the updated BPT diagrams. Nonetheless, more than half of the LINERs and Seyferts, i.e. of the line-emitting active galaxies, in our sample show compact radio core or jetted structures. Previous VLA campaigns targeting active galaxies detected radio emission in half of them (e.g. [Nagar et al. 2000](#)), with a more prominent detection fraction for Seyferts and type-I AGN in general. One quarter of the detected sources which are not identified as powered by active SMBH by their emission-line ratios show evident jetted structures (one-side, twin jets, triple and double sources), excluding those with complex morphology. This corroborates the idea that at least one fourth (~ 28.6 per cent) of the Palomar galaxies emit pc-scale radio emission possibly related to a LLAGN. If we include those sources with a intricate radio morphology which could hide jet emission, and also the core-jet HII galaxies, the possible fraction of radio-emitting LLAGN rises to one third (~ 32.5 per cent).

The most common radio morphology observed in the LeMMINGs galaxies with centrally detected radio emissions is the core/core-jet morphology (64/106). This is unsurprising as the high-resolution of *e*-MERLIN can resolve out some of the diffuse emission associated with jets and star-forming regions. The nature of these unresolved radio components, whether an unresolved radio jet base or a star-forming nuclear region on scales of < 100 pc, can be explored by using further diagnostics such as [O III] and X-ray luminosities when clear jet-like structures lack. We will discuss the radio core origin per optical class in upcoming papers.

Half of the early-type galaxies (elliptical and lenticular) in the LeMMINGs sample host a radio source coincident with the optical centre, that is determined to be an active SMBH. Regarding late-type galaxies (spirals and irregulars) ~ 32 per cent has a radio-emitting central active SMBH. Quantitatively, the detection fraction decreases with later Hubble type, as only ~ 17 per cent of Sc–Sd galaxies are detected. Hence, the LeMMINGs survey agrees with the basic results of previous radio studies of the nearby galaxies ([Ho & Ulvestad 2001](#); [Ulvestad & Ho 2001a](#); [Nagar et al. 2005](#); [Ho 2008](#)), which detected flat-spectrum radio cores predominantly at the centre of massive (typically early-type) galaxies ([Sadler et al. 1989](#); [Wrobel & Heeschen 1991](#); [Capetti et al. 2009](#); [Miller et al. 2009](#); [Nyland et al. 2016](#)).

6.3 Radio evidence of nuclear star formation

In our Legacy survey only a small number of galaxies show evidence of intense bursts of SF, based on the ra-

dio properties. The clearest examples are the well-known galaxies/systems M 82 and Arp 299. Only three sources (NGC 4013, NGC 4102, and NGC 5273) clearly exhibit diffuse low-brightness radio emission, consistent with a stellar disc or ring, similar to what is expected from diffuse extended star forming galaxies ([Muxlow et al. 2010](#); [Murphy et al. 2018](#); [Herrero-Illana et al. 2017](#)). Single radio components were detected at the centre of most of HII galaxies. We note that complex radio morphologies, unidentified off-nuclear sources and non-jetted galaxies might conceal nuclear star-forming regions, though. Furthermore, ambiguous morphologies (see e.g. NGC 2964, NGC 2273, NGC 2639) might be caused by the interaction of a jet with a dense ISM, which in turn could trigger SF ([Silk 2005](#); [Gaibler et al. 2012](#)).

The very low fraction of clear star forming regions observed in our survey is most probably due to the sparse $u-v$ coverage of the observations because of the long baselines of *e*-MERLIN and of the snapshot imaging technique of our program. For most of the sample, which is further than ~ 4 Mpc, the spatial frequencies covered by *e*-MERLIN are appropriate to detect compact bright young SN/SNR and HII regions (< 400 – 500 yr, [Westcott et al. 2017](#)) and are not suited for detecting diffuse, low-brightness radio emission ($T_B < 10^5$ K), typical of old SNR. At distances $\lesssim 4$ Mpc, VLA data are required to study long-lived diffuse HII complexes, which instead would be resolved out with *e*-MERLIN. We have estimated that our *e*-MERLIN observations can lose up to 75 per cent of the radio structures detected with VLA with 1-arcsec resolution. In fact, adding shorter spacing (VLA) data to *e*-MERLIN visibilities will thus increase the ability to detect more diffuse lower surface brightness emission from SF products. Dedicated deep *e*-MERLIN radio observations combined with shorter-baseline datasets of compact star forming regions, similar to that performed on M 82 ([Wills et al. 1999](#); [Muxlow et al. 2010](#)) has the potential to diagnose the nature of the radio emission in HII galaxies. This will be the goal of one of our future works.

7 SUMMARY AND CONCLUSIONS

This paper present the second data release from the *e*-MERLIN legacy survey, LeMMINGs, aimed at studying a sample of nearby 280 (active and quiescent) galaxies. Here we show the observations of 177 sources from the Palomar sample ([Ho et al. 1997](#)) at 1.5 GHz. By combining this release with the first one ([Baldi et al. 2018](#)), the complete survey represents the deepest, least unbiased view of the galactic nuclei of the local Universe (< 110 Mpc) in the radio band, reaching a sensitivity of ~ 0.80 mJy beam $^{-1}$ and an angular resolution of ~ 150 mas, which corresponds to a physical scale of $\lesssim 100$ pc. This program revealed a large population of local radio-emitting LLAGN and nuclear starbursts ($\lesssim 10^{17.6}$ W Hz $^{-1}$).

After updating the optical spectroscopic classifications of the 280 galaxies of the survey, the entire sample consists of 94 LINERs, 18 Seyferts, 140 HII galaxies and 26 ALG.

Our radio survey has detected significant radio emission with flux densities $\gtrsim 0.25$ mJy in the innermost region (0.73 arcmin 2) of 125 galaxies (44.6 per cent): 58/94 LINERs, 16/18 Seyferts, 47/140 HII galaxies and 7/28 ALGs. For 106 of the 125 detected sources we identified the core

within the radio structure, spatially associated with the optical galaxy centre. We resolved parsec-scale radio structures with a broad variety of morphologies: core/core-jet, one-sided jet, triple sources, twin jets, double-lobed, and complex shapes with sizes of 3 – 6600 pc. The compact cores (64/106) are the most common morphology. There are 31 sources with clear jets, roughly half (18/31) of which are LINERs. This jet fraction could be higher because the complex morphologies (11/106) could possibly hide diffuse jets interacting with the ISM, similar to what is seen in nearby LLAGN and star forming galaxies (e.g. Mould et al. 2000; Croft et al. 2006; Gaibler et al. 2012).

The detected radio cores have been interpreted as a sign of nuclear activity and their luminosities range between $\sim 10^{34}$ and 10^{40} erg s $^{-1}$. The lower end of this interval explicits the depth of this survey, greater than that reached by previous radio surveys, $\sim 10^{35}$ erg s $^{-1}$ (Nagar et al. 2005; Filho et al. 2006). The total radio luminosities determined by integrating the extended radio structures are on average double the core radio luminosities, although they can be up to a factor of 100 times the core luminosity for jetted sources and those with complex morphologies.

Concerning the host type, approximately half of the early-type galaxies and one third of the late-type galaxies are detected in our survey. The jetted sources are typically related to elliptical, lenticulars or bulged-dominated spirals.

Based only on the radio properties (brightness temperatures, luminosities, morphologies) and spectroscopic classification, the origin of the radio emission from the LeMMINGs galaxies is probably ascribed to active SMBHs in one third of the sample, precisely in the generic population of LINER and Seyferts. Conversely, SF is the most plausible physical process of radio-emission production in HII galaxies. For ALG the nature of the radio emission is more controversial, but the lack of clear SF favours an AGN origin. Nonetheless, adding multi-band data to the radio analysis will better address the question on the nature of the radio emission in each single galaxy and will be subject of upcoming papers.

LINERs reveal narrow structures of rapidly declining brightness at increasing distance from the nucleus, i.e. core-brightened morphology, similar to small FR I radio galaxies. They have the highest brightness temperatures (some $> 10^6$ K) and are among the most luminous galaxies, suggesting a synchrotron emission from a (mildly?) relativistic jet. They tend to live in ellipticals and lenticulars, another analogy with classical radio-loud AGN (Heckman & Best 2014).

Seyferts exhibit the highest fraction of detections and double-lobed radio outflows, echoing the ‘edge-brightened’ morphology observed in nearby radio-quiet Seyferts (e.g. Kukula et al. 1995; Wrobel 2000). Along with LINERs, they are among the most luminous sources of the sample and are found in both galaxy types but more frequently in late types. Similar to the conclusion in Paper I regarding Seyferts, their symmetric (two-sided) radio morphology and their association with spirals recall the ‘spin paradigm’ (Wilson & Colbert 1995; Sikora et al. 2007; Tchekhovskoy et al. 2010; Dotti et al. 2013) which suggests that SMBH in spiral/disc galaxies may host (on average) lower-spinning SMBHs than those in giant elliptical galaxies. This argument has been interpreted as one of the possible conditions which prevents from launching faster jets in late-type galaxies than in early-type galaxies, although largely under debate.

We typically detected the cores of HII galaxies, with brightness temperature $< 10^6$ K and with sub-kpc sizes, probably representing nuclear starburst as similar to local star-forming galaxies (e.g. Herrero-Illana et al. 2017). Although this class encompasses the least luminous objects, a small sub-group of seven HII galaxies is associated with core-brightened jetted structures similar to jets seen in LINERs. This association suggests the presence of an active SMBH, optically outshined by the nuclear SF, but able to support the launch of a jet. These star forming galaxies with active nuclei are still consistent with the picture of LLAGN (Nagar et al. 2001; Ulvestad & Ho 2001b). In addition, HII galaxies have the highest fraction of complex morphologies and multiple components (see M 82 and Arp 299), plausibly related to diffuse SF and SN factories.

Only 7 out of 28 ALGs have been detected and only 2 reveal clear jets. They are typically associated with massive ellipticals and when detected, they are the most luminous sources. Their radio and host properties are similar to those of the LINER population (Baldi & Capetti 2010). The absence of a clear emission-line nucleus and their low radio activity chime with a picture of a population of evolved galaxies with dormant SMBHs which occasionally trigger AGN activity (Morganti 2017).

The nuclear components revealed by our *e*-MERLIN survey suggest that the detected pc-scale radio cores, which unlike in previous radio surveys could now be resolved, represent the brightest and main parts of the entire galaxy. In one third of the nuclei the emission can plausibly be ascribed to a central, active SMBH in a low-accretion stage and/or to a disc emitting at low-radiative efficiency, as expected in LLAGN able to launch pc-scale jets (Ho 2008; Mezcua & Prieto 2014). However, it is clear that sub-mJy radio cores can conceal both strong SF and an active, low-brightness SMBH (Padovani 2016), even in a flaring or dimming stage of accretion, such as in the case of a TDE, as observed in our target NGC 3690 (Arp 299, Mattila et al. 2018). Therefore, by eventually disentangling SF and SMBH activity and assessing the origin of the radio emission at the centre of our galaxies, the next LeMMINGs papers will make use of the optical and X-ray data along with our radio observations to address the following astrophysical open issues: the disc-jet connection in LLAGN (Merloni et al. 2003), the contribution from SF (stellar processes and XRBs) in the GHz band and possible core variability due to transient phenomena (Mundell et al. 2009; Alexander et al. 2020).

ACKNOWLEDGEMENTS

The authors thank the anonymous referee for his/her helpful comments to improve the manuscript. AA and MAPT acknowledge support from the Spanish MCIU through grant PGC2018-098915-B-C21 and from the State Agency for Research of the Spanish MCIU through the “Center of Excellence Severo Ochoa” award for the Instituto de Astrofísica de Andalucía (SEV-2017-0709). B.T.D acknowledges support from a Spanish postdoctoral fellowship ‘Ayudas 1265 para la atracción del talento investigador. Modalidad 2: jóvenes investigadores.’ funded by Comunidad de Madrid under grant number 2016-T2/TIC-2039. B.T.D also acknowledges support from grant ‘Ayudas para la real-

ización de proyectos de I+D para jóvenes doctores 2019.’ funded by Comunidad de Madrid and Universidad Complutense de Madrid under grant number PR65/19-22417. J.H.K. acknowledges financial support from the European Union’s Horizon 2020 research and innovation programme under Marie Skłodowska-Curie grant agreement No 721463 to the SUNDIAL ITN network, from the State Research Agency (AEI-MCINN) of the Spanish Ministry of Science and Innovation under the grant ”The structure and evolution of galaxies and their central regions” with reference PID2019-105602GB-I00/10.13039/501100011033, and from IAC project P/300724, financed by the Ministry of Science and Innovation, through the State Budget and by the Canary Islands Department of Economy, Knowledge and Employment, through the Regional Budget of the Autonomous Community. JSG thanks the University of Wisconsin-Madison and its Foundation for support of this research through his Ruppel Bascom Professorship. FS acknowledges partial support from a Leverhulme Trust Research fellowship. CGM acknowledges support from the University of Bath and Jim and Hiroko Sherwin. *e*-MERLIN is a National Facility operated by the University of Manchester at Jodrell Bank Observatory on behalf of STFC, part of UK Research and Innovation.

DATA AVAILABILITY

The data on which this paper is based are publicly available from the *e*-MERLIN archive. Calibrated image products are available upon reasonable request to the corresponding author. These, along with other LeMMINGS survey products, will be publicly hosted in association with upcoming publications.

REFERENCES

- Alexander K. D., van Velzen S., Horesh A., Zauderer B. A., 2020, *Space Sci. Rev.*, **216**, 81
- Allen M. G., Groves B. A., Dopita M. A., Sutherland R. S., Kewley L. J., 2008, *ApJS*, **178**, 20
- Aller M. C., Richstone D., 2002, *AJ*, **124**, 3035
- Alonso-Herrero A., Rieke G. H., Rieke M. J., Scoville N. Z., 2000, *ApJ*, **532**, 845
- Anastasopoulou K., Zezas A., Ballo L., Della Ceca R., 2016, *MNRAS*, **460**, 3570
- Baldi R. D., Capetti A., 2009, *A&A*, **508**, 603
- Baldi R. D., Capetti A., 2010, *A&A*, **519**, A48
- Baldi R. D., et al., 2018, *MNRAS*, **476**, 3478 (Paper I)
- Baldwin J. A., Phillips M. M., Terlevich R., 1981, *PASP*, **93**, 5
- Balmaverde B., Capetti A., 2013, *A&A*, **549**, A144
- Barausse E., Shankar F., Bernardi M., Dubois Y., Sheth R. K., 2017, *MNRAS*, **468**, 4782
- Battye R. A., et al., 2020, *MNRAS*, **495**, 1706
- Beasley A. J., Gordon D., Peck A. B., Petrov L., MacMillan D. S., Fomalont E. B., Ma C., 2002, *ApJS*, **141**, 13
- Bennett A. S., 1962, *Mem. RAS*, **68**, 163
- Beswick R. J., et al., 2006, *MNRAS*, **369**, 1221
- Beswick R., Argo M. K., Evans R., McHardy I., Williams D. R. A., Westcott J., 2014, in *Proceedings of the 12th European VLBI Network Symposium and Users Meeting (EVN 2014)*. 7-10 October 2014. Cagliari, Italy. p. 10
- Blandford R., Meier D., Readhead A., 2019, *ARA&A*, **57**, 467
- Bondi M., Pérez-Torres M. A., Herrero-Illana R., Alberdi A., 2012, *A&A*, **539**, A134
- Brown R. H., Hazard C., 1961, *MNRAS*, **122**, 479
- Brunthaler A., et al., 2010, *A&A*, **516**, A27
- Buttiglione S., Capetti A., Celotti A., Axon D. J., Chieaberge M., Macchetto F. D., Sparks W. B., 2010, *A&A*, **509**, A6
- Capetti A., Baldi R. D., 2011, *A&A*, **529**, A126
- Capetti A., Kharb P., Axon D. J., Merritt D., Baldi R. D., 2009, *AJ*, **138**, 1990
- Carilli C. L., Wrobel J. M., Ulvestad J. S., 1998, *AJ*, **115**, 928
- Cazzoli S., et al., 2018, *MNRAS*, **480**, 1106
- Chen C. T. J., et al., 2017, *ApJ*, **837**, 48
- Condon J. J., 1992, *ARA&A*, **30**, 575
- Condon J. J., Huang Z.-P., Yin Q. F., Thuan T. X., 1991, *ApJ*, **378**, 65
- Connolly S. D., McHardy I. M., Skipper C. J., Emmanoulopoulos D., 2016, *MNRAS*, **459**, 3963
- Conway J. E., Myers S. T., Pearson T. J., Readhead A. C. S., Unwin S. C., Xu W., 1994, *ApJ*, **425**, 568
- Croft S., et al., 2006, *ApJ*, **647**, 1040
- Deller A. T., Middelberg E., 2014, *AJ*, **147**, 14
- Dotti M., Colpi M., Pallini S., Perego A., Volonteri M., 2013, *ApJ*, **762**, 68
- Dullo B. T., et al., 2018, *MNRAS*, **476**, 3478
- Falcke H., Nagar N. M., Wilson A. S., Ulvestad J. S., 2000, *ApJ*, **542**, 197
- Fenech D. M., Muxlow T. W. B., Beswick R. J., Pedlar A., Argo M. K., 2008, *MNRAS*, **391**, 1384
- Fenech D., Beswick R., Muxlow T. W. B., Pedlar A., Argo M. K., 2010, *MNRAS*, **408**, 607
- Ferrarese L., Merritt D., 2000, *ApJL*, **539**, L9
- Filho M. E., Barthel P. D., Ho L. C., 2000, *ApJS*, **129**, 93
- Filho M. E., Barthel P. D., Ho L. C., 2006, *A&A*, **451**, 71
- Filippenko A. V., Sargent W. L. W., 1985, *ApJS*, **57**, 503
- Florido E., Pérez I., Zurita A., Sánchez-Blázquez P., 2012, *A&A*, **543**, A150
- Gaibler V., Khochfar S., Krause M., Silk J., 2012, *MNRAS*, **425**, 438
- García-Lorenzo B., et al., 2015, *A&A*, **573**, A59
- Gavazzi G., Consolandi G., Dotti M., Fossati M., Savorgnan G., Gualandri R., Bruni I., 2013, *A&A*, **558**, A68
- Gavazzi G., Consolandi G., Belladitta S., Boselli A., Fossati M., 2018, *A&A*, **615**, A104
- Gebhardt K., et al., 2000, *ApJL*, **539**, L13
- Gendre M. A., Fenech D. M., Beswick R. J., Muxlow T. W. B., Argo M. K., 2013, *MNRAS*, **431**, 1107
- Girichidis P., et al., 2020, *Space Sci. Rev.*, **216**, 68
- Graham A. W., Scott N., 2013, *ApJ*, **764**, 151
- Greisen E. W., 2003, *AIPS*, the VLA, and the VLBA. p. 109, doi:10.1007/0-306-48080-8.7
- Heckman T. M., 1980, *A&A*, **500**, 187
- Heckman T. M., Best P. N., 2014, *ARA&A*, **52**, 589
- Herrero-Illana R., et al., 2017, *MNRAS*, **471**, 1634
- Ho L. C., 1999, *ApJ*, **516**, 672
- Ho L. C., 2008, *ARA&A*, **46**, 475
- Ho L. C., Ulvestad J. S., 2001, *ApJS*, **133**, 77
- Ho L. C., Filippenko A. V., Sargent W. L. W., 1993, *ApJ*, **417**, 63
- Ho L. C., Filippenko A. V., Sargent W. L. W., 1995, *ApJS*, **98**, 477
- Ho L. C., Filippenko A. V., Sargent W. L. W., 1997, *ApJS*, **112**, 315
- Högbom J. A., 1974, *A&AS*, **15**, 417
- Hummel E., Fanti C., Parma P., Schilizzi R. T., 1982, *A&A*, **114**, 400
- Kankare E., et al., 2014, *MNRAS*, **440**, 1052
- Kaplan E. L., Meier P., 1958, *Journal of the American Statistical Association*, **53**, 457
- Kauffmann G., Heckman T. M., 2009, *MNRAS*, **397**, 135

- Keel W. C., 1983, *ApJ*, **269**, 466
- Kennicutt R., 1983, *A&A*, **120**, 219
- Kennicutt R. C., 1992, *ApJ*, **388**, 310
- Kettenis M., van Langevelde H. J., Reynolds C., Cotton B., 2006, in Gabriel C., Arviset C., Ponz D., Enrique S., eds, *Astronomical Society of the Pacific Conference Series Vol. 351, Astronomical Data Analysis Software and Systems XV*. p. 497
- Kewley L. J., Groves B., Kauffmann G., Heckman T., 2006, *MNRAS*, **372**, 961
- Kimani N., et al., 2016, *A&A*, **593**, A18
- Krichbaum T. P., et al., 1998, *A&A*, **335**, L106
- Krips M., et al., 2007, *A&A*, **464**, 553
- Kukula M. J., Pedlar A., Baum S. A., O’Dea C. P., 1995, *MNRAS*, **276**, 1262
- Laor A., Behar E., 2008, *MNRAS*, **390**, 847
- Leonidaki I., Zezas A., Boumis P., 2010, *ApJ*, **725**, 842
- Linden S. T., Murphy E. J., Dong D., Momjian E., Kennicutt R. C. J., Meier D. S., Schinnerer E., Turner J. L., 2020, *ApJS*, **248**, 25
- Lira P., Johnson R. A., Lawrence A., Cid Fernandes R., 2007, *MNRAS*, **382**, 1552
- Maoz D., 2007, *MNRAS*, **377**, 1696
- Marconi A., Risaliti G., Gilli R., Hunt L. K., Maiolino R., Salvati M., 2004, *MNRAS*, **351**, 169
- Marleau F. R., Clancy D., Habas R., Bianconi M., 2017, *A&A*, **602**, A28
- Mattila S., et al., 2018, *Science*, **361**, 482
- McMullin J. P., Waters B., Schiebel D., Young W., Golap K., 2007, in Shaw R. A., Hill F., Bell D. J., eds, *Astronomical Society of the Pacific Conference Series Vol. 376, Astronomical Data Analysis Software and Systems XVI*. p. 127
- Menci N., Fiore F., Perola G. C., Cavaliere A., 2004, *ApJ*, **606**, 58
- Merloni A., Heinz S., di Matteo T., 2003, *MNRAS*, **345**, 1057
- Mezcua M., Prieto M. A., 2014, *ApJ*, **787**, 62
- Miller N. A., Hornschemeier A. E., Mobasher B., Bridges T. J., Hudson M. J., Marzke R. O., Smith R. J., 2009, *AJ*, **137**, 4450
- Morganti R., 2017, *Nature Astronomy*, **1**, 596
- Mould J. R., et al., 2000, *ApJ*, **536**, 266
- Moustakas J., Kennicutt Jr. R. C., 2006, *ApJS*, **164**, 81
- Mundell C. G., Ferruit P., Nagar N., Wilson A. S., 2009, *ApJ*, **703**, 802
- Murphy E. J., Dong D., Momjian E., Linden S., Kennicutt R. C. J., Meier D. S., Schinnerer E., Turner J. L., 2018, *ApJS*, **234**, 24
- Muxlow T. W. B., Pedlar A., Wilkinson P. N., Axon D. J., Sanders E. M., de Bruyn A. G., 1994, *MNRAS*, **266**, 455
- Muxlow T. W. B., Pedlar A., Beswick R. J., Argo M. K., O’Brien T. J., Fenech D., Trotman W., 2005, *Mem. Soc. Astron. Italiana*, **76**, 586
- Muxlow T. W. B., et al., 2010, *MNRAS*, **404**, L109
- Nagar N. M., Falcke H., Wilson A. S., Ho L. C., 2000, *ApJ*, **542**, 186
- Nagar N. M., Wilson A. S., Falcke H., 2001, *ApJ*, **559**, L87
- Nagar N. M., Falcke H., Wilson A. S., Ulvestad J. S., 2002, *A&A*, **392**, 53
- Nagar N. M., Falcke H., Wilson A. S., 2005, *A&A*, **435**, 521
- Neff S. G., Ulvestad J. S., Teng S. H., 2004, *ApJ*, **611**, 186
- Nyland K., et al., 2016, *MNRAS*, **458**, 2221
- Offringa A. R., van de Gronde J. J., Roerdink J. B. T. M., 2012, *A&A*, **539**, A95
- Padovani P., 2016, *A&A Rev.*, **24**, 13
- Panessa F., Giroletti M., 2013, *MNRAS*, **432**, 1138
- Panessa F., Barcons X., Bassani L., Cappi M., Carrera F. J., Ho L. C., Pellegrini S., 2007, *astro-ph/0701546*,
- Panessa F., Baldi R. D., Laor A., Padovani P., Behar E., McHardy I., 2019, *Nature Astronomy*, **3**, 387
- Parma P., de Ruiter H. R., Fanti C., Fanti R., 1986, *A&AS*, **64**, 135
- Peck L. W., Fenech D. M., 2013, *Astronomy and Computing*, **2**, 54
- Pérez-Torres M. A., Romero-Cañizales C., Alberdi A., Polatidis A., 2009, *A&A*, **507**, L17
- Pérez-Torres M. A., Alberdi A., Romero-Cañizales C., Bondi M., 2010, *A&A*, **519**, L5
- Peterson B. M., 2014, *Space Sci. Rev.*, **183**, 253
- Pişmiş P., Colombón L., Mampaso A., Manteiga M., 2001, *Ap&SS*, **276**, 539
- Ptak A., et al., 2015, *ApJ*, **800**, 104
- Rampadarath H., et al., 2018, *MNRAS*, **476**, 2876
- Rau U., Cornwell T. J., 2011, *A&A*, **532**, A71
- Reines A. E., Greene J. E., Geha M., 2013, *ApJ*, **775**, 116
- Reines A. E., Reynolds M. T., Miller J. M., Sivakoff G. R., Greene J. E., Hickox R. C., Johnson K. E., 2016, *ApJ*, **830**, L35
- Rich J. A., Kewley L. J., Dopita M. A., 2014, *ApJ*, **781**, L12
- Romero-Cañizales C., Mattila S., Alberdi A., Pérez-Torres M. A., Kankare E., Ryder S. D., 2011, *MNRAS*, **415**, 2688
- Romero-Cañizales C., et al., 2014, *MNRAS*, **440**, 1067
- Rosa-González D., 2005, *MNRAS*, **364**, 1304
- Sadler E. M., Jenkins C. R., Kotanyi C. G., 1989, *MNRAS*, **240**, 591
- Saikia P., Körding E., Coppejans D. L., Falcke H., Williams D., Baldi R. D., McHardy I., Beswick R., 2018, *A&A*, **616**, A152
- Sandage A., Tammann G. A., 1981, *Carnegie Inst. of Washington*, p. 0
- Sarzi M., et al., 2010, *MNRAS*, **402**, 2187
- Schmitt H. R., Calzetti D., Armus L., Giavalisco M., Heckman T. M., Kennicutt R. C. J., Leitherer C., Meurer G. R., 2006, *ApJS*, **164**, 52
- Schulze A., Wisotzki L., 2010, *A&A*, **516**, A87
- Serra P., Trager S. C., Oosterloo T. A., Morganti R., 2008, *A&A*, **483**, 57
- Shankar F., Salucci P., Granato G. L., De Zotti G., Danese L., 2004, *MNRAS*, **354**, 1020
- Shankar F., Marulli F., Mathur S., Bernardi M., Bournaud F., 2012, *A&A*, **540**, A23
- Shankar F., Weinberg D. H., Miralda-Escudé J., 2013, *MNRAS*, **428**, 421
- Shankar F., et al., 2016, *MNRAS*, **460**, 3119
- Shankar F., et al., 2019, *Nature Astronomy*, p. 503
- Shields J. C., et al., 2007, *ApJ*, **654**, 125
- Sikora M., Stawarz L., Lasota J.-P., 2007, *ApJ*, **658**, 815
- Silk J., 2005, *MNRAS*, **364**, 1337
- Singh R., et al., 2013, *A&A*, **558**, A43
- Sliwa K., Wilson C. D., Petitpas G. R., Armus L., Juvela M., Matsushita S., Peck A. B., Yun M. S., 2012, *ApJ*, **753**, 46
- Soltan A., 1982, *MNRAS*, **200**, 115
- Tarchi A., Castangia P., Henkel C., Surcis G., Menten K. M., 2011, *A&A*, **525**, A91
- Tchekhovskoy A., Narayan R., McKinney J. C., 2010, *ApJ*, **711**, 50
- Tremaine S., et al., 2002, *ApJ*, **574**, 740
- Ulvestad J. S., 2009, *AJ*, **138**, 1529
- Ulvestad J. S., Ho L. C., 2001a, *ApJ*, **558**, 561
- Ulvestad J. S., Ho L. C., 2001b, *ApJ*, **562**, L133
- Varenus E., et al., 2015, *A&A*, **574**, A114
- Wegner G., Salzer J. J., Jangren A., Gronwall C., Melbourne J., 2003, *AJ*, **125**, 2373
- Westcott J., et al., 2017, *MNRAS*, **467**, 2113
- Williams D. R. A., et al., 2017, *MNRAS*, **472**, 3842
- Williams D. R. A., et al., 2019, *MNRAS*, **486**, 4962
- Wills K. A., Redman M. P., Muxlow T. W. B., Pedlar A., 1999, *MNRAS*, **309**, 395
- Wilson A. S., Colbert E. J. M., 1995, *ApJ*, **438**, 62
- Woltjer L., 1959, *ApJ*, **130**, 38

- Wrobel J. M., 2000, *ApJ*, **531**, 716
Wrobel J. M., Heeschen D. S., 1991, *AJ*, **101**, 148
Zakamska N. L., Greene J. E., 2014, *MNRAS*, **442**, 784
de Vaucouleurs G., de Vaucouleurs A., Corwin J. R., 1976, in
Second reference catalogue of bright galaxies, Vol. 1976, p.
Austin: University of Texas Press..
de Vaucouleurs G., de Vaucouleurs A., Corwin Jr. H. G., Buta
R. J., Paturel G., Fouqué P., 1991, Third Reference Catalogue
of Bright Galaxies. Volume I: Explanations and references.
Volume II: Data for galaxies between 0^h and 12^h . Volume III:
Data for galaxies between 12^h and 24^h .
van Bemmell I., Small D., Kettenis M., Szomoru A., Moellenbrock
G., Janssen M., 2019, preprint, ([arXiv:1904.11747](https://arxiv.org/abs/1904.11747))
van den Bosch R. C. E., Gebhardt K., Gültekin K., Yıldırım A.,
Walsh J. L., 2015, *ApJS*, **218**, 10

AFFILIATIONS

- ¹ Istituto di Radioastronomia - INAF, Via P. Gobetti 101,
I-40129 Bologna, Italy
² School of Physics and Astronomy, University of Southamp-
ton, Southampton, SO17 1BJ, UK
³ Dipartimento di Fisica, Università degli Studi di Torino,
via Pietro Giuria 1, 10125 Torino, Italy
⁴ INAF - Istituto di Astrofisica e Planetologia Spaziali, via
Fosso del Cavaliere 100, I-00133 Roma, Italy
⁵ Jodrell Bank Centre for Astrophysics, School of Physics
and Astronomy, The University of Manchester, Manchester,
M13 9PL, UK
⁶ Department of Physics, University of Oxford, Denys
Wilkinson Building, Keble Road, Oxford, OX1 3RH, UK
⁷ Centre for Astrophysics Research, University of Hertford-
shire, College Lane, Hatfield, AL10 9AB, UK
⁸ Departamento de Astrofísica y Ciencias de la Atmosfera,
Universidad Complutense de Madrid, E-28040 Madrid,
Spain
⁹ Instituto de Astrofísica de Canarias, Via Lactea S/N,
E-38205, La Laguna, Tenerife, Spain
¹⁰ Departamento de Astrofísica, Universidad de La Laguna,
E-38206, La Laguna, Tenerife, Spain
¹¹ Jeremiah Horrocks Institute, University of Central
Lancashire, Preston PR1 2HE, UK
¹² Department of Space, Earth and Environment, Chalmers
University of Technology, Onsala Space Observatory, 43992
Onsala, Sweden
¹³ Instituto de Astrofísica de Andalucía (IAA, CSIC),
Glorieta de la Astronomía s/n, 18008-Granada, Spain
¹⁴ Netherlands Institute for Radio Astronomy, ASTRON,
Dwingeloo, The Netherlands
¹⁵ UK ALMA Regional Centre Node, Jodrell Bank Centre
for Astrophysics
¹⁶ AIM/CEA Paris-Saclay, Université de Paris, CNRS,
F-91191 Gif-sur-Yvette, France
¹⁷ Station de Radioastronomie de Nançay, Observatoire
de Paris, PSL Research University, CNRS, Univ. Orléans,
18330 Nançay, France
¹⁸ Department of Physics & Astronomy, University College
London, Gower Street, London WC1E 6BT, UK
¹⁹ Department of Astronomy, University of Wisconsin-
Madison, Madison, Wisconsin, USA
²⁰ Astrophysics Group, Cavendish Laboratory, 19
J. J. Thomson Avenue, Cambridge CB3 0HE, UK

- ²¹ Steward Observatory, University of Arizona, Tucson, AZ
85721-0065, USA
²² George P. and Cynthia W. Mitchell Institute for Fun-
damental Physics & Astronomy, Texas A&M University,
College Station, TX USA
²³ Max-Planck-Institut für Radioastronomie, Auf dem
Hügel 69, 53121 Bonn, Germany
²⁴ Department of Astrophysics/IMAPP, Radboud Univer-
sity, P.O. Box 9010, 6500 GL Nijmegen, The Netherlands
²⁵ Department of Physics, Box 41051, Science Building,
Texas Tech University, Lubbock, TX 79409-1051, US
²⁶ Department of Physics, University of Bath, Claverton
Down, Bath, BA2 7AY, UK
²⁷ International Gemini Observatory/NSF's NOIRLab, 670
N. A'ohoku Pl, Hilo, HI 96720 USA
²⁸ Institute of Astronomy and Astrophysics, Academia
Sinica, 11F of Astronomy-Mathematics Building, AS/NTU
No. 1, Sec. 4, Roosevelt Rd, Taipei 10617, Taiwan, R.O.C
²⁹ Center for Astro, Particle and Planetary Physics, New
York University Abu Dhabi, PO Box 129188, Abu Dhabi,
UAE
³⁰ School of Physics and Astronomy, University of Birming-
ham, Edgbaston, Birmingham B15 2TT, UK
³¹ Centre for Extragalactic Astronomy, Department of
Physics, Durham University, Durham DH1 3LE.

APPENDIX A: RADIO DATA

In the Appendix A we present the radio images of the 78 de-
tected Palomar galaxies (out of 177) studied here: Fig. A1 for
the 66 galaxies where we identified the core and Fig. A2 for
the 15 galaxies without a core identification. Table A2 and
Table A3 list the source parameters of the radio components
detected in the images for the identified and unidentified
sources, respectively. Table A4 provides the radio contours
and the properties of the restoring beams of the radio maps
of all the detected galaxies.

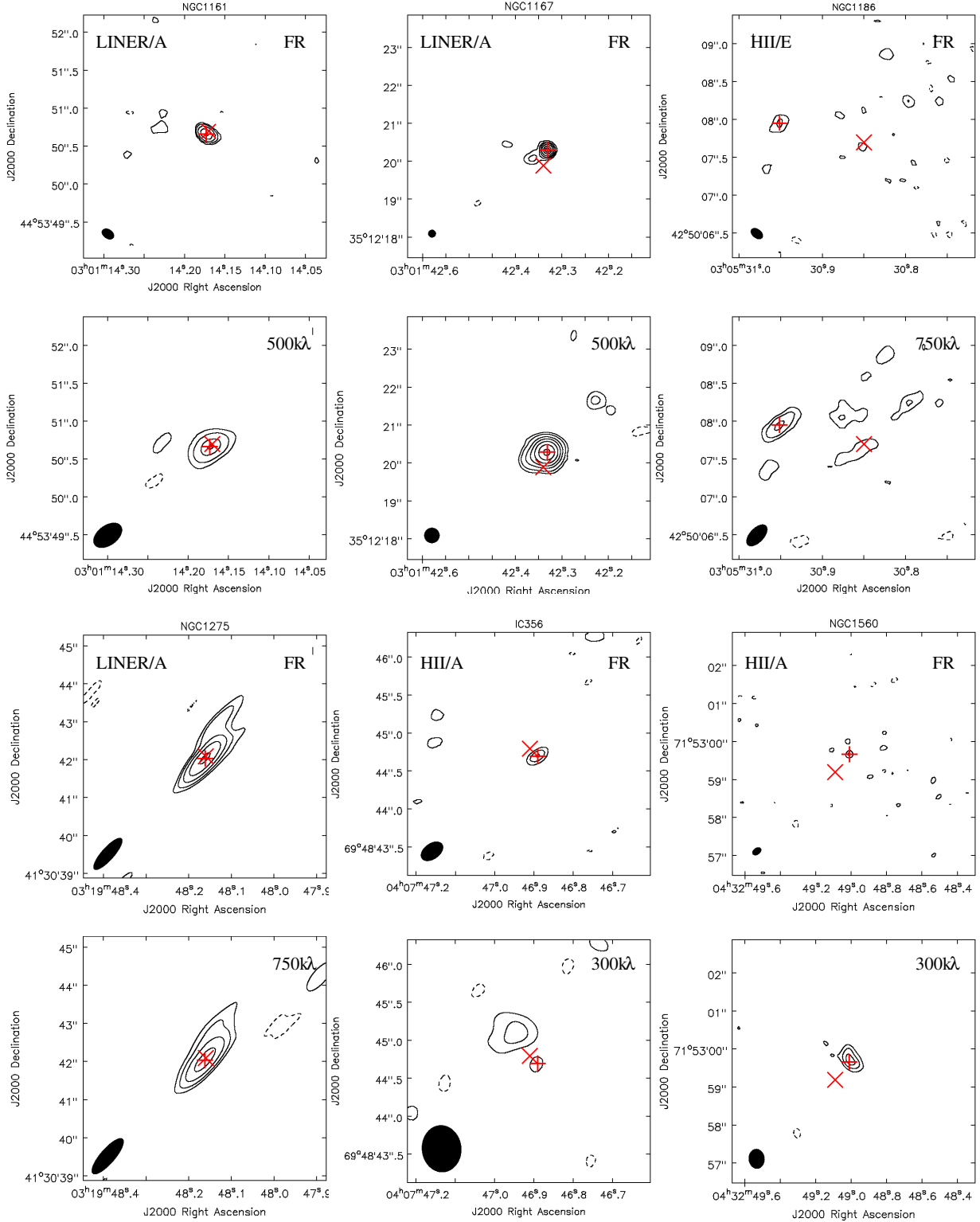


Figure A1. e-MERLIN 1.5-GHz radio maps of the detected and core-identified galaxies. For each galaxy two panels are shown. The upper panel depicts the full-resolution map, while the lower panel shows the low-resolution map obtained with a uv -tapered scale written in the panel (in kλ), all on a same physical scale. For four galaxies (NGC 3516, NGC 4036, NGC 5322, and NGC 5548) a third radio map is presented corresponding to a lower resolution map (see the scale and map parameters in Tab A4). The restoring beam is presented as a filled ellipse at one of the corners of each of the maps. The contour levels of the maps are presented in Table A4. The \times marks indicate the optical galaxy centre taken from NED, while the $+$ symbol marks the radio core position, if identified. In the upper panels, the optical (LINER, Seyfert, HII, and ALG) and radio (A, B, C, D, E, see Section 4.2 for description) classifications of the sources are reported. The full sets of Figures are available online.

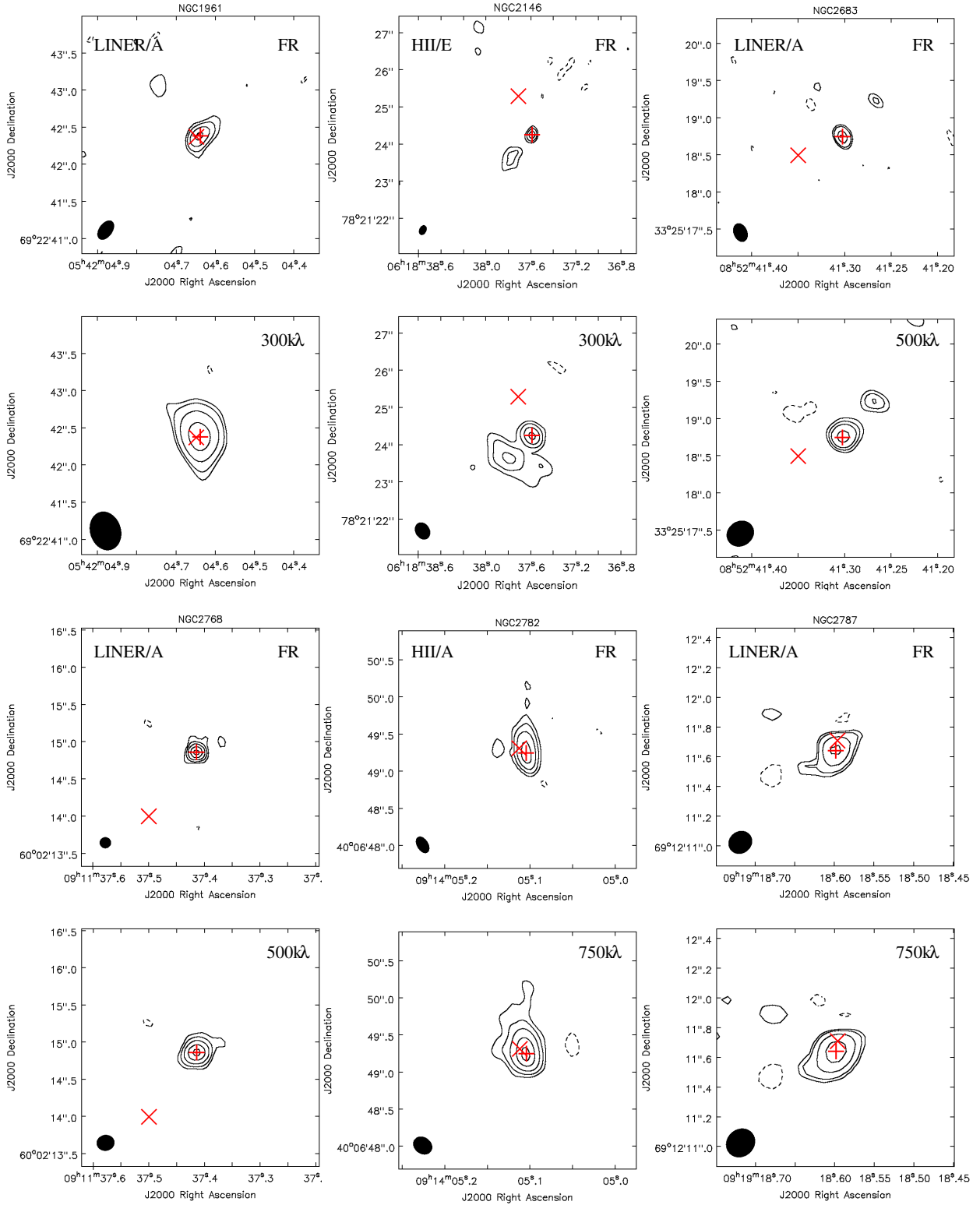


Figure A1. e-MERLIN 1.5-GHz maps of the detected and core-identified galaxies. See first page of this figure for details.

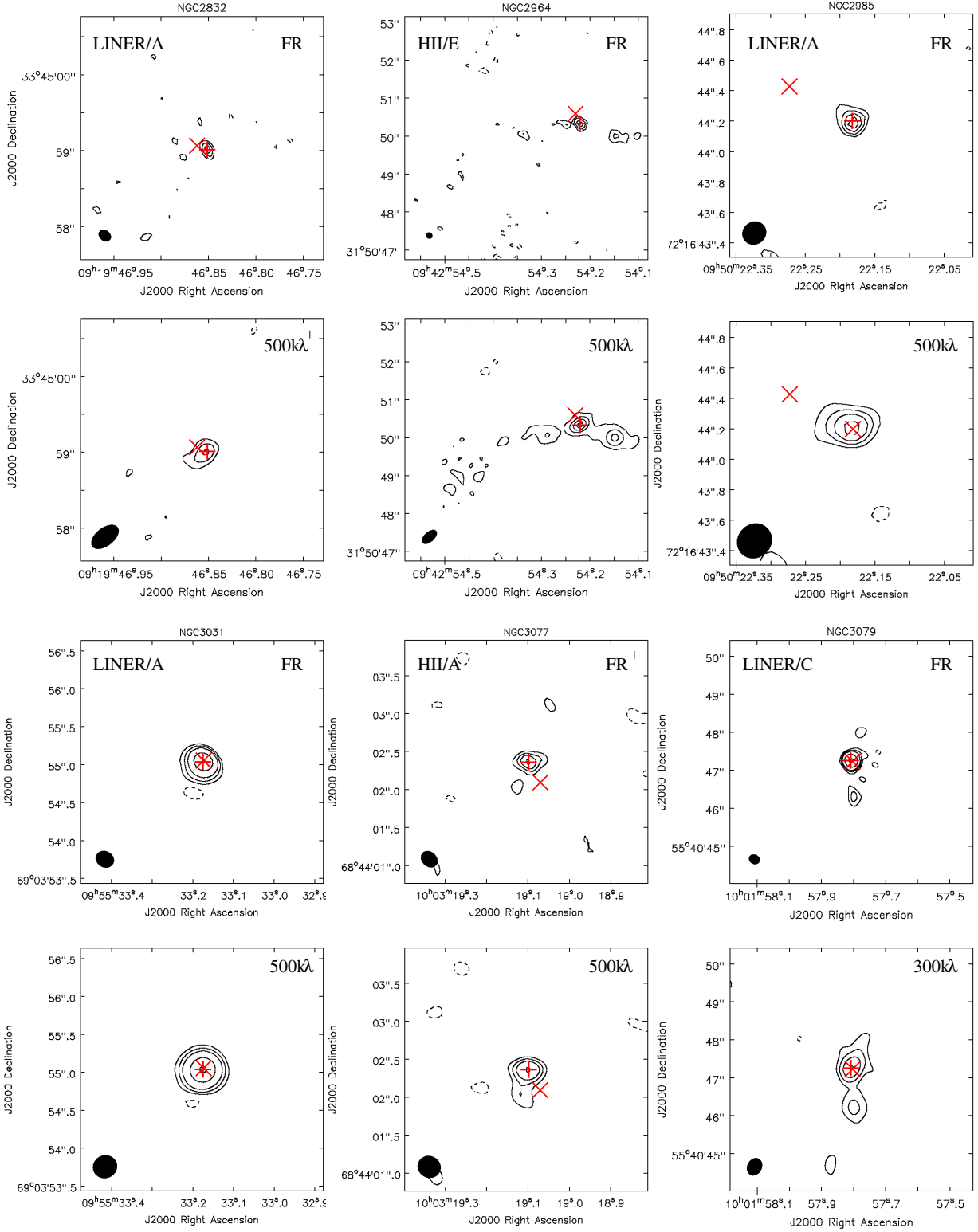


Figure A1. e-MERLIN 1.5-GHz maps of the detected and core-identified galaxies. See first page of this figure for details.

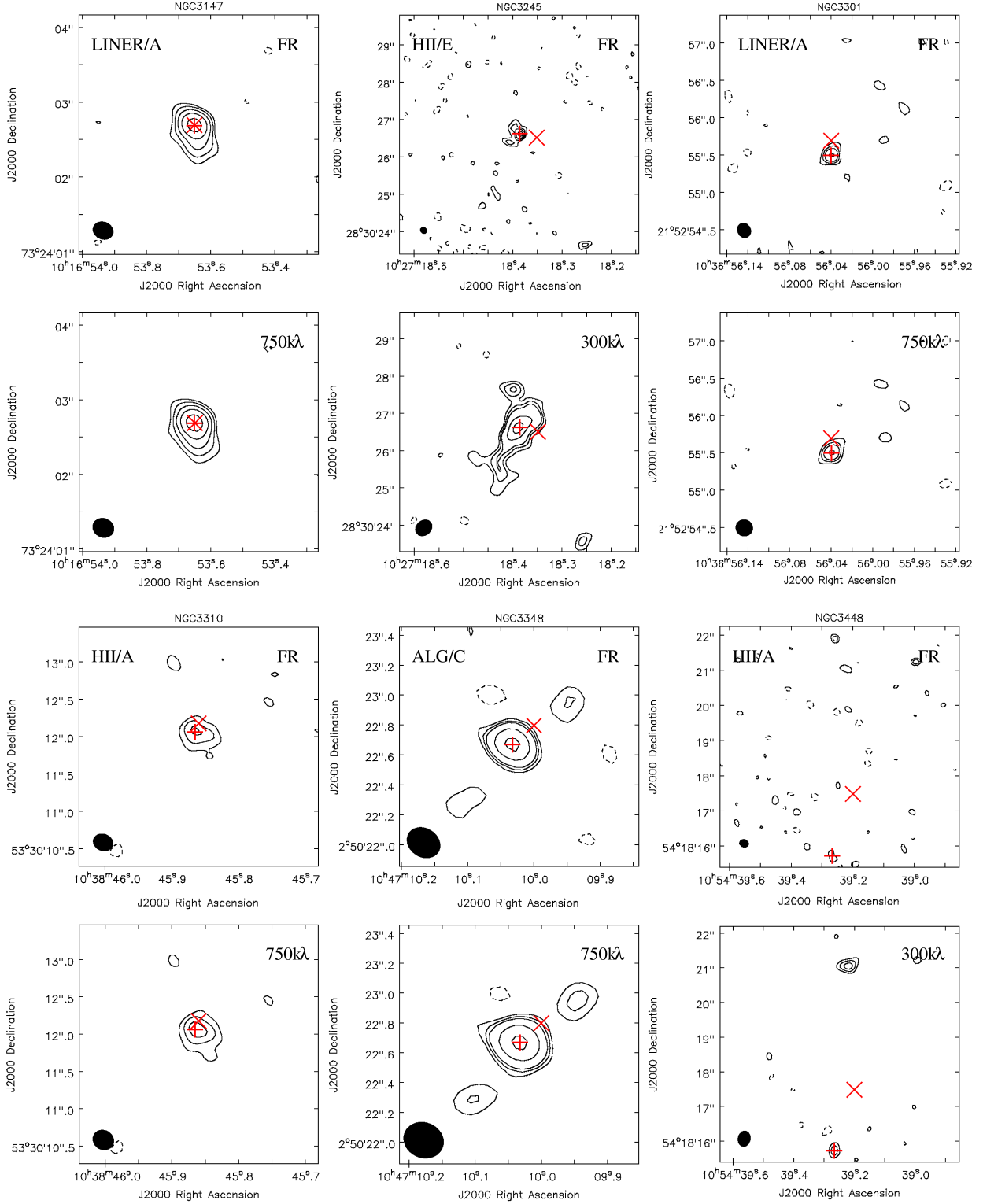


Figure A1. e-MERLIN 1.5-GHz maps of the detected and core-identified galaxies. See first page of this figure for details.

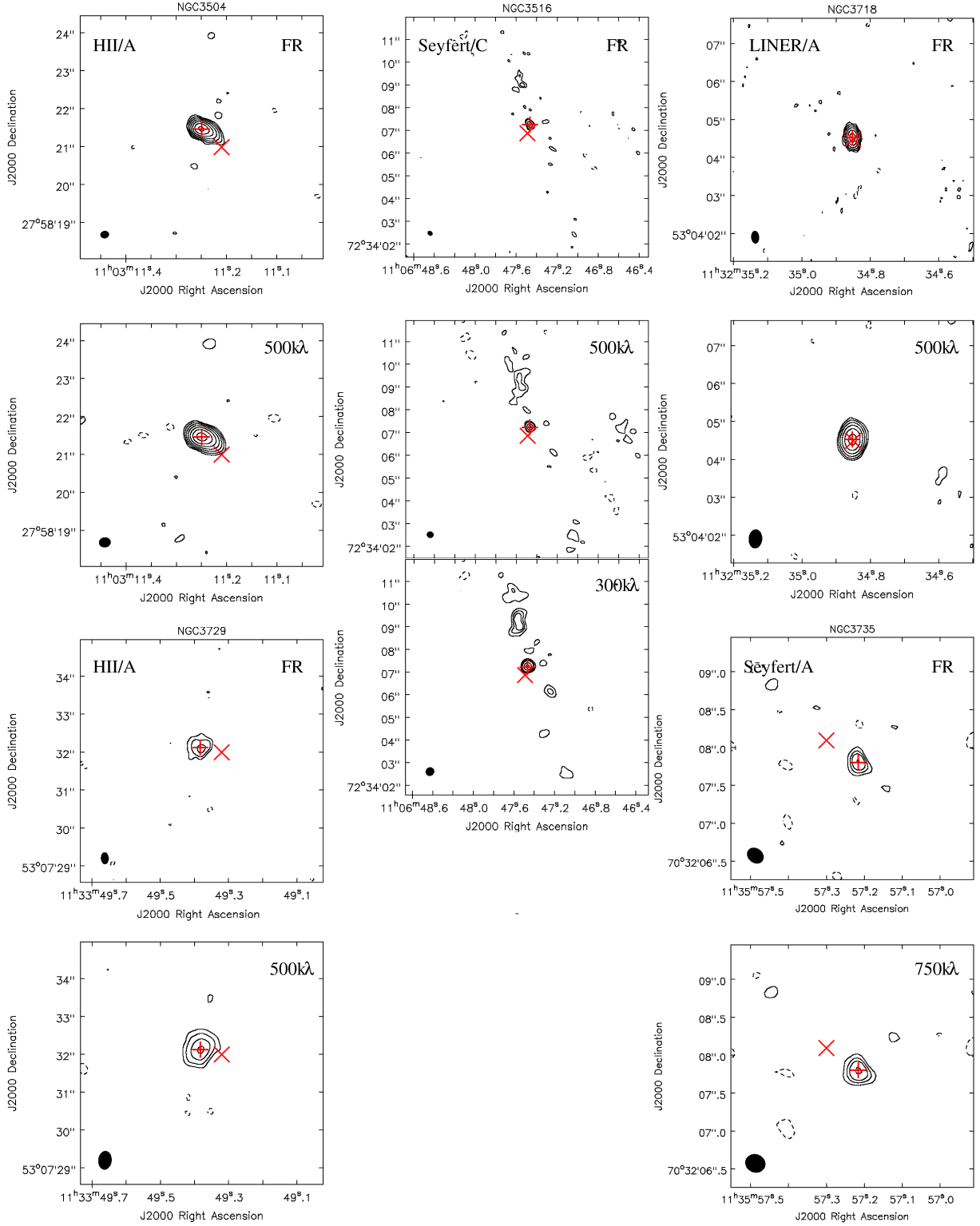


Figure A1. e-MERLIN 1.5-GHz maps of the detected and identified galaxies. See first page of this figure for details.

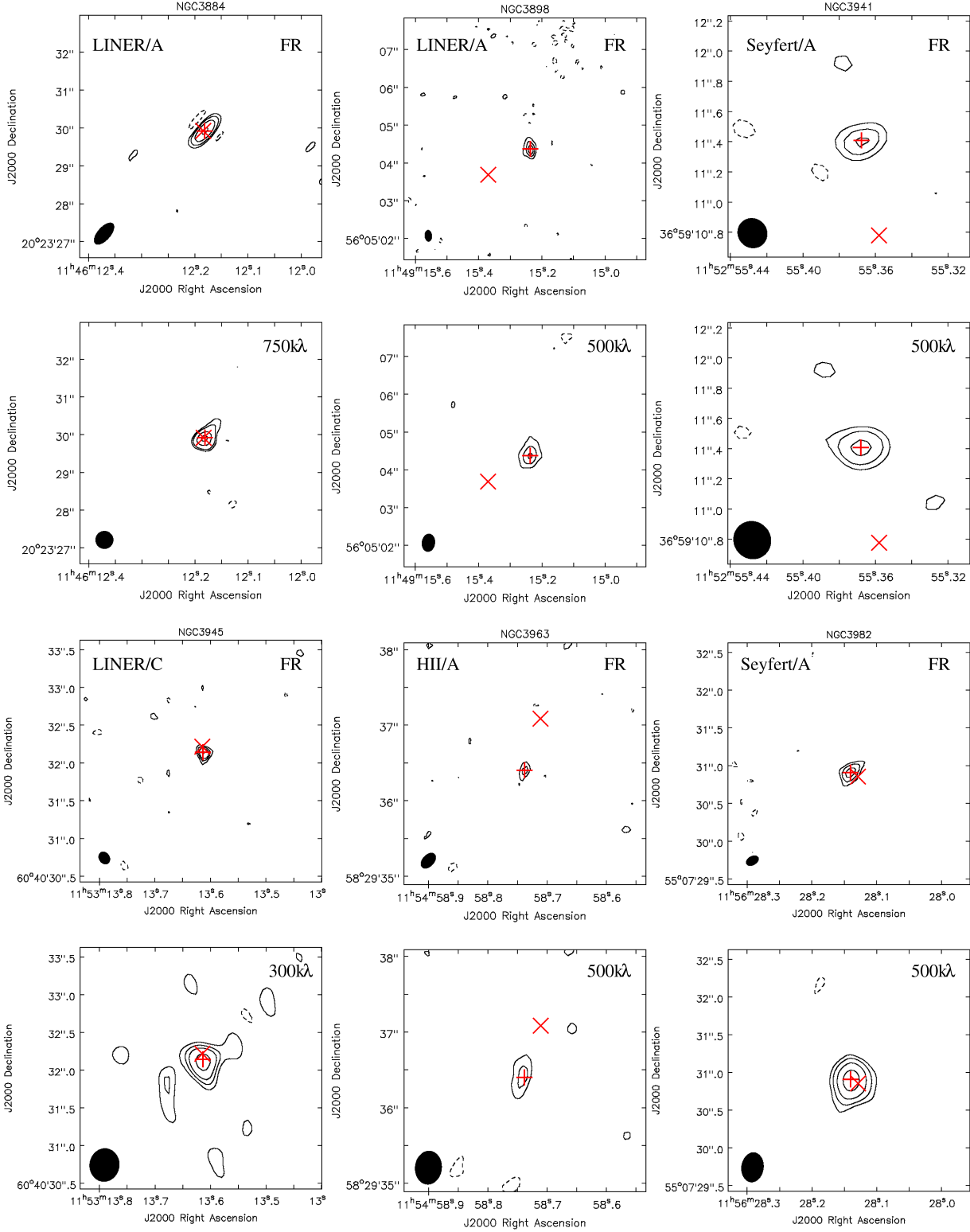


Figure A1. e-MERLIN 1.5-GHz maps of the detected and core-identified galaxies. See first page of this figure for details.

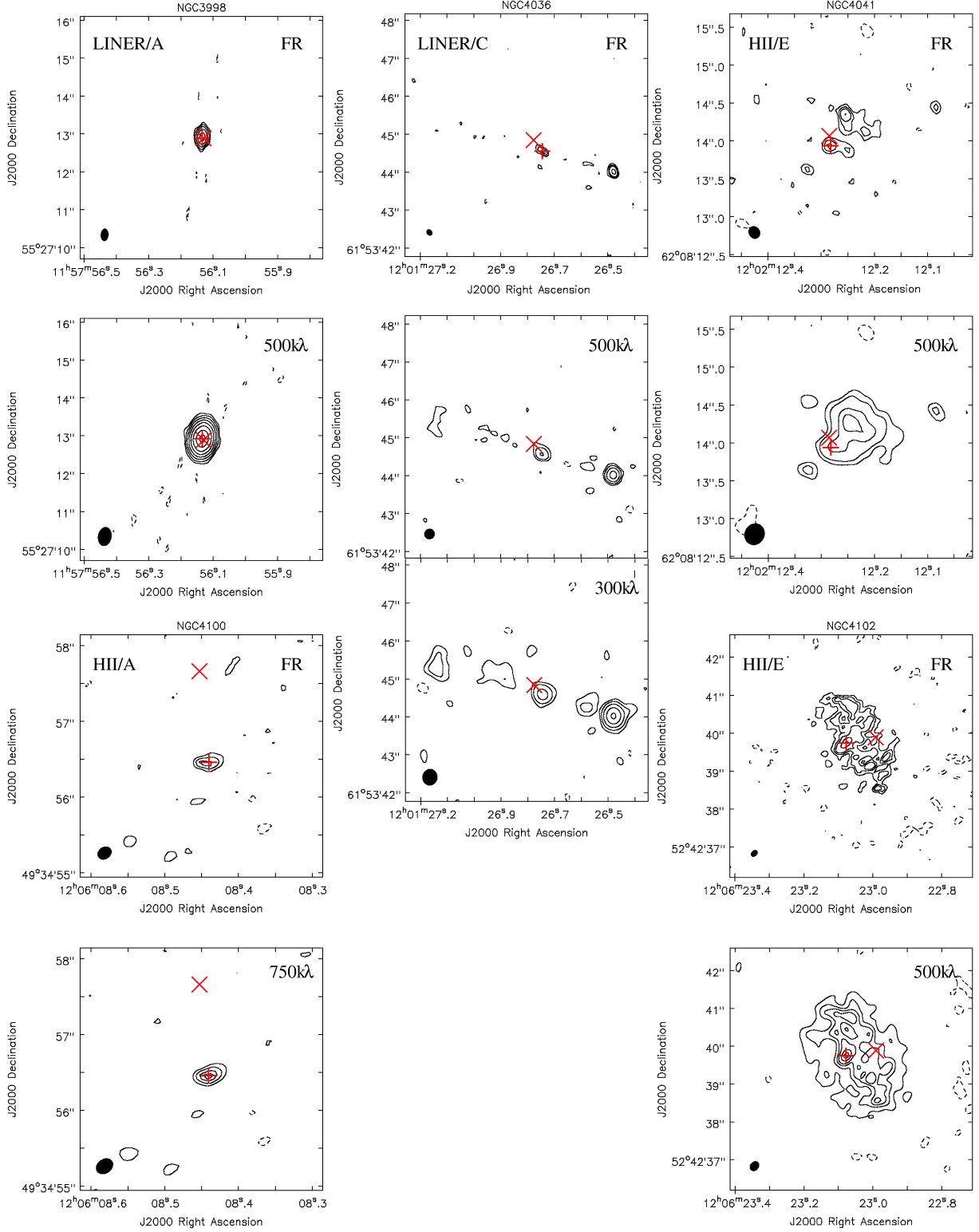


Figure A1. e-MERLIN 1.5-GHz maps of the detected and core-identified galaxies. See first page of this figure for details.

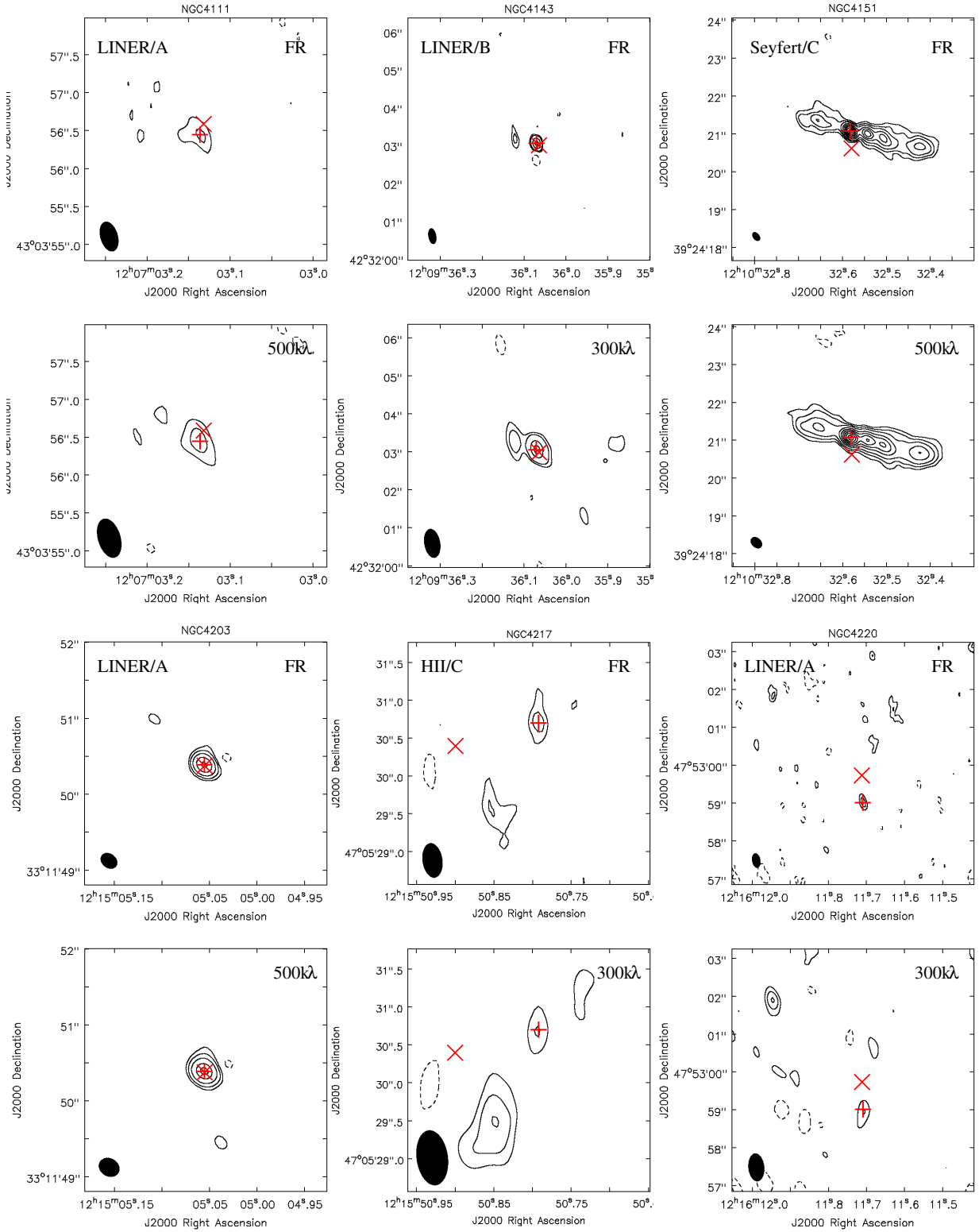


Figure A1. e-MERLIN 1.5-GHz maps of the detected and core-identified galaxies. See first page of this figure for details.

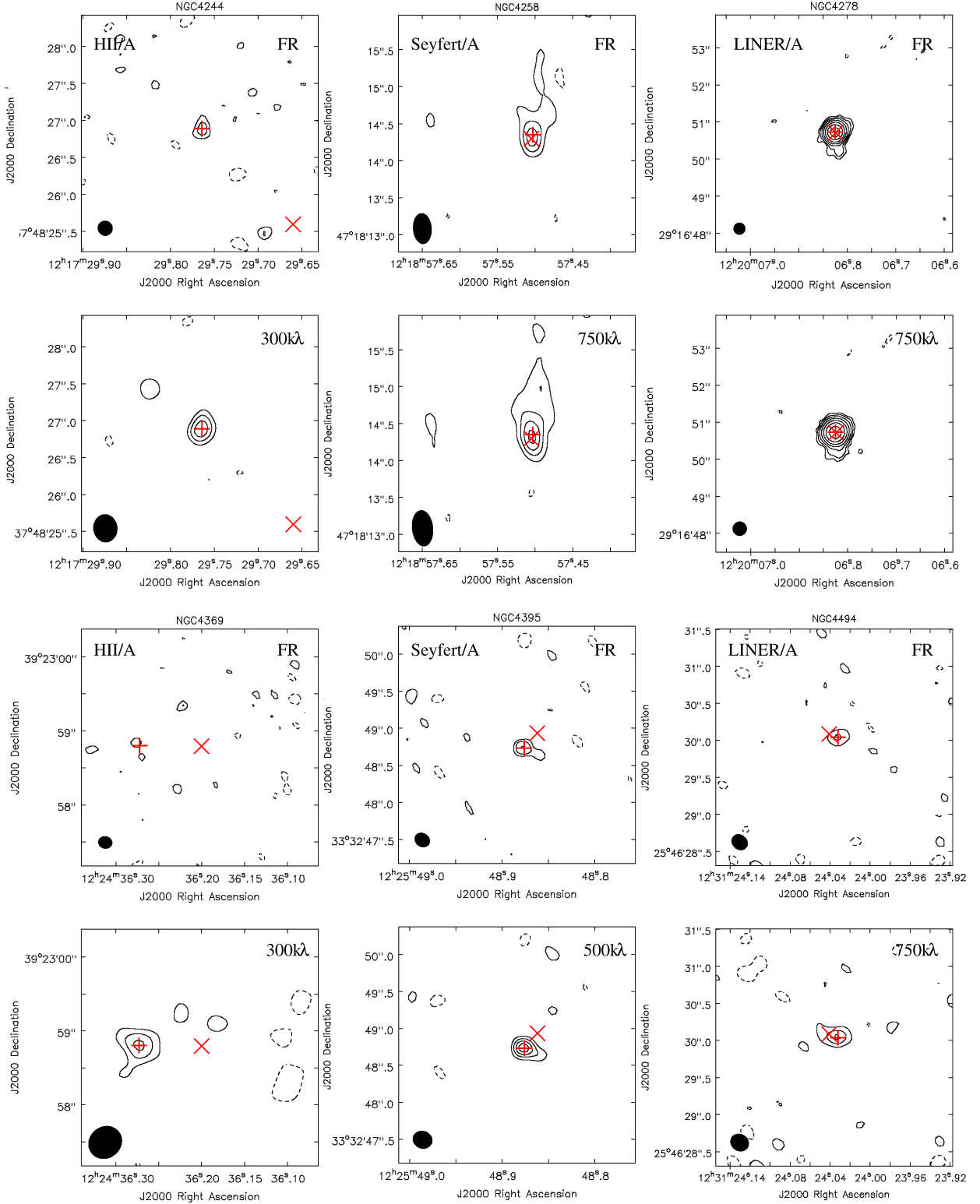


Figure A1. e-MERLIN 1.5-GHz maps of the detected and core-identified galaxies. See first page of this figure for details.

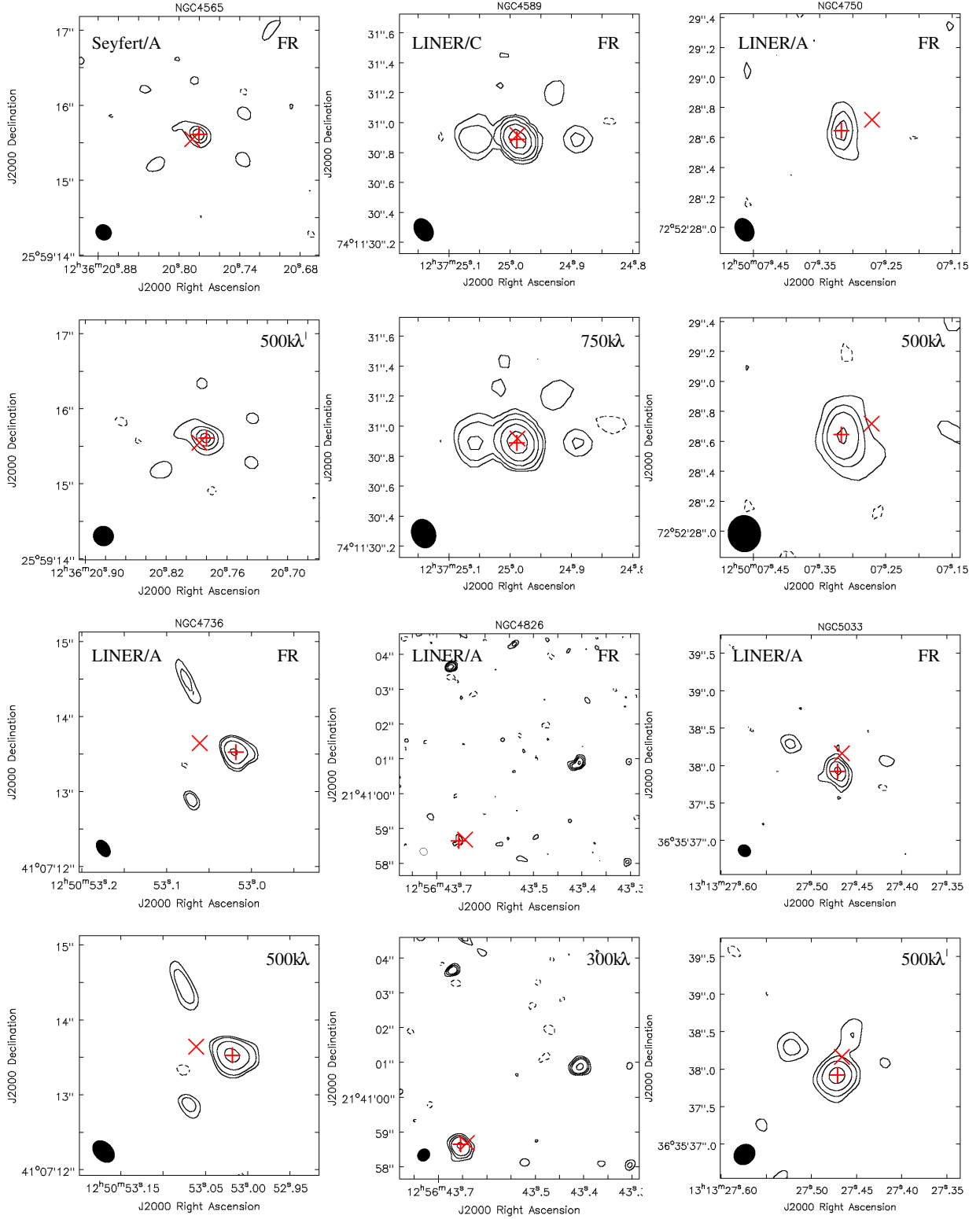


Figure A1. e-MERLIN 1.5-GHz maps of the detected and core-identified galaxies. See first page of this figure for details.

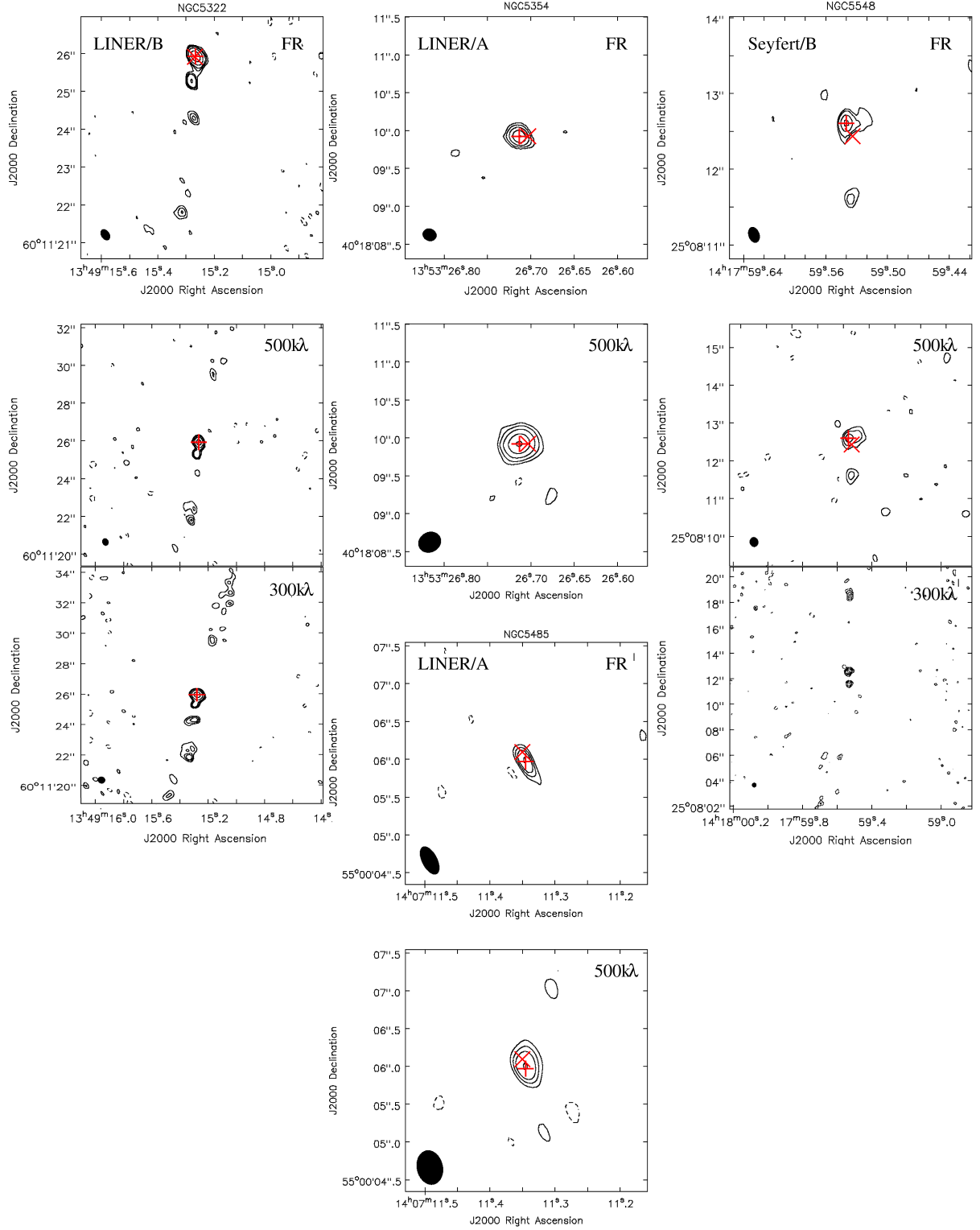


Figure A1. e-MERLIN 1.5-GHz maps of the detected and core-identified galaxies. See first page of this figure for details.

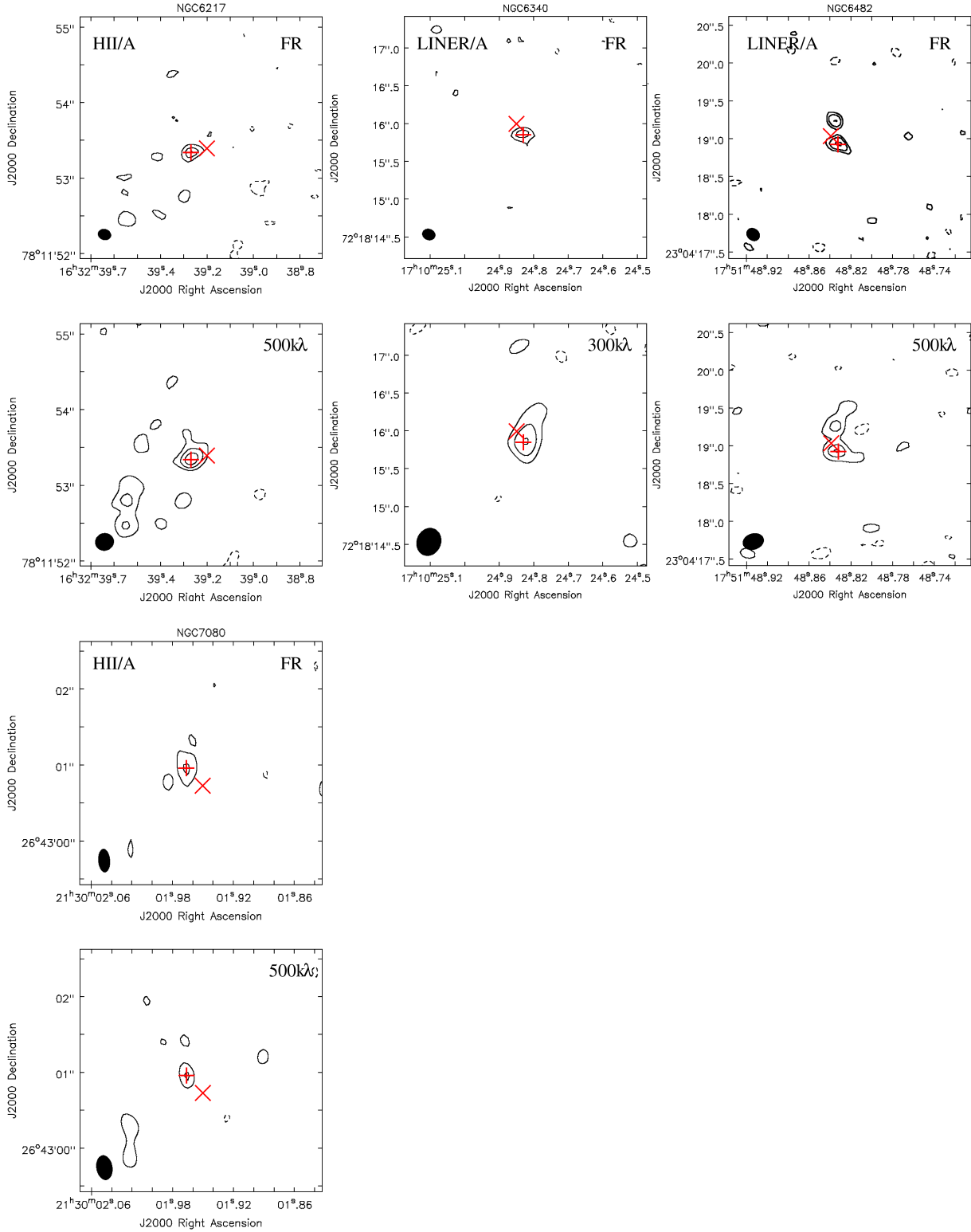


Figure A1. e-MERLIN 1.5-GHz maps of the detected and core-identified galaxies. See first page of this figure for details.

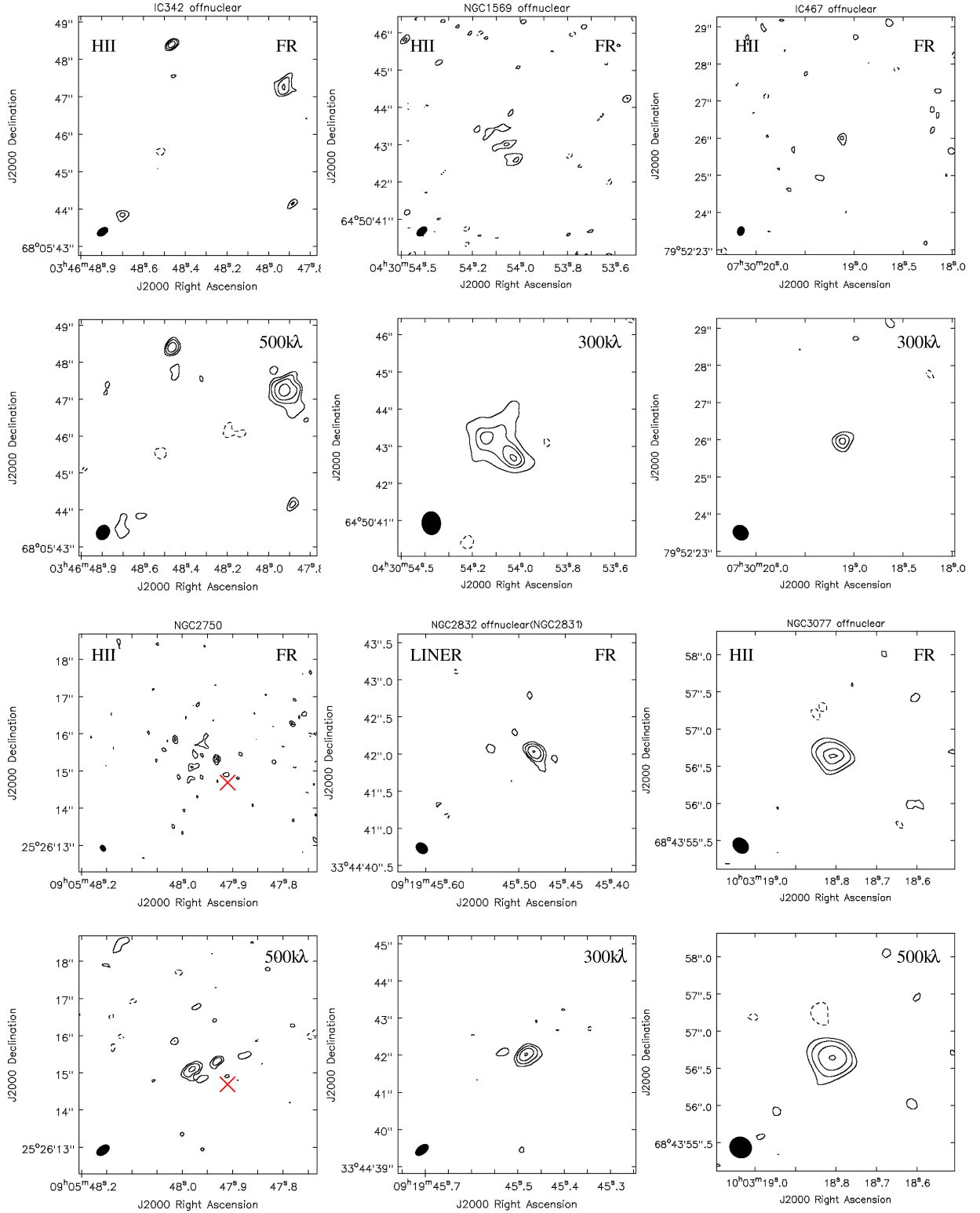


Figure A2. *e*-MERLIN 1.5-GHz radio images of the galaxies, which are detected but no radio core is identified. For each galaxy two panels are shown. The upper panel shows the full-resolution map, while the lower panel shows the low-resolution map obtained with a uv-tapered scale written in the panel (in kλ). The maps for the each source are generally on the same physical scale. The restoring beam is presented as a filled ellipse at one of the corners of each of the maps. The contour levels of the maps are presented in Table A4. The × marks indicate the optical galaxy centre taken from NED, while the + symbol marks the radio core position, if identified. In the upper panels, the optical (LINER, Seyfert, HII, and ALG) and radio (A, B, C, D, E, see Section 4.2 for description) classifications of the sources are reported.

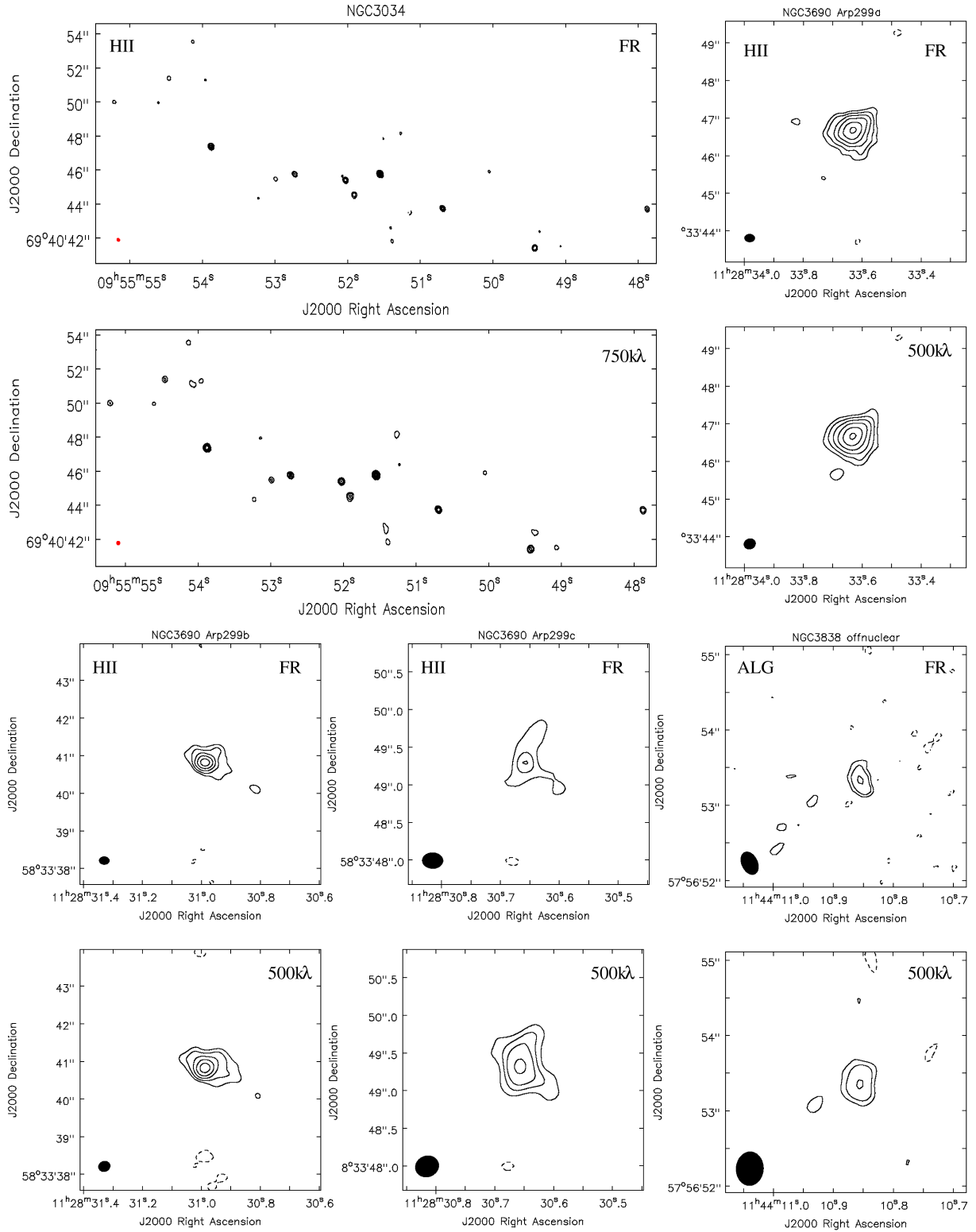


Figure A2. e-MERLIN 1.5-GHz images of the unidentified galaxies. See last page of this figure for detail.

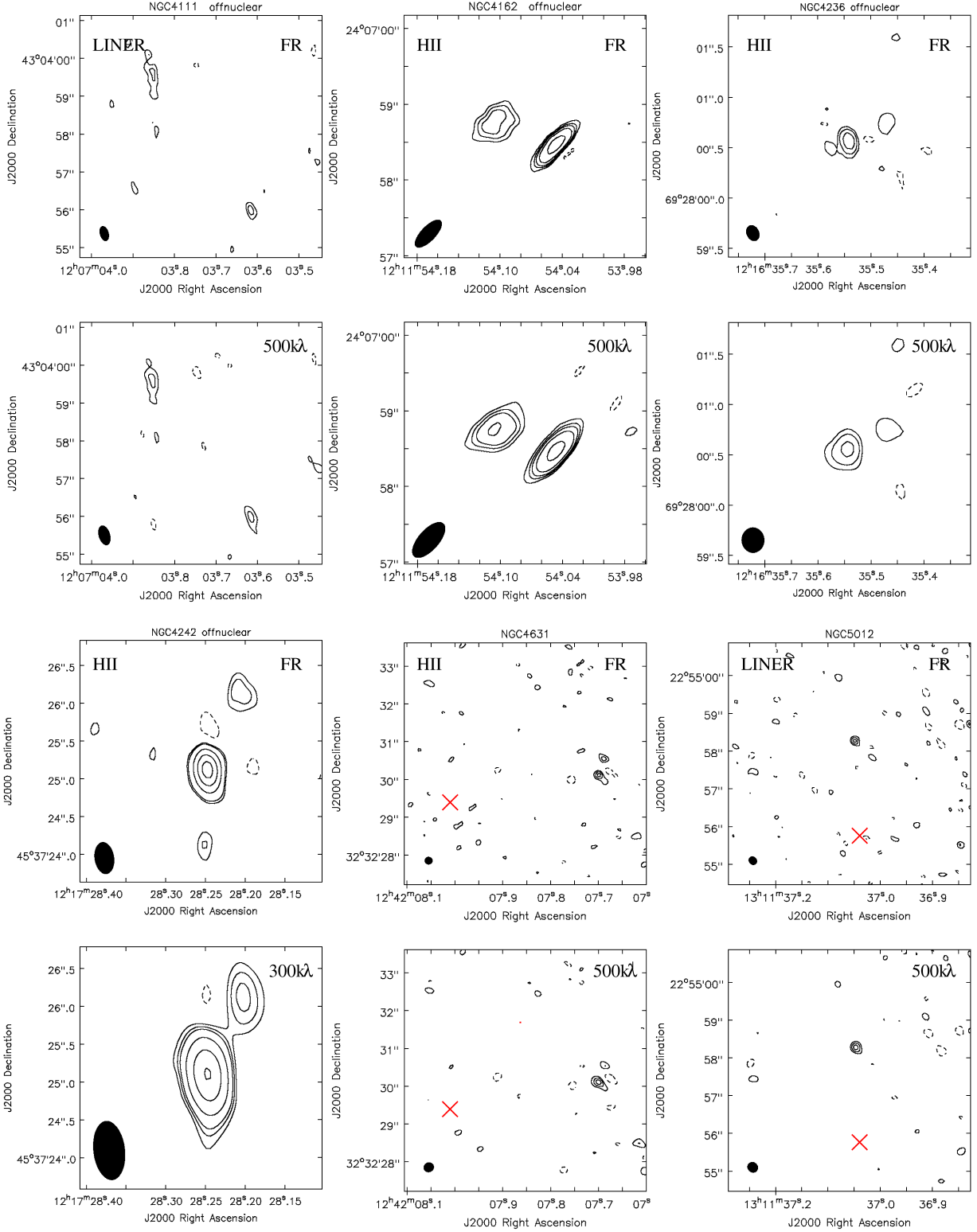


Figure A2. e-MERLIN 1.5-GHz images of the unidentified galaxies. See last page of this figure for detail.

Table A1: Optical and radio properties of the sample.

Name (1)	RA (2)	DEC (3)	D (4) Mpc	Hubble (5) type	class (6) Ho97	class (7) BPT	LEM (8)	Q (9)	Beam (10) arcsec ²	PA (11) degree	rms (12) $\mu\text{Jy/b}$	det (13)	morph (14)	log L_{core} (15) erg s ⁻¹	log L_{tot} (16) erg s ⁻¹
NGC 783	02 01 06.61	+31 52 56.8	68.1	SAC	H	H	MISC1	+	0.22×0.12	34.5	53	U	—	<36.12	—
IC 239	02 36 27.82	+38 58 09.1	16.8	SAB(rs)cd	L2::	H ^a	TEST	++	0.19×0.12	40.0	63	U	—	<34.98	—
NGC 1003	02 39 17.03	+40 52 21.3	10.7	SA(s)cd	ALG	H ^{b,c}	TEST	++	0.19×0.12	46.5	62	U	—	<34.58	—
NGC 1023	02 40 24.01	+39 03 47.7	10.5	SB(rs)0-	ALG	ALG ^b	TEST	++	0.19×0.12	42.7	63	U	—	<34.57	—
NGC 1058	02 43 30.01	+37 20 28.7	9.1	SA(rs)c	S2	L	TEST	++	0.21×0.12	41.0	57	U	—	<34.41	—
NGC 1156	02 59 42.85	+25 14 28.4	6.4	IB(s)m	H	H	TEST	++	0.22×0.12	33.5	64	U	—	<34.15	—
NGC 1161	03 01 14.17	+44 53 50.7	25.9	SA0	T1.9:	L	TEST	++	0.18×0.12	55.8	67	I	A	36.57	36.69
NGC 1167	03 01 42.34	+35 12 19.9	65.3	SA0-	S2	L	TEST	++	0.20×0.20	0	2700	I	A	39.65	39.76
NGC 1169	03 03 34.76	+46 23 10.7	33.7	SAB(r)b	L2	L ^d	TEST	++	0.20×0.11	48.3	75	U	—	<35.66	—
NGC 1186	03 05 30.85	+42 50 07.7	35.4	SB(r)bc:	H	H	TEST	++	0.18×0.12	52.3	65	I	E	35.91	36.78
NGC 1275	03 19 48.16	+41 30 42.1	70.1	Pec cD	S1.5	L ^e	TEST	++	1.00×0.33	-41.6	156000	I	A	40.97	41.62
IC 342	03 46 48.51	+68 05 46.0	3.0	SAB(rs)cd	H	H	26	+	0.33×0.20	-57.3	150	unI	—	<33.86	—
IC 356	04 07 46.88	+69 48 44.7	18.1	SA(s)ab pec	T2	H ^b	26	+	0.33×0.20	-54.5	113	I	A	35.52	35.74
NGC 1569	04 30 49.19	+64 50 52.5	1.6	IBm	H	H	26	+	0.33×0.20	-50.1	110	unI	—	<33.18	—
NGC 1560	04 32 49.09	+71 52 59.2	3.0	SA(s)d spin	H	H	26	+	0.26×0.17	-53.7	95	I	A	33.78	34.12
NGC 1961	05 42 04.61	+69 22 42.3	53.1	SAB(rs)c	L2	L ^f	26	+	0.29×0.18	-35.8	126	I	A	37.15	37.25
NGC 2146	06 18 37.71	+78 21 25.3	17.2	SB(s)ab pec	H	H	26	+	0.27×0.18	-23.7	134	I	E	36.34	36.86
UGC 3714	07 12 32.68	+71 45 01.9	40.9	S? pec	H	H	26	+	0.30×0.19	-17.9	89	U	—	<35.90	—
NGC 2336	07 27 03.66	+80 10 42.0	33.9	SAB(r)bc	L2/S2	L	26	+	0.27×0.20	-11.7	90	U	—	<35.75	—
NGC 2366	07 28 51.85	+69 12 31.1	2.9	IB(s)m	ALG	H ^{f,g}	26	+	0.32×0.19	-11.8	96	U	—	<33.64	—
IC 467	07 30 18.40	+79 52 21.1	27.4	SAB(s)c:	H:	H	26	+	0.26×0.19	-15.7	90	unI	—	<35.56	—
NGC 2403	07 36 51.40	+65 36 09.2	4.2	SAB(s)cd	H	H:	24	+	0.15×0.15	84.9	97	U	—	<33.96	—
NGC 2549	08 18 58.35	+57 48 10.9	18.8	SA(r)0 spin	ALG	ALG ^f	24	+	0.16×0.15	-85.9	95	U	—	<35.26	—
NGC 2683	08 52 41.35	+33 25 18.5	5.7	SA(rs)b	L2/S2	L	MISC2	+	0.26×0.18	22.8	48	I	A	34.49	34.65
NGC 2685	08 55 34.75	+58 44 03.9	16.2	(R)SB0+pec	S2/T2:	L	MISC2	+	0.19×0.14	36.4	47	U	—	<34.82	—
NGC 2750	09 05 47.89	+25 26 14.5	38.4	SABc	H	H	28	+	0.19×0.14	33.0	72	unI	—	<35.76	—
NGC 2742	09 07 33.58	+60 28 45.8	22.2	SA(s)c:	H	H	24	+	0.15×0.15	-55.9	88	U	—	<35.37	—
NGC 2770	09 09 33.62	+33 07 24.3	29.6	SA(s)c:	H	H	28	+	0.18×0.13	46.8	61	U	—	<35.46	—
NGC 2768	09 11 37.50	+60 02 14.8	23.7	E6:	L2	L ^g	24	+	0.15×0.15	88.6	122	I	A	37.10	37.19
NGC 2776	09 12 14.53	+44 57 17.6	38.7	SAB(rs)c	H	H	MISC2	+	0.21×0.13	32.9	51	U	—	<35.61	—
NGC 2782	09 14 05.12	+40 06 49.1	37.3	SAB(rs)a pec	H	H	MISC2	+	0.24×0.15	31.5	51	I	A	36.79	37.16
NGC 2787	09 19 18.54	+69 12 11.6	13.0	SB(r)0+	L1.9	L	24	+	0.16×0.15	-53.8	141	I	A	36.28	36.41
NGC 2832	09 19 46.88	+33 44 59.4	91.6	E+2:	L2::	L ^b	28	+	0.18×0.14	50.3	70	I+unI	A	36.83	37.05
NGC 2859	09 24 18.53	+34 30 47.5	25.4	(R)SB(r)0+	T2:	L	28	+	0.17×0.14	53.2	59	U	—	<35.31	—
NGC 2903	09 32 10.11	+21 30 03.0	6.3	SAB(rs)bc	H	H	28	+	0.19×0.13	30.7	97	U	—	<34.32	—
NGC 2950	09 42 35.12	+58 51 04.4	23.3	(R)SB(r)0	ALG	ALG	24	+	0.15×0.14	53.5	100	U	—	<35.47	—
NGC 2964	09 42 54.23	+31 50 50.2	21.9	SAB(r)bc:	H	H	28	+	0.17×0.16	57.5	90	I	E	36.03	36.97
NGC 2977	09 43 46.80	+74 51 34.9	40.9	SAb:	H	H	24	+	0.16×0.15	-58.3	91	U	—	<35.91	—
NGC 2976	09 47 15.46	+67 54 59.0	2.1	SAC pec	H	H	23	++	0.24×0.19	48.5	74	U	—	<33.24	—

Continued on Next Page

Table A1 – Continued

Name (1)	RA (2)	DEC (3)	D (4) Mpc	Hubble (5) type	class (6) Ho97	class (7) BPT	LEM (8)	Q (9)	Beam (10) arcsec ²	PA (11) degree	rms (12) $\mu\text{Jy/b}$	det (13)	morph (14)	log L _{core} (15) erg s ⁻¹	log L _{tot} (16) erg s ⁻¹
NGC 3003	09 48 36.05	+33 25 17.4	24.4	SABc?	H	H	28	+	0.17×0.16	82.6	59	U	—	<35.28	—
NGC 2985	09 50 22.23	+72 16 4.0	22.4	R')SA(rs)ab	T1.9	L ^h	24	+	0.16×0.15	-54.9	91	I	A	35.81	36.03
NGC 3031	09 55 33.17	+69 03 55.1	1.4	SA(s)ab	S1.5	L ^{f,g,h}	23	++	0.25×0.21	61.5	178	I	A	35.50	35.54
NGC 3027	09 55 40.63	+72 12 12.8	19.5	SB(rs)d:	H	H	24	+	0.16×0.15	-52.1	95	U	—	<35.29	—
NGC 3034	09 55 52.43	+69 40 46.9	5.2	IA0 spin	H	H	23	++	0.24×0.20	60.1	131	unI	—	<34.28	—
NGC 3043	09 56 14.85	+59 18 25.6	39.1	SAb: spin	H	H	24	+	0.15×0.14	72.4	99	U	—	<35.91	—
NGC 3073	10 00 52.20	+55 37 07.9	19.3	SAB0-	H	H ⁱ	22	+	0.29×0.25	66.6	91	U	—	<35.26	—
NGC 3077	10 03 19.10	+68 44 1.6	2.1	I0 pec	H	H	23	++	0.24×0.19	46.6	88	I+unI	A	33.32	34.35
NGC 3079	10 01 57.80	+55 40 47.2	20.4	SB(s)c spin	S2	L ⁱ	22	+	0.30×0.25	64.7	257	I	C	37.27	37.75
NGC 3162	10 13 31.59	+22 44 15.2	22.2	SAB(rs)bc	H	H	16	++	0.20×0.19	-64.6	58	U	—	<35.19	—
NGC 3147	10 16 53.62	+73 24 02.3	40.9	SA(rs)bc	S2	L	23	++	0.23×0.19	51.9	99	I	A	37.36	37.51
NGC 3185	10 17 38.56	+21 41 17.8	21.3	(R)SB(r)0/a	S2:	S	16	++	0.20×0.20	-60.5	58	U	—	<35.15	—
NGC 3190	10 18 05.63	+21 49 55.6	22.4	SA(s)a pec spin	L2	L	16	++	0.20×0.20	-81.0	77	U	—	<35.32	—
NGC 3193	10 18 24.88	+21 53 38.3	23.2	E2	L2:	L	16	++	0.21×0.20	-84.5	59	U	—	<35.23	—
NGC 3245	10 27 18.39	+28 30 26.8	22.2	SA(r)0?	T2:	H ⁱ	16	++	0.19×0.17	39.1	70	I	E	35.71	36.36
IC 2574	10 28 23.62	+68 24 43.4	3.4	SAB(s)m	H	H	23	++	0.24×0.19	46.3	74	U	—	<33.66	—
NGC 3254	10 29 19.92	+29 29 39.2	23.6	SA(s)bc	S2	S	16	++	0.19×0.17	42.4	62	U	—	<35.27	—
NGC 3301	10 36 56.03	+21 52 55.8	23.3	(R')SB(rs)0/a	L2	L ^j	16	++	0.21×0.18	26.8	74	I	A	35.70	35.86
NGC 3310	10 38 45.86	+53 30 11.9	18.7	SAB(r)bc pec	H	H	22	+	0.27×0.23	69.4	101	I	A	35.60	36.20
NGC 3344	10 43 31.15	+24 55 20.0	6.1	(R)SAB(r)bc	H	H	16	++	0.20×0.17	32.1	64	U	—	<34.11	—
NGC 3359	10 46 36.86	+63 13 27.3	19.2	SB(rs)c	H	H	23	++	0.25×0.20	40.6	81	U	—	<35.21	—
NGC 3348	10 47 10.00	+72 50 22.8	37.8	E0	ALG	ALG	23	++	0.23×0.19	56.7	78	I	C	36.59	36.73
NGC 3395	10 49 50.11	+32 58 58.3	27.4	SAB(rs)cd: pec	H	H	MISC2	+	0.24×0.15	37.3	52	U	—	<35.32	—
NGC 3448	10 54 39.20	+54 18 17.5	24.5	IA0	H	H	22	+	0.27×0.22	71.5	86	I	A	35.55	36.35
NGC 3486	11 00 23.87	+28 58 30.5	7.4	SAB(r)c	S2	S	16	++	0.19×0.17	41.0	62	U	—	<34.26	—
NGC 3504	11 03 11.21	+27 58 21.0	26.5	(R)SAB(s)ab	H	H	16	++	0.22×0.19	-77.4	57	I	A	37.30	37.65
NGC 3516	11 06 47.49	+72 34 06.9	38.9	(R)SB(s)0:	S1.2	S	23	++	0.23×0.19	50.9	97	I	C	36.84	36.95
NGC 3556	11 11 30.97	+55 40 26.8	14.1	SB(s)cd spin	H	H	22	+	0.26×0.23	73.1	78	U	—	<34.92	—
NGC 3610	11 18 25.27	+58 47 10.6	29.2	E5:	ALG	ALG	22	+	0.26×0.22	82.7	79	U	—	<35.56	—
NGC 3613	11 18 36.11	+58 00 00.0	32.9	E6	ALG	ALG	22	+	0.26×0.22	80.9	84	U	—	<35.69	—
NGC 3631	11 21 02.87	+53 10 10.5	21.6	SA(s)c	H	H	19	++	0.19×0.15	-45.2	67	U	—	<35.23	—
NGC 3646	11 21 43.08	+20 10 10.4	56.8	SA:(r)bc pec ring	H/T2:	L	12	m	0.62×0.24	-39.2	55	U	—	<35.98	—
NGC 3642	11 22 17.89	+59 04 28.3	27.5	SA(r)bc:	L1.9	L ^h	22	+	0.27×0.22	79.9	87	U	—	<35.55	—
NGC 3690	11 28 32.30	+58 33 43.0	40.4	IBm pec	H	H	22	+	0.28×0.21	88.2	184	unI	—	<36.21	—
UGC 6484	11 29 11.76	+57 07 55.4	32.4	SB(rs)c	H	H	22	+	0.26×0.23	78.4	82	U	—	<35.67	—
NGC 3718	11 32 34.85	+53 04 04.5	17.0	SB(s)a pec	L1.9	L ^k	20	+	0.33×0.20	4.1	86	I	A	36.78	36.78
NGC 3729	11 33 49.32	+53 07 32.0	17.0	SB(r)a pec	H	H	20	+	0.31×0.20	2.6	86	I	A	35.85	36.34
NGC 3738	11 35 48.79	+54 31 26.0	4.3	IAm	H	H	20	+	0.31×0.19	2.8	78	U	—	<33.89	—
NGC 3735	11 35 57.30	+70 32 08.1	41.0	SAc: spin	S2:	S	23	++	0.23×0.19	52.4	79	I	A	36.24	36.50

Continued on Next Page

Table A1 – Continued

Name (1)	RA (2)	DEC (3)	D (4) Mpc	Hubble (5) type	class (6) Ho97	class (7) BPT	LEM (8)	Q (9)	Beam (10) arcsec ²	PA (11) degree	rms (12) μ Jy/b	det (13)	morph (14)	log L _{core} (15) erg s ⁻¹	log L _{tot} (16) erg s ⁻¹
NGC 3756	11 36 48.02	+54 17 36.8	23.5	SAB(rs)bc	H	H	20	+	0.31×0.20	-177.7	66	U	—	<35.29	—
NGC 3780	11 39 22.36	+56 16 14.4	37.2	SA(s)c:	L2::	L ⁱ	20	+	0.22×0.15	-45.6	80	U	—	<35.78	—
NGC 3813	11 41 18.66	+36 32 48.5	26.4	SA(rs)b:	H	H	13	+	0.20×0.19	38.8	90	U	—	<35.53	—
NGC 3838	11 44 13.76	+57 56 53.6	24.6	SA0/a?	ALG	ALG ^k	20	+	0.32×0.21	-154.9	84	unI	—	<35.44	—
NGC 3884	11 46 12.18	+20 23 29.9	91.6	SA(r)0/a	L1.9	L	12	m	0.41×0.41	0.0	167	I	A	37.79	37.80
NGC 3900	11 49 09.46	+27 01 19.3	29.4	SA(r)0+	L2:	ALG	12	m	0.50×0.17	-41.7	91	U	—	<35.63	—
NGC 3898	11 49 15.37	+56 05 03.7	21.9	SA(s)ab	T2	L ^{b,k}	20	+	0.30×0.19	-175	75	I	A	35.84	36.11
NGC 3917	11 50 45.43	+51 49 28.8	17.0	SAcd:	T2:	L	19	++	0.19×0.15	-44.1	70	U	—	<35.04	—
NGC 3941	11 52 55.36	+36 59 10.8	18.9	SB(s)0	S2:	S ^b	13	+	0.20×0.19	41.1	90	I	A	35.46	35.70
NGC 3945	11 53 13.73	+60 40 32.0	22.5	(R)SB(rs)0+	L2	L	21	++	0.17×0.14	33.5	75	I	C	35.77	35.86
NGC 3953	11 53 48.92	+52 19 36.4	17.0	SB(r)bc	T2	L	19	++	0.19×0.15	-43.8	76	U	—	<35.07	—
NGC 3963	11 54 58.71	+58 29 37.1	42.7	SAB(rs)bc	H	H	20	+	0.24×0.15	-42.8	76	I	A	36.03	36.09
NGC 3982	11 56 28.13	+55 07 30.9	17.0	SAB(r)b:	S1.9	S	20	+	0.18×0.12	-60.6	106	I	A	36.15	36.36
NGC 3992	11 57 35.98	+53 22 28.3	17.0	SB(rs)bc	T2:	L ^{b,l}	19	++	0.19×0.15	-43.9	76	U	—	<35.07	—
NGC 3998	11 57 56.13	+55 27 12.9	21.6	SA(r)0?	L1.9	L	20	+	0.32×0.20	-4.0	272	I	A	37.98	37.98
NGC 4026	11 59 25.19	+50 57 42.1	17.0	SA0 spin	ALG	L ^{b,m,n}	19	++	0.20×0.15	-40.6	83	U	—	<35.11	—
NGC 4036	12 01 26.75	+61 53 44.8	24.6	SA0-	L1.9	L	21	++	0.17×0.14	34.7	74	I	C	35.99	36.94
NGC 4041	12 02 12.20	+62 08 14.0	22.7	SA(rs)bc:	H	H	21	++	0.17×0.15	30.1	71	I	E	35.50	36.51
NGC 4062	12 04 03.83	+31 53 44.9	9.7	SA(s)c	H	H	13	+	0.21×0.19	52.6	85	U	—	<34.63	—
NGC 4088	12 05 34.19	+50 32 20.5	17.0	SAB(rs)bc	H	H	19	++	0.20×0.14	-44.0	81	U	—	<35.10	—
NGC 4096	12 06 01.13	+47 28 42.4	8.8	SAB(rs)c	H	H	19	++	0.20×0.16	-49.5	81	U	—	<34.53	—
NGC 4100	12 06 08.45	+49 34 57.7	17.0	(R')SA(rs)bc	H	H	19	++	0.20×0.16	-55.9	83	I	A	35.36	35.76
NGC 4102	12 06 22.99	+52 42 39.9	17.0	SAB(s)b?	H	H	19	++	0.20×0.15	-42.9	91	I	E	35.91	37.55
NGC 4111	12 07 03.13	+43 03 56.6	17.0	SA(r)0+: spin	L2	L	15	+	0.40×0.23	16.1	102	I+unI	A	35.41	35.83
NGC 4125	12 08 06.02	+65 10 26.9	24.2	E6 pec	T2	L ^b	21	++	0.17×0.13	34.5	73	U	—	<35.36	—
NGC 4136	12 09 17.69	+29 55 39.4	9.7	SAB(r)c	H	H	13	+	0.22×0.20	30.1	90	U	—	<34.66	—
NGC 4138	12 09 29.78	+43 41 07.1	17.0	SA(r)0+	S1.9	L	15	+	0.43×0.24	17.5	125	U	—	<35.29	—
NGC 4143	12 09 36.06	+42 32 03.0	17.0	SAB(s)0	L1.9	L	15	+	0.42×0.20	9.7	117	I	B	36.13	36.22
NGC 4144	12 09 58.60	+46 27 25.8	4.1	SAB(s)cd? spin	H	H	15	+	0.39×0.20	-176.5	115	U	—	<34.02	—
NGC 4145	12 10 01.52	+39 53 01.9	20.7	SAB(rs)d	T2:	H ⁱ	14	++	0.26×0.17	39.3	66	U	—	<35.18	—
NGC 4151	12 10 32.58	+39 24 20.6	20.3	(R')SAB(rs)ab:	S1.5	S	14	++	0.26×0.16	38.8	201	I	C	37.75	38.35
NGC 4150	12 10 33.65	+30 24 05.5	9.7	SA(r)0?	T2	L	13	+	0.22×0.20	34.3	82	U	—	<34.62	—
NGC 4157	12 11 04.37	+50 29 04.8	17.0	SAB(s)b? spin	H	H	19	++	0.19×0.16	-51.2	76	U	—	<35.07	—
NGC 4162	12 11 52.47	+24 07 25.2	38.5	(R)SA(rs)bc	H	H	12	m	0.57×0.18	-39.3	120	unI	—	<35.98	—
NGC 4169	12 12 18.78	+29 10 45.9	50.4	SA0	S2	S	13	+	0.22×0.20	37.1	88	U	—	<36.08	—
NGC 4183	12 13 16.88	+43 41 54.9	17.0	SA(s)cd? spin	H	H	15	+	0.41×0.19	10.4	96	U	—	<35.17	—
NGC 4203	12 15 05.06	+33 11 50.4	9.7	SAB0-:	L1.9	L	13	+	0.22×0.18	54.7	142	I	A	36.09	36.11
NGC 4214	12 15 39.17	+36 19 36.8	3.5	IAB(s)m	H	H	13	+	0.22×0.19	49.9	80	U	—	<33.72	—
NGC 4217	12 15 50.90	+47 05 30.4	17.0	SAb spin	H	H	15	+	0.46×0.26	8.0	85	I	C	35.23	35.96
NGC 4220	12 16 11.71	+47 52 59.7	17.0	SA(r)0+	T2	L	15	+	0.38×0.21	6.8	83	I	A	35.25	35.72

Continued on Next Page

Table A1 – Continued

Name (1)	RA (2)	DEC (3)	D (4) Mpc	Hubble (5) type	class (6) Ho97	class (7) BPT	LEM (8)	Q (9)	Beam (10) arcsec ²	PA (11) degree	rms (12) $\mu\text{Jy/b}$	det (13)	morph (14)	log L _{core} (15) erg s ⁻¹	log L _{tot} (16) erg s ⁻¹
NGC 4236	12 16 42.12	+69 27 45.3	2.2	SB(s)dm	H	H	21	++	0.16×0.12	25.0	71	unI	—	<33.27	—
NGC 4244	12 17 29.66	+37 48 25.6	3.1	SA(s)cd: spin	H	H	13	+	0.20×0.20	33.7	86	I	A	33.83	33.94
NGC 4242	12 17 30.18	+45 37 09.5	7.5	SAB(s)dm	H::	H: ⁱ	15	+	0.42×0.25	8.3	86	unI	—	<34.42	—
NGC 4245	12 17 36.77	+29 36 28.8	9.7	SB(r)0/a:	H	H	12	m	0.56×0.18	-38.9	87	U	—	<34.64	—
NGC 4251	12 18 08.25	+28 10 31.4	9.7	SB0? spin	ALG	ALG	12	m	0.57×0.18	-39.5	90	U	—	<34.66	—
NGC 4258	12 18 57.50	+47 18 14.3	6.8	SAB(s)bc	S1.9	S	15	+	0.42×0.25	-176.3	87	I	A	34.93	35.06
NGC 4274	12 19 50.59	+29 36 52.1	9.7	(R)SB(r)ab	H	L ^{b,o}	12	m	0.55×0.19	-39.3	83	U	—	<34.62	—
NGC 4278	12 20 06.82	+29 16 50.7	9.7	E1+	L1.9	L	12	m	0.32×0.32	-38.8	110	I	A	37.61	37.63
NGC 4291	12 20 18.20	+75 22 15.0	29.4	E	ALG	ALG	21	++	0.16×0.12	26.5	68	U	—	<35.50	—
NGC 4314	12 22 31.82	+29 53 45.2	9.7	SB(rs)a	L2	L ^{d,p}	12	m	0.52×0.20	-38.7	89	U	—	<34.65	—
NGC 4346	12 23 27.94	+46 59 37.8	17.0	SA0 spin	L2::	L ^m	15	+	0.39×0.22	6.1	123	U	—	<35.28	—
NGC 4369	12 24 36.20	+39 22 58.8	21.6	(R)SA(rs)a	H	H	MISC1	+	0.19×0.17	78.1	38	I	A	35.18	35.40
NGC 4395	12 25 48.86	+33 32 48.9	3.6	SA(s)m:	S1.8	S	13	+	0.22×0.18	56.2	110	I	A	34.17	34.39
NGC 4414	12 26 27.10	+31 13 24.7	9.7	SA(rs)c?	T2:	L ^{b,c}	12	m	0.49×0.19	-39.8	94	U	—	<34.68	—
NGC 4449	12 28 11.10	+44 05 37.1	3.0	IBm	H	H	14	++	0.24×0.17	35.8	79	U	—	<33.58	—
NGC 4448	12 28 15.43	+28 37 13.1	9.7	SB(r)ab	H	H	11	++	0.23×0.20	53.5	58	U	—	<34.47	—
NGC 4460	12 28 45.56	+44 51 51.2	8.1	SB(s)0+? spin	H	H	14	++	0.25×0.17	34.6	65	U	—	<34.36	—
NGC 4485	12 30 31.13	+41 42 04.2	9.3	IB(s)m pec	H	H ^q	MISC1	+	0.19×0.16	69.1	45	U	—	<34.32	—
NGC 4490	12 30 36.24	+41 38 38.0	7.8	SB(s)d pec	H	H ^{f,g}	14	++	0.25×0.16	32.8	66	U	—	<34.33	—
NGC 4494	12 31 24.10	+25 46 30.9	9.7	E1+	L2::	L ^m	11	++	0.23×0.20	49.3	67	I	A	34.69	34.92
NGC 4559	12 35 57.65	+27 57 36.0	9.7	SAB(rs)cd	H	H	11	++	0.22×0.20	52.5	61	U	—	<34.49	—
NGC 4565	12 36 20.78	+25 59 15.6	9.7	SA(s)b? spin	S1.9	S	11	++	0.22×0.20	44.4	68	I	A	35.20	35.31
NGC 4589	12 37 25.00	+74 11 30.9	30.0	E2	L2	L	21	++	0.16×0.12	30.9	85	I	C	37.45	37.60
NGC 4605	12 39 59.38	+61 36 33.1	4.0	SB(s)c pec	H	H	21	++	0.17×0.13	46.3	69	U	—	<33.77	—
NGC 4618	12 41 32.85	+41 09 02.8	7.3	SB(rs)m	H	H	14	++	0.25×0.16	33.2	66	U	—	<34.28	—
NGC 4648	12 41 44.39	+74 25 15.4	27.5	E3	ALG	ALG	21	++	0.16×0.12	29.8	70	U	—	<35.45	—
NGC 4631	12 42 08.01	+32 32 29.4	6.9	SB(s)d spin	H	H	11	++	0.21×0.20	77.9	77	unI	—	<34.30	—
NGC 4656	12 43 57.73	+32 10 05.3	7.2	SB(s)m pec	H	H	11	++	0.21×0.20	70.1	74	U	—	<34.32	—
NGC 4750	12 50 07.27	+72 52 28.7	26.1	(R)SA(rs)ab	L1.9	L	21	++	0.16×0.12	27.2	61	I	A	35.84	36.17
NGC 4725	12 50 26.58	+25 30 02.9	12.4	SAB(r)ab pec	S2:	S	11	++	0.21×0.20	70.9	73	U	—	<34.78	—
NGC 4736	12 50 53.06	+41 07 13.7	4.3	(R)SA(r)ab	L2	L ^{c,r}	14	++	0.25×0.16	33.1	91	I	A	34.82	35.29
NGC 4800	12 54 37.80	+46 31 52.2	15.2	SA(rs)b	H	H	14	++	0.24×0.16	33.9	66	U	—	<34.91	—
NGC 4793	12 54 40.62	+28 56 19.2	38.9	SAB(rs)c	H	H	11	++	0.21×0.19	73.5	74	U	—	<35.78	—
NGC 4826	12 56 43.64	+21 40 58.7	4.1	(R)SA(rs)ab	T2	L ^{b,r}	11	++	0.22×0.20	46.4	74	I	A	33.88	34.93
NGC 5012	13 11 37.04	+22 54 55.8	40.4	SAB(rs)c	T2	L	11	++	0.23×0.20	42.5	79	unI	—	<35.84	—
NGC 5033	13 13 27.47	+36 35 38.2	18.7	SA(s)c	S1.5	L	MISC1	+	0.18×0.16	52.7	54	I	A	36.04	36.42
NGC 5204	13 29 36.51	+58 25 07.4	4.8	SA(s)m	H	H	08	m	0.34×0.21	29.8	112	U	—	<34.14	—
NGC 5308	13 47 00.43	+60 58 23.4	32.4	SA0- spin	ALG	ALG	08	m	0.31×0.21	34.2	116	U	—	<35.82	—
NGC 5322	13 49 15.27	+60 11 25.9	31.6	E3+	L2::	L ^s	08	m	0.31×0.22	33.0	117	I	B	36.96	37.51
NGC 5354	13 53 26.70	+40 18 09.9	32.8	SA0 spin	T2/L2:	L	MISC1	+	0.19×0.16	67.1	74	I	A	36.94	36.97

Continued on Next Page

Table A1 – Continued

Name (1)	RA (2)	DEC (3)	D (4) Mpc	Hubble (5) type	class (6) Ho97	class (7) BPT	LEM (8)	Q (9)	Beam (10) arcsec ²	PA (11) degree	rms (12) $\mu\text{Jy/b}$	det (13)	morph (14)	log L_{core} (15) erg s ⁻¹	log L_{tot} (16) erg s ⁻¹
NGC 5457	14 03 12.54	+54 20 56.2	5.4	SAB(rs)cd	H	H	08	m	0.36×0.18	19.9	120	U	–	<34.28	–
NGC 5473	14 04 43.23	+54 53 33.5	33.0	SAB(s)0-:	ALG	ALG	08	m	0.36×0.18	20.1	112	U	–	<35.82	–
NGC 5474	14 05 01.61	+53 39 44.0	6.0	SA(s)cd pec	H	H	08	m	0.39×0.20	15.7	124	U	–	<34.38	–
NGC 5485	14 07 11.35	+55 00 06.1	32.8	SA0 pec	L2:	L ^t	08	m	0.30×0.30	27.1	178	I	A	36.44	36.44
NGC 5548	14 17 59.53	+25 08 12.4	67.0	(R')SA(s)0/a	S1.5	S	MISC1	+	0.21×0.14	-161.6	63	I	B	36.96	37.61
NGC 5585	14 19 48.20	+56 43 44.6	7.0	SAB(s)d	H	H	08	m	0.38×0.18	28.5	128	U	–	<34.53	–
NGC 5631	14 26 33.30	+56 34 57.5	32.7	SA(s)0	S2/L2:	L ^m	08	m	0.38×0.18	31.0	135	U	–	<35.89	–
NGC 5678	14 32 05.61	+57 55 17.2	35.6	SAB(rs)b	T2	H	08	m	0.39×0.18	34.3	125	U	–	<35.93	–
NGC 6217	16 32 39.20	+78 11 53.4	23.9	(R)SB(rs)bc	H	H	06	+	0.17×0.14	72.4	102	I	A	35.66	36.59
NGC 6207	16 43 03.75	+36 49 56.7	17.4	SA(s)c	H	H	06	+	0.22×0.17	76.6	95	U	–	<35.19	–
NGC 6236	16 44 34.65	+70 46 48.8	23.3	SAB(s)cd	H	H	06	+	0.18×0.15	65.9	85	U	–	<35.40	–
NGC 6340	17 10 24.85	+72 18 16.0	22.0	SA(s)0/a	L2	L	06	+	0.17×0.15	69.8	84	I	A	35.53	36.03
NGC 6412	17 29 37.51	+75 42 15.9	23.5	SA(s)c	H	H	06	+	0.17×0.14	80.9	84	U	–	<35.40	–
NGC 6503	17 49 26.43	+70 08 39.7	6.1	SA(s)cd	T2/S2:	L ^r	06	+	0.18×0.14	71.4	100	U	–	<34.30	–
NGC 6482	17 51 48.81	+23 04 19.0	52.3	E:	T2/S2::	L ^b	06	+	0.19×0.16	51.3	112	I	A	36.37	36.74
NGC 6643	18 19 46.41	+74 34 06.1	25.5	SA(rs)c	H	H	06	+	0.17×0.15	82.9	84	U	–	<35.47	–
NGC 6654	18 24 07.57	+73 10 59.6	29.5	(R')SB(s)0/a	ALG	ALG	06	+	0.17×0.15	81.0	87	U	–	<35.61	–
NGC 6689	18 34 50.25	+70 31 26.1	12.2	SA d? spin	H	L	06	+	0.18×0.14	80.2	89	U	–	<34.85	–
NGC 7080	21 30 01.95	+26 43 04.1	64.1	SB(r)b	H	H:	MISC1	+	0.31×0.15	4.3	54	I	A	36.50	36.91

Column description: (1) source name; (2)-(3) RA and DEC position (J2000.0) from NED, using optical or infrared images; (4) distance (Mpc) from [Ho et al. \(1997\)](#); (5) morphological galaxy type given from RC3 ([de Vaucouleurs et al. 1991](#)); (6) optical spectroscopic classification based on [Ho et al. \(1997\)](#): H=HII, S=Seyfert, L=LINER, T=Transition object, and ALG=Absorption line galaxy. The number attached to the class letter designates the AGN type (between 1 and 2); quality ratings are given by ':' and '::' for uncertain and highly uncertain classification, respectively. Two classifications are given for some ambiguous cases, where the first entry corresponds to the adopted choice; (7) optical spectroscopic classification based on BPT diagrams and from the literature. See the notes for the classification based on the literature; (8) LeMMINGs observation block; (9) raw data and calibration quality: '++' = very good; '+' = good; 'm' = moderate; (10) restoring beam size in arcsec in full resolution map; (11) PA angle (degree) in full resolution map; (12) rms in full resolution map in $\mu\text{Jy beam}^{-1}$; (13) radio detection status of the source: 'I' = detected and core identified; 'U' = undetected; 'unI' = detected but core unidentified; 'I+unI' = detected and core identified with additional unknown source(s) in the field; (14) radio morphological class: A = core/core-jet; B = one-sided jet; C = triple; D = doubled-lobed; E = jet+complex (see Sect 4.2); (15)-(16) logarithm of the radio core and total luminosities (erg s⁻¹). To convert the radio luminosities from erg s⁻¹ to monochromatic luminosities (W Hz⁻¹) at 1.5 GHz, an amount +16.18 should be subtracted to the logarithm of the luminosities presented in the Table.

Notes: letters correspond to following publications: *a* [Keel \(1983\)](#); *b* [van den Bosch et al. \(2015\)](#); *c* [Moustakas & Kennicutt \(2006\)](#); *d* [Florido et al. \(2012\)](#); *e* [Buttiglione et al. \(2010\)](#); *f* [Gavazzi et al. \(2013\)](#); *g* [Heckman \(1980\)](#); *h* [Balmaverde & Capetti \(2013\)](#); *i* SDSS; *j* [Gavazzi et al. \(2018\)](#); *k* [Cazzoli et al. \(2018\)](#); *l* [Shields et al. \(2007\)](#); *m* [Nyland et al. \(2016\)](#); *n* [Serra et al. \(2008\)](#); *o* [Wegner et al. \(2003\)](#); *p* [Pişmiş et al. \(2001\)](#); *q* [Kennicutt \(1992\)](#); *r* [Lira et al. \(2007\)](#); *s* [Baldi & Capetti \(2009\)](#); *t* [García-Lorenzo et al. \(2015\)](#).

Table A2: Properties of the detected and core-identified sources.

name	comp	$\theta_{\rm M} \times \theta_{\rm m}$ arcsec ²	PA _d deg	Full resolution					Low resolution					morph/size
				rms mJy/b	α (J2000)	δ (J2000)	F _{peak} mJy/b	F _{tot} mJy	$u-v$ k λ	$\theta_{\rm M} \times \theta_{\rm m}$ arcsec ²	PA _d deg	rms mJy/b	F _{peak} mJy/b	
NGC 1161	core	0.06×0.01	53.7	0.067	03 01 14.173	44 53 50.66	3.09±0.07	3.13	500	<0.43×<0.26	-53.7	0.066	3.00±0.07	core (A)
				0.067	03 01 14.242	44 53 50.77	<0.22		500	<0.69×<0.26	139.8	0.066	0.61±0.08	
	Tot												4.1±0.2	
NGC 1167	core	0.08×0.07	19	2.7	03 01 42.331	35 12 20.30	580.1±10.0	695	500	0.20×0.10	114	3.1	618±11	core-jet (A) 1'' →310pc
		0.35×0.14	113	2.7	03 01 42.361	35 12 20.10	49.0±11.0	121	500			3.1	<75	
				2.7	03 01 42.226	35 12 21.65	<30	121	500	0.18×0.10	113	3.1	20±5	
	Tot												755±28	
NGC 1186	core	<0.26×<0.16	134.4	0.065	03 05 30.951	42 50 07.95	0.36±0.07	0.71	750	<0.45×<0.18	129.7	0.067	0.61±0.07	complex (E) multi- components 2.5'' →423pc
		<0.33×<0.11	61.0	0.065	03 05 30.874	42 50 08.08	<0.20		750	0.29×<0.16	61	0.067	0.27±0.07	
		<0.18×<0.14	150	0.065	03 05 30.965	42 50 07.36	<0.22		750	0.32×<0.18	143	0.067	0.29±0.08	
		0.19×0.06	91	0.065	03 05 30.823	42 50 08.86	0.26±0.08	0.40	750	<0.32×<0.17	131	0.067	0.28±0.08	
		<0.16×<0.12	48	0.065	03 05 30.796	42 50 08.24	0.34±0.09	0.38	750	<0.39×<0.16	128	0.067	0.31±0.08	
		0.26×<0.06	142	0.065	03 05 30.852	42 50 07.64	<0.20		750	0.62×0.04	124	0.067	0.24±0.08	
	Tot												2.7±0.1	
NGC 1275	core	0.21×0.10	143.3	156	03 19 48.161	41 30 42.04	10500±160	11160	750	0.34×0.13	159	216	105700±310	core-jet (A)
	Tot												47136±2500	2'' →664pc
IC 356	core	<0.31×<0.15	126	0.108	04 07 46.890	69 48 44.70	0.56±0.11	0.43	300	<0.40×<0.31	169	0.070	0.22±0.07	core (A)
				0.108	04 07 46.953	69 48 45.09	<0.36		300	<0.72×<0.56	99	0.070	0.32±0.08	
	Tot												0.93±0.20	
NGC 1560	core	0.20×0.14	27	0.102	04 32 49.008	71 52 59.67	0.37±0.10	0.64	300	0.49×<0.03	45	0.075	0.53±0.04	core (A)
	Tot												0.81±0.10	
NGC 1961	core	0.14×0.08	121	0.126	05 42 04.638	69 22 42.38	2.81±0.16	3.46	300	0.28×0.08	13.6	0.085	3.12±0.10	core (A)
	Tot												3.5±0.2	
NGC 2146	core	0.09×0.04	32	0.263	06 18 37.589	78 21 24.25	4.10±0.27	4.61	300	0.19×0.10	135	0.134	4.23±0.17	one-sided jet (B) 1.5'' →87pc
		0.56×0.36	152	0.263	06 18 37.771	78 21 23.62	1.75±0.27	8.87	300	0.72×0.42	68.2	0.131	2.52±0.06	
	Tot												13.7±1.0	
NGC 2683	core	<0.24×<0.16	27.1	0.048	08 52 41.302	33 25 18.75	0.53±0.05	0.56	500	<0.33×<0.31	114	0.044	0.46±0.06	core (A)
		<0.28×<0.15	49.2	0.048	08 52 41.266	33 25 19.23	0.21±0.05	0.21	500	<0.37×<0.28	87	0.044	0.24±0.06	
	Tot												0.76±0.08	
NGC 2768	core	0.06×0.05	144	0.186	09 11 37.414	60 02 14.86	12.63±0.39	14.26	500	0.12×0.05	152	0.180	13.13±0.26	core (A)
	Tot												15.2±0.6	
NGC 2782	core	0.28×0.09	2.8	0.051	09 14 05.104	40 06 49.23	2.46±0.07	4.78	750	0.37×0.14	3.2	0.048	2.72±0.09	core-jet? (A)
	Tot												5.8±0.1	
NGC 2787	core	0.14×0.02	153	0.127	09 19 18.599	69 12 11.64	6.11±0.28	8.44	750	0.14×0.03	144	0.140	6.64±0.16	core-jet? (A)
	Tot												8.5±0.3	
NGC 2832	core	0.18×<0.04	21	0.070	09 19 46.851	33 44 59.02	0.45±0.07	0.69	500	0.25×0.15	6.1	0.086	0.50±0.09	core (A)
	Tot												0.75±0.10	
NGC 2964	core	0.22×0.12	43.7	0.090	09 42 54.220	31 50 50.34	1.24±0.09	2.54	500	0.31×0.20	77	0.104	1.32±0.10	elongated

Continued on Next Page

Table A2 – Continued

name	comp	Full resolution							Low resolution					morph/size		
		$\theta_M \times \theta_m$ arcsec ²	PA _d deg	rms mJy/b	α (J2000)	δ (J2000)	F _{peak} mJy/b	F _{tot} mJy	$u-v$ k λ	$\theta_M \times \theta_m$ arcsec ²	PA _d deg	rms mJy/b	F _{peak} mJy/b			
		0.33×0.25	78	0.090	09 42 54.146	31 50 49.99	0.54±0.09	2.24	500	0.46×0.21	49.3	0.104	1.05±0.10	star-forming region? (E) 5.5'' →578pc		
				0.090	09 42 54.287	31 50 50.10	<0.48		500	0.52×0.32	67	0.104	0.65±0.10			
	Tot												10.8±0.5			
NGC 2985	core	0.11×0.07	87	0.096	09 50 22.184	72 16 44.21	0.72±0.10	0.75	500	0.28×0.04	83.8	0.113	0.74±0.11	core (A)		
	Tot												1.18±0.16			
NGC 3031	core	0.08×0.04	13	0.334	09 55 33.174	69 03 55.04	90.3±2.4	97.9	500	0.06×0.04	6	0.370	93.6±1.0	core (A)		
	Tot												98±5			
NGC 3077	core	0.25×0.17	109	0.092	10 03 19.097	68 44 02.37	0.60±0.09	1.27	500	0.26×0.10	100	0.100	0.74±0.10	core (A)		
		0.34×0.21	152	0.092	10 03 19.122	68 44 02.04	0.27±0.09	0.73	500	0.48×0.14	6.9	0.100	0.40±0.10			
	Tot												2.1±0.3			
NGC 3079	core	0.25×0.03	168	0.630	10 01 57.806	55 40 47.26	25.2±0.8	41.1	300	0.40×0.23	159	1.278	31.0±1.3	triple source (C) 2.5'' →210pc		
		0.54×0.22	12.1	0.630	10 01 57.798	55 40 46.32	5.1±0.8	16.7	300	0.60×0.37	19.4	1.278	9.70±1.3			
		0.43×0.20	144.5	0.630	10 01 57.774	55 40 48.02	5.1±0.9	10.0	300			1.278	<8.0			
	Tot												75±3			
NGC 3147	core	0.19×0.07	16	0.137	10 16 53.651	73 24 02.69	7.71±0.28	10.38	750	0.22×0.08	15	0.122	7.90±0.28	core (A)		
	Tot												10.7±0.6			
NGC 3245	core	0.25×0.21	39	0.070	10 27 18.386	28 30 26.63	0.58±0.07	1.55	300	0.69×0.32	143	0.046	1.02±0.06	complex (E) 2.5'' →268pc		
		0.43×0.16	81	0.070	10 27 18.406	28 30 26.40	0.30±0.07	1.03	300				<0.25			
	Tot												2.6±0.3			
NGC 3301	core	<0.24× <0.20	139	0.075	10 36 56.039	21 52 55.51	0.52±0.08	0.73	750	0.29×0.06	137	0.067	0.52±0.07	core (A)		
	Tot												0.75±0.13			
NGC 3310	core	0.39×0.30	27	0.110	10 38 45.865	53 30 12.06	0.64±0.11	1.83	750	0.48×0.43	54	0.102	0.66±0.10	core (A)		
	Tot												2.53±0.38			
NGC 3348	core	0.09×0.03	59	0.087	10 47 10.032	72 50 22.67	1.50±0.09	1.51	750	0.09×0.04	68.3	0.083	1.52±0.08	triple source (C) 1.2'' →228pc		
		0.19×0.06	146	0.087	10 47 09.948	72 50 22.94	0.32±0.10	0.37	750	<0.41× <0.21	130	0.083	0.34±0.08			
		<0.30× <0.19	121	0.087	10 47 10.104	72 50 22.29	0.28±0.09	0.36	750	<0.45× <0.20	108	0.083	0.32±0.08			
	Tot												2.1±0.2			
NGC 3448	core	0.36×0.09	1.3	0.079	12 54 39.266	54 18 15.73	0.33±0.08	0.66	300	<0.40× <0.29	167	0.092	0.51±0.09	core + components? (A)		
		0.56×0.10	81	0.079	12 54 39.225	54 18 21.05	0.40±0.08	0.99	300	<0.56× <0.37	101	0.092	0.59±0.09			
		<0.25× <0.20	63	0.079	12 54 39.258	54 18 21.91	0.42±0.08	0.43	300			0.092	<0.29			
	Tot												2.1±0.2			
NGC 3504	core	0.32×0.13	63	0.057	11 03 11.249	27 58 21.47	15.93±0.50	34.43	500	0.34×0.13	62.4	0.071	20.85±0.57	core-jet? (A)		
	Tot												35.7±2.0			
NGC 3516	core	0.18×0.06	30	0.103	11 06 47.465	72 34 07.26	2.55±0.12	3.11	{	500	0.18×0.04	25	0.200	2.72±0.20	twin jets (C) 9'' →1.6kpc	
											300	0.12×0.07	44	0.149		2.70±0.16
											500	2.5×0.81	179	0.200		0.79±0.21
			0.97×0.53	3	0.103	11 06 47.555	72 34 09.26	0.39±0.10		5.11	300	1.16×0.47	177	0.149		2.70±0.16
											500	0.68×0.42	37	0.200		0.62±0.20
			0.65×0.30	47	0.103	11 06 47.233	72 34 09.13	0.47±0.10		2.68	300	0.62×0.39	34	0.149		0.65±0.17

Continued on Next Page

Table A2 – Continued

name	comp	Full resolution								Low resolution					morph/size
		$\theta_M \times \theta_m$ arcsec ²	PA _d deg	rms mJy/b	α (J2000)	δ (J2000)	F _{peak} mJy/b	F _{tot} mJy	$u-v$ k λ	$\theta_M \times \theta_m$ arcsec ²	PA _d deg	rms mJy/b	F _{peak} mJy/b		
	Tot												3.26±0.32		
NGC 3718	core	<0.33×<0.20	4.6	0.086	11 32 34.852	53 04 04.53	11.62±0.10	11.65	500	<0.49×<0.35	175.8	0.094	11.55±0.12	core (A)	
	Tot												11.7±0.2		
NGC 3729	core	0.42×0.25	103	0.086	11 33 49.382	53 07 32.13	1.37±0.11	4.17	500	0.44×0.29	122	0.097	2.23±0.10	core (A)	
	Tot												4.2±0.1		
NGC 3735	core	0.22×0.06	8.5	0.088	11 35 57.216	70 32 07.81	0.57±0.09	0.93	750	0.29×0.17	40	0.085	0.59±0.09	core (A)	
	Tot												1.05±0.15		
NGC 3884	core	<0.66×<0.26	138	0.145	11 46 12.181	20 23 29.93	4.09±0.20	4.10	750	<0.48×<0.38	130	0.173	2.63±0.20	core (A)	
	Tot												4.2±0.2		
NGC 3898	core	0.27×0.14	4.8	0.075	11 49 15.236	56 05 04.38	0.80±0.08	1.31	500	0.42×0.23	152	0.082	0.92±0.08	core (A)	
	Tot												1.5±0.1		
NGC 3941	core	0.25×0.08	94	0.090	11 52 55.368	36 59 11.41	0.45±0.09	0.79	500	<0.25×<0.24	0.0	0.085	0.54±0.08	core (A)	
	Tot												0.79±0.11		
NGC 3945	core	<0.19×<0.14	10	0.075	11 53 13.612	60 40 32.13	0.65±0.08	0.68	300	<0.44×<0.39	24	0.083	0.63±0.08	triple source (C) 1.3'' →122pc	
				0.075	11 53 13.675	60 40 31.85	<0.23		300	<0.79×<0.24	178.9	0.083	0.30×0.08		
	Tot												0.8±0.1		
NGC 3963	core	<0.24×<0.12	153.4	0.076	11 54 58.738	58 29 36.40	0.33±0.08	0.35	500	<0.67×<0.26	168.6	0.088	0.35±0.09	core (A)	
	Tot												0.38±0.10		
NGC 3982	core	<0.23×<0.14	138.2	0.106	11 56 28.140	55 07 30.91	2.73±0.11	4.30	500	0.15×0.08	172.7	0.106	3.82±0.11	core (A)	
	Tot												4.4±0.4		
NGC 3998	core	<0.33×<0.19	175.5	0.272	11 57 56.133	55 27 12.93	113.9±1.4	114.2	500	0.73×0.32	174	0.136	112.5±2.4	core (A)	
	Tot												114.5±2.6		
NGC 4036	core	0.28×0.03	58.3	0.074	12 01 26.743	61 53 44.56	0.90±0.08	1.71	{	500	<0.34×<0.26	54.5	0.079	1.19±0.09	twin jets (C) 5'' →500pc
										300	<0.44×<0.34	33.7	0.079	1.10±0.08	
										500	0.13×0.02	9.2	0.079	2.97±0.09	
	blob W	0.14×0.05	14.8	0.074	12 01 26.478	61 53 44.02	2.41±0.1	3.36		300	<0.44×<0.39	178.9	0.079	3.06±0.08	
										500	0.52×0.22	1.8	0.079	0.60±0.10	
	blob E			0.074	12 01 27.135	61 53 45.38	<0.30			300	0.54×0.21	179	0.079	0.60±0.09	
	Tot												8.0±0.2		
NGC 4041		0.25×0.12	18	0.071	12 02 12.253	62 08 14.33	0.42±0.07	0.96	500	0.49×0.31	10.2	0.073	0.63±0.07	complex (E) 1.3'' →117pc	
	core	0.20×0.14	85	0.071	12 02 12.279	62 08 13.94	0.34±0.07	0.57	500	0.37×0.22	97.1	0.073	0.51±0.07		
		<0.20×<0.13	55.7	0.071	12 02 12.352	62 08 13.62	0.27±0.07	0.29	500	<0.35×<0.24	69.1	0.073	0.24±0.07		
		<0.19×<0.14	33	0.071	12 02 12.084	62 08 14.45	0.27±0.07	0.29	500	0.29×0.26	-27.2	0.073	0.24±0.07		
	Tot												3.5±0.2		
NGC 4100	core	0.30×0.09	96.5	0.083	12 06 08.440	49 34 56.46	0.44±0.08	1.02	750	0.30×0.07	104	0.083	0.53±0.08	core (A)	
	Tot												1.1±0.1		
NGC 4102	core	0.51×0.32	139	0.123	12 06 23.077	52 42 39.76	1.55±0.14	9.40	500	0.49×0.34	158	0.148	2.26±0.16	extended star forming region	
		0.39×0.27	110	0.123	12 06 23.008	52 42 39.13	0.82±0.12	3.84	500	0.33×0.33	31	0.148	1.68±0.15		

Continued on Next Page

Table A2 – Continued

name	comp	Full resolution								Low resolution					morph/size
		$\theta_M \times \theta_m$ arcsec ²	PA _d deg	rms mJy/b	α (J2000)	δ (J2000)	F _{peak} mJy/b	F _{tot} mJy	$u-v$ k λ	$\theta_M \times \theta_m$ arcsec ²	PA _d deg	rms mJy/b	F _{peak} mJy/b		
		0.60×0.36	49	0.123	12 06 23.059	52 42 40.69	0.87±0.12	7.57	500	0.81×0.39	69	0.148	1.45±0.17	(E)	
		0.23×0.17	93	0.123	12 06 22.982	52 42 38.56	0.77±0.13	1.87	500	0.57×0.28	98	0.148	1.26±0.16	3.5'' →238pc	
NGC 4111	Tot												68.1±0.7		
	core	0.43×0.14	43	0.102	12 07 03.136	43 03 56.45	0.49±0.10	0.91	500	0.56×0.36	52	0.110	0.44±0.11	core (A)	
	Tot												1.30±0.22		
	core	<0.31×<0.22	20.0	0.117	12 09 36.070	42 32 03.05	2.63±0.13	2.59	500	<0.67×<0.45	26.9	0.117	2.32±0.14	one-sided jet	
NGC 4143		<0.56×<0.17	8.4	0.117	12 09 36.122	42 32 03.16	0.93±0.12	1.07	500	0.51×0.13	22	0.117	0.96±0.04	(B)	
	Tot												3.2±0.3	1.5'' →117pc	
NGC 4151	core	0.53×0.29	86.9	0.201	12 10 32.426	39 24 20.66	10.48±0.55	51.7	500	0.57×0.30	85.9	0.237	16.77±0.79	twin jets (C) 4'' →328pc	
		0.37×0.21	50.7	0.201	12 10 32.507	39 24 30.88	20.08±0.73	57.4	500	0.47×0.22	56.0	0.237	29.59±0.14		
		0.22×0.12	73	0.201	12 10 32.542	39 24 21.01	32.5±1.3	55.0	500	0.53×0.12	79.2	0.237	41.12±0.63		
		0.10×0.05	75.3	0.201	12 10 32.582	39 24 21.07	75.99±0.58	86.2	500	0.14×0.06	76.2	0.237	81.57±0.34		
		0.37×0.20	63	0.201	12 10 32.654	39 24 21.35	8.67±0.57	24.2	500	0.49×0.25	74.2	0.237	12.11±0.42		
	Tot												302±12.5		
NGC 4203	core	0.08×0.04	0.0	0.115	12 15 05.055	33 11 50.39	7.36±0.17	7.65	500	<0.28×<0.23	0.0	0.115	7.56±0.18	core (A)	
	Tot												7.7±0.3		
NGC 4217	core	0.55×0.07	0.4	0.085	12 15 50.792	47 05 30.70	0.33±0.09	0.49	300	<0.78×<0.36	175	0.110	0.37±0.11	triple source? (C)	
				0.085	12 15 50.846	47 05 29.56	<0.26	300	1.11×0.47	163	0.110	0.48±0.07			
	Tot												1.74±0.20	3'' →246pc	
NGC 4220	core	0.26×0.13	4.4	0.087	12 16 11.709	47 52 59.02	0.34±0.09	0.49	300	<0.98×<0.37	169.3	0.101	0.33±0.10	core + components?	
		0.35×0.14	10	0.087	12 16 11.947	47 53 01.89	0.33±0.09	0.53	300	<0.77×<0.39	10	0.101	0.42±0.10		
	Tot												1.02±0.11	(A)	
NGC 4244	core	0.21×0.15	158	0.089	12 17 29.764	37 48 26.89	0.39±0.09	0.63	500	<0.39×0.30	165	0.074	0.51±0.08	core (A)	
	Tot												0.51±0.09		
NGC 4258	core	0.27×0.09	170	0.101	12 18 57.503	47 18 14.35	1.03±0.10	1.29	750	0.27×0.10	11	0.094	1.08±0.09	core-jet? (A)	
	Tot												1.37±0.19		
NGC 4278	core	0.09×0.04	142	0.824	12 20 06.825	29 16 50.73	239.1±1.8	251	750	0.12×0.05	150	0.974	240.2±1.7	core (A)	
	Tot												254±4		
NGC 4369	core			0.038	12 24 36.273	39 22 58.81	<0.12		300	0.40×0.20	52	0.043	0.18±0.05	core (A)	
	Tot												0.30±0.07		
NGC 4395	core	0.14×0.08	114	0.107	12 25 48.876	33 32 48.74	0.64±0.11	0.84	500	0.19×0.11	59	0.099	0.71±0.10	core-jet? (A)	
	Tot												1.05±0.16		
NGC 4494	core	<0.28×<0.20	49	0.067	12 31 24.032	25 46 30.04	0.29±0.07	0.34	750	0.26×0.23	58	0.071	0.34±0.07	core (A)	
	Tot												0.49±0.08		
NGC 4565	core	<0.19×<0.23	63	0.068	12 36 20.780	25 59 15.61	0.93±0.07	0.94	500	0.21×0.05	59	0.074	0.99±0.08	core (A)	
	Tot												1.2±0.1		
NGC 4589	core	0.16×0.12	37.6	0.085	12 37 24.988	74 11 30.89	17.51±0.09	18.0	750	<0.07×<0.04	0.0	0.200	17.35±0.06	triple source (C)	
		0.15×0.09	92.0	0.085	12 37 25.057	74 11 30.89	2.80±0.20	4.9	750	<0.20×<0.16	0.0	0.200	1.80±0.12		

Continued on Next Page

Table A2 – Continued

name	comp	Full resolution								Low resolution					morph/size
		$\theta_M \times \theta_m$ arcsec ²	PA _d deg	rms mJy/b	α (J2000)	δ (J2000)	F _{peak} mJy/b	F _{tot} mJy	$u-v$ k λ	$\theta_M \times \theta_m$ arcsec ²	PA _d deg	rms mJy/b	F _{peak} mJy/b		
		<0.16× <0.12	30.9	0.085	12 37 24.890	74 11 30.89	1.82±0.13	1.93	750	0.12×0.09	117	0.200	3.39±0.15	0.7'' →94pc	
	Tot												24.51±1.59		
NGC 4750	core	0.23×0.05	179	0.061	12 50 07.315	72 52 28.64	0.57±0.06	1.11	500	0.26×0.07	7	0.063	0.80±0.06	core (A)	
	Tot												1.2±0.1		
NGC 4736	core	0.20×0.17	100	0.087	12 50 53.018	41 07 13.53	1.97±0.10	3.78	500	0.23×0.12	100	0.097	2.62±0.12	core + components? (A) 2'' →70pc	
		<0.25× <0.14	31.2	0.087	12 50 53.070	41 07 12.89	0.75±0.09	0.66	500	0.20×0.05	33.1	0.097	0.68±0.12		
		0.72×0.05	24.4	0.087	12 50 53.076	41 07 14.47	0.57±0.09	1.53	500	<0.67× <0.23	22.8	0.097	0.77±0.12		
	Tot												5.85±0.15		
NGC 4826	core	0.35×0.15	170	0.074	12 56 43.655	21 40 58.58	0.25±0.07	0.64	300	0.51×0.34	33	0.080	0.67±0.08	core + components (A) 5'' →230pc	
		0.40×0.16	125	0.074	12 56 43.408	21 41 00.88	0.51±0.07	1.39	300	0.25×0.12	91	0.080	0.74±0.08		
		<0.26× <0.19	110	0.074	12 56 43.670	21 41 03.66	0.73±0.07	0.77	300	<0.34× <0.39	122	0.080	0.60±0.10		
	Tot												2.83±0.14		
NGC 5033	core	0.19×0.09	21.1	0.054	13 13 27.471	36 35 37.92	1.73±0.08	2.90	500	0.17×0.14	15	0.063	2.18±0.08	core + components? (A) 1.5'' →110pc	
		0.15×0.08	44	0.054	13 13 27.523	36 35 38.29	0.52±0.06	0.77	500	0.17×0.09	49	0.063	0.56±0.08		
		<0.58× <0.13	152	0.054	13 13 27.478	36 35 38.02	0.29±0.07	0.67	500	0.48×0.09	162	0.063	0.38±0.08		
	Tot												4.20±0.20		
NGC 5322		0.74×0.22	154	0.117	13 49 15.170	60 11 29.45	0.38±0.08	0.83	{ 500 300 500 300 500 300 500 300 500 300	0.64×0.28	5.6	0.134	0.52±0.05	one-sided jet (B) 14.5'' →1.8kpc	
										0.099	<0.6				
	core	<0.14× <0.03	0.0	0.117	13 49 15.265	60 11 25.94	5.13±0.12	5.35		0.16×0.07	16	0.134	4.90±0.13		
										0.19×0.08	4.6	0.099	5.02±0.11		
	<0.31× <0.22	0.0	0.117	3 49 15.279	60 11 25.29	1.17±0.08	1.27	<0.34× <0.16		0.0	0.134	1.26±0.08			
								0.66×0.04		156	0.099	1.42±0.11			
	0.37×0.24	116	0.117	13 49 15.278	60 11 24.30	0.51±0.08	0.98	0.38×0.17		126	0.134	0.45±0.05			
								0.73×0.44		100	0.099	0.74±0.10			
	0.30×0.24	102	0.117	13 49 15.321	60 11 21.81	0.55±0.06	0.88	0.57×0.33		30	0.134	0.62±0.07			
								0.73×0.41		24	0.099	1.64±0.10			
	Tot											18.1±0.18			
NGC 5354	core	0.07×0.02	44	0.074	13 53 26.713	40 18 09.92	4.47±0.07	4.78	500	<0.30× <0.27	112	0.082	4.52±0.09	core (A)	
	Tot												4.78±0.10		
NGC 5485	core	0.40×0.20	27.1	0.175	14 07 11.345	55 00 05.97	1.43±0.13	1.27	500	0.46×0.34	13.2	0.178	1.11±0.08	core (A)	
	Tot												1.30±0.14		
NGC 5548	core	<0.24× <0.15	176	0.063	14 17 59.540	25 08 12.61	1.14±0.06	1.40	{ 500 300 500 300 500 300	0.36×0.18	111.9	0.074	1.19±0.07	one-sided jet (B) 17'' →5.9kpc	
										<0.23×0.15	-161	0.083	1.21±0.08		
		0.26× <0.16	169	0.063	14 17 59.535	25 08 11.63	0.40±0.06	0.56		<0.26× <0.22	171.1	0.074	0.55±0.08		
										0.25×0.18	140	0.083	0.81±0.08		
			0.42×0.18	2.9	0.074	0.42±0.08									
	Tot												0.76±0.09		
													5.0±0.5		
NGC 6217	core	0.25×0.15	121	0.102	16 32 39.267	78 11 53.35	0.45±0.10	1.21	500	0.28×0.17	125	0.108	0.56±0.11	core + components (A)	
		0.31×0.24	120	0.102	16 32 39.546	78 11 52.46	0.33±0.10	1.29	0.36×0.30	161	0.108	0.36±0.11			
									0.41×0.31	148	0.108	0.38±0.11			

Continued on Next Page

Table A2 – Continued

name	comp	Full resolution								Low resolution					
		$\theta_M \times \theta_m$ arcsec ²	PA _d deg	rms mJy/b	α (J2000)	δ (J2000)	F _{peak} mJy/b	F _{tot} mJy	$u-v$ k λ	$\theta_M \times \theta_m$ arcsec ²	PA _d deg	rms mJy/b	F _{peak} mJy/b	morph/size	
		0.17×0.22	131	0.102	16 32 39.298	78 11 52.76	0.36±0.10	0.54	500	0.23×0.06	129	0.108	0.34±0.11	2'' → 176pc	
	Tot												3.82±0.18		
NGC 6340	core	0.21×0.08	89	0.086	17 10 24.827	72 18 15.85	0.39±0.09	1.02	300	0.48×0.11	165	0.120	0.67±0.12	core (A)	
	Tot												1.22±0.17		
NGC 6482	core	<0.27×<0.15	64.6	0.069	17 51 48.832	23 04 18.93	0.48±0.07	0.64	500	<0.32×0.22	-73	0.077	0.50±0.08	core+component	
		<0.20×<0.16	31	0.069	17 51 48.835	23 04 19.24	0.45±0.07	0.49	500	0.18×0.07	147	0.077	0.42±0.08	(A)	
	Tot												1.13±0.11	0.8'' → 202pc	
NGC 7080	core	0.21×0.16	164	0.054	21 30 01.966	26 43 00.96	0.43±0.05	0.77	500	<0.34×<0.18	8.6	0.061	0.38±0.07	core (A)	
	Tot												1.1±0.1		

Column description: (1) galaxy name; (2) radio component: core, jet, lobe, blob or unidentified component if not labeled (W or E stand for West or East); (3) deconvolved FWHM dimensions (major × minor axes [arcsec²], $\theta_M \times \theta_m$) of the fitted component, determined from an elliptical Gaussian fit from the full-resolution radio map; (4) PA of the deconvolved component, PA_d, from the full-resolution radio map (degree); (5) rms of the radio map close to the specific component from the full-resolution radio map (mJy/b, mJy beam⁻¹); (6)-(7) radio position (J2000.0); (8) peak flux density in mJy beam⁻¹, F_{peak}, from the full-resolution radio map: this represents the radio core flux density; (9) integrated flux density, F_{tot}, in mJy, from the full-resolution radio map; (10) uv -taper scale of the low-resolution radio map in k λ ; (11) deconvolved FWHM dimensions (major × minor axes [arcsec²], $\theta_M \times \theta_m$) of the fitted component, determined from an elliptical Gaussian fit from the low-resolution radio map; (12) PA of the deconvolved component, PA_d, from the low-resolution radio map (degree); (13) rms of the radio map close to the specific component from the low-resolution radio map (mJy beam⁻¹); (14) peak flux density in mJy beam⁻¹, F_{peak}, from the low-resolution radio map. For NGC 5194 we give the total integrated flux densities of the radio lobes instead of the peak flux densities. At the bottom of each target the total flux density of the radio source associated with the galaxy is given in mJy, measured from the low-resolution map; (15) radio morphology (A, B, C, D, E) and size in arcsec and pc (see Section 4.2).

Table A3: Properties of the unidentified sources.

name	comp	Full resolution							Low resolution					morph/size
		$\theta_M \times \theta_m$ arcsec ²	PA _d deg	rms mJy/b	α (J2000)	δ (J2000)	F _{peak} mJy/b	F _{tot} mJy	$u-v$ k λ	$\theta_M \times \theta_m$ arcsec ²	PA _d deg	rms mJy/b	F _{peak} mJy/b	
IC 342		0.13×0.05	141	0.175	03 46 48.464	68 05 48.41	1.61±0.18	1.79	500	0.21×0.05	154	0.177	1.35±0.18	multi- components 5.5'' → 100pc, >2'' offset
		0.54×0.38	163	0.175	03 46 47.926	68 05 47.28	1.18±0.18	5.18	500	0.60×0.54	57	0.177	1.69±0.18	
		0.36×0.30	142	0.175	03 46 48.701	68 05 43.83	0.86±0.18	2.30	500	1.20×0.44	165	0.177	0.60±0.18	
		<0.39× <0.20	137	0.175	03 46 47.884	68 05 44.14	0.94±0.18	1.11	500	<0.46× <0.30	156	0.177	0.81±0.18	
	Tot												10.2±0.9	
NGC 1569		0.61×0.39	99	0.115	04 30 54.026	64 50 42.62	0.38±0.11	1.81	300	0.84×0.32	57	0.148	0.95±0.15	triple source 2'' → 14pc, offset ~30''
	core	0.54×0.06	98	0.115	04 30 54.054	64 50.43.01	0.40±0.11	1.46	300			0.148	<0.42	
		0.92×0.29	138.0	0.115	04 30 54.131	64 50 43.39	0.38±0.11	1.81	300	0.88×0.74	89	0.148	0.82±0.04	
	Tot												3.70±0.40	
IC 467		0.18×0.15	41	0.101	07 30 19.115	79 52 25.99	0.44±0.10	0.69	300	0.44×0.16	136	0.102	0.63±0.10	offset 5.5''
	Tot												1.0±0.1	
NGC 2750	core?	0.18×0.09	167	0.072	09 05 47.931	25 26 15.32	0.35±0.07	0.60	500	<0.42× <0.22	135	0.055	0.28±0.07	multi- components 2.2'' → 425pc, offset <2''
		0.28×0.07	127	0.072	09 05 47.981	25 26 15.11	0.26±0.07	0.63	500	0.35×0.20	125	0.055	0.35±0.07	
		0.24×0.05	10.3	0.072	09 05 48.014	25 26 15.86	0.29±0.07	0.46	500	<0.31× <0.22	123	0.055	0.19±0.07	
		<0.24× <0.15	91.4	0.072	09 05 47.912	25 26 14.91	0.25±0.07	0.33	500	<0.29× <0.20	101	0.055	0.15±0.08	
		0.07×0.03	21	0.072	09 05 47.883	25 26 15.45	0.23±0.07	0.24	500	<0.27× <0.20	103	0.055	0.21±0.08	
	Tot												1.8±0.4	
NGC 2831	core	<0.19× <0.13	44.5	0.086	09 19 45.483	33 44 42.03	2.65±0.09	2.75	500	0.18× <0.11	56	0.103	2.39±0.10	NGC 2832 companion
	Tot												3.1±0.2	
NGC 3034	SNR	<0.23× <0.04	0.0	0.131	09 55 55.405	69 40 53.15	1.95±0.24	2.47	750	<0.28× <0.25	0.0	0.420	2.19±0.19	multi- components 31.7'' → 602pc
	SNR	0.44×0.20	40	0.131	09 55 55.259	69 40 59.91	2.23±0.15	6.12	750	0.56×0.25	35	0.420	2.23±0.24	
	SNR	0.27×0.16	80	0.131	09 55 55.214	69 40 50.03	3.38±0.27	7.08	750	0.27×0.21	64	0.420	3.89±0.27	
	SNR	<0.14× <0.08	0.0	0.131	09 55 54.609	69 40 49.99	3.03±0.25	3.26	750	<0.28× <0.25	0.0	0.420	3.17±0.26	
	SNR	0.24×0.19	132	0.131	09 55 54.460	69 40 51.43	3.88±0.17	7.56	750	0.25×0.20	133	0.420	4.52±0.21	
		0.51×0.37	168	0.131	09 55 54.097	69 40 46.45	1.47±0.15	5.73	750	0.42×0.36	177	0.420	1.92±0.19	
	SNR	0.13×0.08	150	0.131	09 55 54.133	69 40 53.58	3.67±0.16	4.56	750	0.12×0.04	152	0.420	4.01±0.18	
	SNR	0.44×0.24	127	0.131	09 55 53.967	69 40 51.31	2.06±0.31	8.2	750	0.51×0.30	128	0.420	2.49±0.34	
	SNR	0.14×0.13	97	0.131	09 55 53.880	69 40 47.40	14.38±0.49	20.0	750	0.17×0.15	90	0.420	15.28±0.48	
	SNR	<0.36× <0.07	0.0	0.131	09 55 53.628	69 40 47.31	1.58±0.30	2.57	750	<0.37× <0.04	0.0	0.420	1.91±0.27	
	SNR	0.26×0.18	85	0.131	09 55 53.145	69 40 47.96	1.98±0.31	4.09	750	0.31×0.18	87	0.420	2.23±0.12	
	SNR	0.19×0.14	176	0.131	09 55 53.229	69 40 44.36	2.93±0.17	4.39	750	0.19×0.12	9	0.420	3.20±0.24	
	SNR	0.16×0.15	2	0.131	09 55 52.991	69 40 45.49	4.26±0.17	6.36	750	0.15×0.13	14	0.420	4.82±0.23	
	SNR	0.11×0.03	57	0.131	09 55 52.727	69 40 45.77	10.63±0.25	11.87	750	0.12×0.02	57	0.420	10.83±0.26	
		<0.24× <0.20	0.0	0.131	09 55 52.028	69 40 45.41	22.89±0.60	20.50	750	<0.28× <0.25	0.0	0.420	22.88±0.64	
	SNR	0.22×0.17	156	0.131	09 55 51.908	69 40 44.54	7.87±0.51	14.2	750	0.26×0.19	156	0.420	8.69±0.48	
	SN 2008iz	0.22×0.17	156	0.131	09 55 51.551	69 40 45.78	59.00±0.44	56.22	750	<0.28× <0.25	0.0	0.420	58.61±0.47	
	SNR	0.83×0.34	18	0.131	09 55 51.416	69 40 42.66	2.22±0.19	17.4	750	0.74×0.34	20	0.420	2.95±0.20	
	SNR	0.41×0.13	22	0.131	09 55 51.386	69 40 41.86	2.99±0.28	7.03	750	0.66×0.14	22	0.420	2.94±0.39	
	SNR	0.44×0.31	174	0.131	09 55 51.261	69 40 48.17	2.59±0.22	8.94	750	0.53×0.25	172	0.420	2.95±0.32	
		0.41×0.26	57	0.131	09 55 51.230	69 40 46.42	1.83±0.27	3.79	750	0.43×0.26	64	0.420	1.81±0.34	
	XS	<0.24× <0.20	0.0	0.131	09 55 50.688	69 40 43.75	16.22±0.36	15.33	750	<0.28× <0.25	0.0	0.420	16.07±0.41	

Continued on Next Page

Table A3 – Continued

name	comp	Full resolution							Low resolution					morph/size
		$\theta_M \times \theta_m$ [arcsec ²]	PA _d deg	rms mJy/b	α (J2000)	δ (J2000)	F _{peak} mJy/b	F _{tot} mJy	$u-v$ k λ	$\theta_M \times \theta_m$ [arcsec ²]	PA _d deg	rms mJy/b	F _{peak} mJy/b	
	SNR	<0.24×<0.20	0.0	0.131	09 55 50.049	69 40 45.92	3.50±0.24	3.18	750	<0.28×<0.25	0.0	0.420	3.67±0.29	
	SNR	0.20×0.12	137	0.131	09 55 49.421	69 40 41.43	8.93±0.15	13.87	750	10.20×0.13	139	0.420	10.20±0.13	
	SNR	0.54×0.34	68	0.131	09 55 49.363	69 40 42.42	2.27±0.22	11.2	750	0.54×0.43	62	0.420	2.81±0.32	
	SNR	0.31×0.20	81	0.131	09 55 49.061	69 40 41.52	2.51±0.21	5.61	750	0.36×0.20	80	0.420	2.84±0.21	
	SNR	0.20×0.15	4	0.131	09 55 47.873	69 40 43.72	6.14±0.15	10.12	750	0.20×0.15	4	0.420	6.94±0.18	
	Tot												206±15	
NGC 3077		0.28×0.19	86	0.090	10 03 18.808	68 43 56.65	1.30±0.08	2.92	500	0.26×0.19	91	0.101	1.81±0.10	SNR? 5.6'' offset
	Tot												2.8±0.2	
NGC 3690	Arp299C	0.48×0.28	175	0.201	11 28 30.657	58 33 49.28	1.33±0.20	7.45	500	0.66×0.40	-68.7	0.236	1.82±0.24	merging system
	Arp299B	0.25×0.21	59	0.190	11 28 30.987	58 33 40.83	14.1±0.7	26.10	500	0.27×0.24	79	0.231	15.21±0.80	
	Arp299A	0.52×0.41	131	0.203	11 28 33.631	58 33 46.68	23.14±0.87	108.8	500	0.52×0.42	129	0.245	31.23±0.25	
	Tot												142±10	
NGC 3838	core	<0.34×<0.21	19.3	0.089	11 44 10.854	57 56 53.34	0.99±0.08	1.03	500	<0.45×<0.35	1.2	0.078	0.89±0.08	offset 23.2''
	Tot												1.1±0.2	
NGC 4111		0.34×0.23	19.1	0.102	12 07 03.614	43 03 55.99	0.55±0.10	0.78	500	0.57×0.06	19.4	0.110	0.50±0.11	offset 6''
		0.83×0.32	11.3	0.102	12 07 03.854	43 03 59.58	0.46±0.10	1.86	500	0.73×0.26	1.4	0.110	0.48±0.11	
	Tot												1.85±0.13	
NGC 4162		0.36×0.27	104	0.175	12 11 54.104	24 06 58.76	2.40±0.24	5.35	500	0.48×0.22	123	0.233	3.11±0.27	double source, offset \gtrsim 30''
		<0.48×<0.16	137	0.175	12 11 54.046	24 06 58.47	7.75±0.28	6.70	500	<0.60×<0.23	139	0.233	6.96±0.24	
	Tot												10.2±1.0	
NGC 4236		<0.19×<0.12	12.0	0.086	12 16 35.542	69 28 00.57	2.91±0.20	3.23	500	0.13×0.03	149	0.103	2.98±0.16	double source, 37.9'' offset
	Tot												3.3±0.2	
NGC 4242	core	0.09×0.06	7.5	0.279	12 17 28.247	45 37 25.11	11.25±0.30	11.30	300	0.22×0.05	7.4	0.176	10.70±0.18	double source, 26'' offset
		0.26×0.25	168	0.279	12 17 28.203	47 37 26.13	1.33±0.28	2.24	300	0.51×0.05	16.0	0.176	1.78±0.19	
		0.42×0.25	8.3	0.279	12 17 28.250	47 37 24.12	1.18±0.28	1.05	300			0.176	<1.2	
	Tot												14.7±0.5	
NGC 4631		0.20×0.21	78	0.077	12 42 07.697	32 32 30.08	0.34±0.08	0.79	500	0.25×0.27	-67.7	0.076	0.40×0.08	offset 3.6''
		0.26×0.02	78	0.077	12 42 07.689	32 32 30.57	0.31±0.08	0.43	500	<0.31×0.21	57.8	0.076	0.28×0.08	
	Tot												1.22±0.18	
NGC 5012		0.13×0.07	45	0.079	13 11 37.048	22 54 58.277	0.41±0.08	0.44	500	<0.30×<0.24	31	0.068	0.41×0.07	offset 2.6''
	Tot												0.45±0.10	

Column description: (1) galaxy name; (2) radio component: radio component: (core, SNR or X-ray source [XS]) or unidentified component if not labeled; (3) deconvolved FWHM dimensions (major \times minor axes [arcsec²], $\theta_M \times \theta_m$) of the fitted component, determined from an elliptical Gaussian fit from the full-resolution radio map; (4) PA of the deconvolved component, PA_d, from the full-resolution radio map (degree); (5) rms of the radio map close to the specific component from the full-resolution radio map (mJy/b, mJy beam⁻¹); (6)-(7) radio position (J2000.0); (8) peak flux density in mJy beam⁻¹, F_{peak}, from the full-resolution radio map; (9) integrated flux density, F_{tot}, in mJy, from the full-resolution radio map; (10) uv -taper scale of the low-resolution radio map in k λ ; (11) deconvolved FWHM dimensions (major \times minor axes [arcsec²], $\theta_M \times \theta_m$) of the fitted component, determined from an elliptical Gaussian fit from the low-resolution radio map; (12) PA of the deconvolved component, PA_d from the low-resolution radio map (degree); (13) rms of the radio map close to the specific component from the low-resolution radio map (mJy beam⁻¹); (14) peak flux density in mJy beam⁻¹, F_{peak} from the low-resolution radio map. At the bottom of each target the total flux density of the radio source associated with the galaxy is given in mJy, measured from the low-resolution map; (15) radio morphology, size in arcsec and pc and offset from the optical centre, if present.

Table A4: Radio contour levels

name	full resolution			low resolution				
	Beam	PA	levels	kλ	beam	PA	levels	
NGC 1161	0.18×0.12	55.8	0.20×(−1,1,2,4,8,13)	500	0.34×0.18	−39.9	0.50×(−1,1,2,4,5,5)	
NGC 1167	0.20×0.20	0	15×(−1,1,2.5,5,10,20,30)	500	0.40×0.40	0	8×(−1, 1, 2, 5, 10, 20, 40, 70)	
NGC 1186	0.18×0.12	52.3	0.15×(−1, 1, 2)	750	0.35×0.19	−43.4	0.15×(−1,1,2,3)	
NGC 1275	1.00×0.33	−41.6	600×(−1, 1, 2, 4, 8, 16)	750	1.20×0.39	−41.0	1000×(−1, 1, 2, 4, 8)	
IC 342	0.33×0.20	−57.3	0.6×(−1,1,1.4,2)	500	0.43×0.35	−29.5	0.5×(−1,1,1.3,2,3)	
IC 356	0.33×0.20	−54.5	0.25×(−1,1,1.5,2)	300	0.62×0.52	5.3	0.20×(−1,1,1.5)	
NGC 1569	0.33×0.20	−50.1	0.25×(−1,1,1.5)	300	0.63×0.52	5.0	0.30×(−1,1,2,2.5,3)	
NGC 1560	0.26×0.17	−53.7	0.26×(−1,1,1.3)	300	0.52×0.41	−174.3	0.23×(−1,1,1.5,2)	
NGC 1961	0.29×0.18	−35.8	0.35×(−1,1,2,4,7)	300	0.53×0.41	17.6	0.28×(−1,1,2,4,8)	
NGC 2146	0.27×0.18	−23.7	0.7×(−1,1,2,4)	300	0.48×0.38	31.6	0.55×(−1,1,2,4,)	
IC 467	0.26×0.19	−15.7	0.26×(−1,1,1.5)	300	0.45×0.39	50.6	0.30×(−1,1,1.5,2)	
NGC 2683	0.26×0.18	22.8	0.12×(−1,1,1.5,3,3.9)	500	0.38×0.33	−57.1	0.11×(−1, 1, 1.5, 2.1, 3.5)	
NGC 2750	0.19×0.14	33.0	0.17×(−1, 1, 1.5, 1.9)	500	0.40×0.24	−55.3	0.13×(−1, 1, 1.5, 2.5)	
NGC 2768	0.15×0.15	88.6	0.8×(−1,1,2,4,8,13)	500	0.24×0.21	−81	0.9×(−1,2,4,8,13)	
NGC 2782	0.24×0.15	31.5	0.22×(−1, 1, 2, 4, 8)	750	0.27×0.22	53.8	0.20×(−1, 1, 2, 4, 8, 12)	
NGC 2787	0.16×0.15	−53.8	0.9×(−1,1,1.5,3,6)	750	0.20×0.18	−47.8	0.8×(−1,1,1.5,3,6)	
NGC 2832	0.18×0.14	50.3	0.19×(−1, 1, 1.5, 2)	500	0.42×0.24	137.8	0.25×(−1, 1, 1.5, 2)	
NGC 2831	0.18×0.14	50.3	0.30×(−1, 1, 2, 4, 8)	500	0.42×0.24	137.8	0.30×(−1, 1, 2, 4, 8)	
NGC 2964	0.17×0.16	57.5	0.24×(−1, 1, 2, 4)	500	0.47×0.26	−48.5	0.32×(−1, 1, 2, 3, 4)	
NGC 2985	0.16×0.15	−54.9	0.24×(−1,1,1.5,2,2.5)	500	0.24×0.22	−44.5	0.26×(−1,1,1.5,2,2.7)	
NGC 3031	0.25×0.21	61.5	2.9×(−1,1,2.5,5,15,30)	500	0.32×0.30	−69.5	2.9×(−1,1,2.5,5,15,30)	
NGC 3034	0.24×0.20	60.1	0.002×(−0.5,1,2,4,5, 10,15,20,25,30)	750	0.28×0.25	73.7	0.002×(−0.5,1,2,4,5, 10,15,20,25,30)	
NGC 3077	0.24×0.19	46.6	0.23×(−1,1,1.5,2,2.7)	500	0.30×0.28	62.3	0.24×(−1,1,2,3)	
NGC 3077*	0.24×0.19	46.6	0.21×(−1,1,2,3,5,7)	500	0.30×0.28	62.3	0.23×(−1,1,2,4,8)	
NGC 3079	0.30×0.25	64.7	3×(−0.8,1,1.5,2,4,8)	300	0.47×0.38	−27	4×(−1,1,2,4,8)	
NGC 3147	0.28×0.23	67.5	0.37×(−1,1,2,4,8,16)	750	0.29×0.25	65.8	0.35×(−1,1,2,4,8,16)	
NGC 3245	0.19×0.17	39.1	0.17×(−1,1,1.5,2,3)	{	750	0.22×0.21	86.6	0.18×(−1,1,1.5,2,3)
					300	0.49×0.40	−49.0	0.15×(−1, 1, 1.5, 2, 4, 6)
					750	0.23×0.22	60.5	0.17×(−1,1,1.5,2,3)
NGC 3301	0.21×0.18	26.8	0.17×(−1,1,1.5,2,3)	750	0.23×0.22	60.5	0.17×(−1,1,1.5,2,3)	
NGC 3310	0.27×0.23	69.4	0.3×(−1,1,1.5,2)	750	0.29×0.26	58.1	0.3×(−1,1,1.5,2)	
NGC 3348	0.23×0.19	56.7	0.18×(−1,1,1.5,2,4,7)	750	0.27×0.24	67.0	0.19×(−1,1,1.5,2,4,7)	
NGC 3448	0.27×0.22	71.5	0.22×(−1,1,1.5)	300	0.46×0.36	−9.9	0.25×(−1,1,1.5,2)	
NGC 3504	0.22×0.19	−77.4	0.22×(−1, 1, 2, 4, 8, 16, 32, 64)	500	0.31×0.26	−81.7	0.24×(−1,1,2,4,8,16,32,64)	
NGC 3516	0.23×0.19	50.9	0.5×(−1,1,2,3,6)	{	500	0.30×0.28	78.7	0.5×(−0.8,1,2,3,4,6)
					300	0.38×0.36	−43.0	0.5×(−1,1,1.5,2,4,6)
					500	0.32×0.28	−68.7	0.8×(−0.8,1,2,4,8,16)
NGC 3690 Arp299-B	0.28×0.21	88.2	0.8×(−0.8,1,2,4,8,16)	500	0.32×0.28	−68.7	1.1×(−1,1,2,4,8,16,28)	
NGC 3690 Arp299-A	0.28×0.21	88.2	0.8×(−0.9,1,2,4,8,16,28)	500	0.32×0.28	−68.7	0.6×(−1,1,1.5,2,3)	
NGC 3690 Arp299-C	0.28×0.21	88.2	0.7×(−0.8,1,2,1.5)	500	0.32×0.28	−68.7	0.6×(−1,1,1.5,2,3)	
NGC 3718	0.33×0.20	4.1	0.25×(−1, 1, 2, 4, 8, 16, 32)	500	0.50×0.35	−4.7	0.28×(−1, 1, 2, 4, 8, 16, 32)	
NGC 3729	0.31×0.20	2.6	0.29×(−1, 1, 2, 4)	500	0.49×0.35	−5.1	0.30×(−1, 1, 2, 4, 7)	
NGC 3735	0.23×0.19	−59.0	0.19×(−1,1,1.5,2,3)	750	0.27×0.24	68	0.2×(−1,1,1.5,2,3)	
NGC 3838	0.32×0.21	−155	0.22×(−1, 1, 2, 4)	500	0.45×0.36	−3.5	0.21×(−1, 1, 2, 4)	
NGC 3884	0.70×0.34	−41.5	0.45×(−1,1,2,4,8)	750	0.47×0.47	0	0.53×(−1,1,1.5,3,4.5)	
NGC 3898	0.30×0.19	−175	0.21×(−1, 1, 2, 3)	500	0.47×0.35	−7.2	0.30×(−1, 1, 2, 3)	
NGC 3941	0.20×0.19	41.1	0.20×(−1,1,1.5,2)	500	0.25×0.24	37.7	0.20×(−1,1,1.5,2,3)	
NGC 3945	0.17×0.14	33.5	0.19×(−1,1,1.5,2,3)	300	0.44×0.39	−8.2	0.18×(−1,1,1.5,2,3)	
NGC 3963	0.24×0.15	−42.8	0.20×(−1, 1, 1.5)	500	0.44×0.35	−5.6	0.20×(−1, 1, 1.5)	
NGC 3982	0.18×0.12	−60.6	0.48×(−1, 1, 1, 2, 4)	500	0.39×0.29	−7.7	0.34×(−1, 1, 2, 4, 8)	
NGC 3998	0.32×0.20	−4.0	5×(−0.3, 1, 2, 4, 8, 16)	500	0.50×0.35	−9.8	1×(−0.4, 1, 2, 4, 8, 16, 32, 64, 100)	
NGC 4036	0.17×0.14	34.7	0.25×(−1,1,2,3,7)	{	500	0.28×0.27	−26	0.27×(−1,1,2,4,8)
					300	0.43×0.39	−8.4	0.20×(−1,1,2,4,8,14)
NGC 4041	0.17×0.15	30.1	0.15×(−1,1,1.5,2,3)	500	0.29×0.26	−27.2	0.14×(−1,1,1.5,3,4)	
NGC 4100	0.20×0.16	−55.9	0.19×(−1,1,1.5,2)	750	0.24×0.19	−55.1	0.20×(−1,1,1.5,2,2,3)	
NGC 4102	0.20×0.15	−43.2	0.31×(−1,1,1.5,2,3,5,6)	500	0.27×0.22	−39.1	0.30×(−1,1,2,3,4,6,8)	
NGC 4111	0.40×0.23	16.1	0.29×(−1,1,1.4,1.8)	500	0.53×0.29	16.6	0.26×(−1,1,1.4,1.8)	
NGC 4111*	0.40×0.23	16.1	0.30×(−1,1,1.5)	500	0.53×0.29	16.6	0.29×(−1,1,1.5)	
NGC 4143	0.40×0.22	16.0	0.50×(−1,1,1.5,3,4,5)	300	0.76×0.41	9.9	0.47×(−1,1,2,3,4)	
NGC 4151	0.26×0.16	38.8	1×(−0.5,1,2,4,9,16, 25,36,49,64)	500	0.34×0.25	47.3	1.1×(−0.5,1,2,4,9,16, 25,36,49,64)	
NGC 4162	0.47×0.19	−43.8	0.9×(−1,1,1.5,2,3,6)	500	0.58×0.27	−41.4	0.7×(−1,1,1.5,2,3,6)	

Continued on Next Page

Table A4 – Continued

name	full resolution			low resolution				
	Beam	PA	levels	k λ	beam	PA	levels	
NGC 4203	0.22 \times 0.18	54.7	0.50 \times (−1,1,2,4,8,13)	500	0.28 \times 0.23	59.5	0.60 \times (−1,1,2,4,8,11)	
NGC 4217	0.46 \times 0.26	8.0	0.2 \times (−1,1,1.4)	300	0.73 \times 0.41	7.9	0.26 \times (−1,1,1.4,1.8)	
NGC 4220	0.38 \times 0.21	9.8	0.21 \times (−1,1,1.4)	300	0.73 \times 0.41	−174.5	0.21 \times (−1,1,1.5,2)	
NGC 4236	0.16 \times 0.12	25.0	0.40 \times (−0.8, 1, 2, 4)	500	0.25 \times 0.22	2.2	0.60 \times (−0.8, 1, 2, 4)	
NGC 4244	0.20 \times 0.20	33.7	0.20 \times (−1,1,1.5)	300	0.38 \times 0.32	6.7	0.20 \times (−1,1,1.5,2)	
NGC 4242	0.42 \times 0.25	8.3	0.70 \times (−1,1,1.4,4,8,13)	300	0.78 \times 0.41	6.7	0.80 \times (−0.8, 1, 1.5, 2, 4, 8, 13)	
NGC 4258	0.42 \times 0.25	−176.3	0.25 \times (−1,1,2,4)	750	0.49 \times 0.28	−173.9	0.25 \times (−1,1,2,4)	
NGC 4278	0.32 \times 0.32	0.0	2.5 \times (−1,1,2,4,8,16, 32,64)	750	0.38 \times 0.38	0.0	2.3 \times (−1,1,2,4,8,16,32,6)	
NGC 4369	0.19 \times 0.17	78.1	0.08 \times (−1, 1, 1.5)	300	0.47 \times 0.42	−51.6	0.09 \times (−1, 1, 1.5, 2)	
NGC 4395	0.22 \times 0.18	56.2	0.25 \times (−1,1,1.5,2.5)	500	0.27 \times 0.24	70.2	0.25 \times (−1,1,1.5,2,2.5)	
NGC 4494	0.23 \times 0.20	49.3	0.13 \times (−1,1,2)	750	0.26 \times 0.23	57.6	0.11 \times (−1,1,2,3)	
NGC 4565	0.22 \times 0.20	44.4	0.26 \times (−1,1,2,3,4)	500	0.28 \times 0.27	69.1	0.22 \times (−0.8,1,2,3,4)	
NGC 4589	0.16 \times 0.12	30.9	0.65 \times (−1,1,2,4,8,16)	750	0.20 \times 0.16	20.9	0.70 \times (−1,1,2,4,8,16)	
NGC 4631	0.21 \times 0.20	77.9	0.17 \times (−1,1,1.5,2)	500	0.27 \times 0.25	−67.7	0.18 \times (−1,1,2)	
NGC 4750	0.16 \times 0.12	27.2	0.15 \times (−1,1,2,3)	500	0.25 \times 0.22	−5.9	0.15 \times (−0.8,1,2,3,5)	
NGC 4736	0.25 \times 0.16	33.1	0.30 \times (−1, 1, 1.5, 3, 6)	500	0.34 \times 0.24	45.2	0.40 \times (−1, 1, 1.5, 3, 6)	
NGC 4826	0.22 \times 0.20	46.4	0.17 \times (−1,1,1.5,2,3)	300	0.39 \times 0.34	−42.0	0.18 \times (−1,1,2,3,4)	
NGC 5012	0.23 \times 0.20	42.5	0.18 \times (−1,1,1.5,2)	750	0.29 \times 0.26	48.5	0.17 \times (−1,1,1.5,2)	
NGC 5033	0.18 \times 0.16	52.7	0.19 \times (−1, 1, 2, 4, 8)	500	0.30 \times 0.26	−50.6	0.20 \times (−1, 1, 2, 4, 8)	
NGC 5322	0.31 \times 0.22	33.0	0.27 \times (−1,1,1.5,2,4,10)	{	500	0.40 \times 0.31	17.7	0.34 \times (−1,1,1.5,2,4,10)
					300	0.44 \times 0.38	−169	0.30 \times (−1,1,1.5,2,4,10)
NGC 5354	0.19 \times 0.16	67.1	0.30 \times (−1, 1, 2, 4, 8,14)	500	0.31 \times 0.26	−62.4	0.30 \times (−1, 1, 2, 4, 8,14)	
NGC 5485	0.40 \times 0.20	27.1	0.44 \times (−1, 1, 1.5, 2, 3)	500	0.46 \times 0.34	13.2	0.35 \times (−1,1,1.5,2,3)	
NGC 5548	0.21 \times 0.14	−161.6	0.20 \times (−1,1,1.5,3,5)	{	500	0.26 \times 0.22	11.2	0.20 \times (−1,1,2,4)
					300	0.35 \times 0.34	−21.2	0.25 \times (−1,1,1.4,2.2,3.2,5)
NGC 6217	0.17 \times 0.14	72.4	0.23 \times (−1,1,1.5,2)	500	0.25 \times 0.23	115	0.23 \times (−1,1,1.5,2)	
NGC 6340	0.17 \times 0.15	69.8	0.22 \times (−1,1,1.5,2)	300	0.37 \times 0.32	−21.6	0.25 \times (−1,1,1.8,2.7)	
NGC 6482	0.19 \times 0.16	64.6	0.16 \times (−1, 1, 1.6, 2.6)	500	0.28 \times 0.21	−73.1	0.17 \times (−1, 1, 2, 2.8)	
NGC 7080	0.31 \times 0.15	4.3	0.16 \times (−1,1,2.5)	500	0.32 \times 0.21	9.6	0.16 \times (−1,1,1.8)	

Column description: (1) source name; (2) FWHM of the elliptical Gaussian restoring beam in arcsec² of the full-resolution maps (Fig. A1); (3) PA of the restoring beam (degree) of the full-resolution maps; (4) radio contour levels (mJy beam^{−1}) of the full-resolution maps; (5) uv taper scale parameter in k λ of the low-resolution radio maps (the full sets of figures is in the online supplementary data); (6) FWHM of the elliptical Gaussian restoring beam in arcsec² of the low-resolution maps (the full sets of figures is in the online supplementary data); (7) PA of the restoring beam (degree) of the low-resolution maps; (8) radio contour levels (mJy beam^{−1}) of the low-resolution maps. The * tag identifies the secondary radio source detected in the field of the main target.